

MANIPULATION OF LARGE NEUTRAL MOLECULES
WITH ELECTRIC FIELDS

Manipulation of large molecules with electric fields

Frank Filsinger

Thesis Radboud Universiteit Nijmegen – Illustrated

With references – With summary in Dutch and English

ISBN: 978-90-8891-137-8

Subject headings: Molecular Beams / Electric Fields / Quantum-state Selection / Conformer Separation

Cover: Design by the author. Front: Photograph of the m/μ -selector, along with a measurement of the transmission through the selector as a function of the AC frequency for cis- and trans-3-aminophenol. Back: Photograph of the electrostatic deflector, along with a contour plot of the electric field strength.

Printed by Boxpress BV / Proefschriftmaken.nl

MANIPULATION OF LARGE NEUTRAL MOLECULES WITH ELECTRIC FIELDS

EEN WETENSCHAPPELIJKE PROEVE OP HET GEBIED VAN DE
NATUURWETENSCHAPPEN, WISKUNDE EN INFORMATICA

PROEFSCHRIFT

TER VERKRIJGING VAN DE GRAAD VAN DOCTOR
AAN DE RABOUD UNIVERSITEIT NIJMEGEN
OP GEZAG VAN DE RECTOR MAGNIFICUS PROF. DR. S.C.J.J. KORTMANN
VOLGENS BESLUIT VAN HET COLLEGE VAN DECANEN
IN HET OPENBAAR TE VERDEDIGEN
OP VRIJDAG 12 FEBRUARI 2010,
OM 13.00 UUR PRECIES

DOOR

FRANK FILSINGER

GEBOREN OP 9 OKTOBER 1978
TE HEIDELBERG, DUITSLAND

PROMOTOR : PROF. DR. G. J. M. MEIJER
COPROMOTOR : DR. J. KÜPPER
FRITZ-HABER-INSTITUT DER
MAX-PLANCK-GESELLSCHAFT, BERLIN

MANUSCRIPTCOMMISSIE : PROF. DR. W. L. MEERTS

PROF. DR. H. STAPELFELDT
AARHUS UNIVERSITY, AARHUS

DR. M. TARBUTT
IMPERIAL COLLEGE LONDON, LONDON

The work described in this thesis has been performed at the Fritz-Haber-Institut der Max-Planck-Gesellschaft in Berlin, Germany.

MANIPULATION OF LARGE NEUTRAL MOLECULES WITH ELECTRIC FIELDS

AN ACADEMIC ESSAY IN
SCIENCE

DOCTORAL THESIS

TO OBTAIN THE DEGREE OF DOCTOR
FROM RADBOUD UNIVERSITY NIJMEGEN
ON THE AUTHORITY OF THE RECTOR MAGNIFICUS
PROF. DR. S.C.J.J. KORTMANN
ACCORDING TO THE DECISION OF THE COUNCIL OF DEANS
TO BE DEFENDED IN PUBLIC
ON FRIDAY, 12 FEBRUARY 2010
AT 13.00 HOURS

BY

FRANK FILSINGER

BORN ON 9 OCTOBER 1978
IN HEIDELBERG, GERMANY

SUPERVISOR : PROF. DR. G. J. M. MEIJER
CO-SUPERVISOR : DR. J. KÜPPER
FRITZ-HABER-INSTITUT DER
MAX-PLANCK-GESELLSCHAFT, BERLIN

MANUSCRIPT COMMITTEE: PROF. DR. W. L. MEERTS

PROF. DR. H. STAPELFELDT
AARHUS UNIVERSITY, AARHUS

DR. M. TARBUTT
IMPERIAL COLLEGE LONDON, LONDON

The work described in this thesis has been performed at the Fritz-Haber-Institut der Max-Planck-Gesellschaft in Berlin, Germany.

Contents

1	Introduction	1
1.1	Manipulation of molecular beams with electric and magnetic fields	1
1.1.1	The early days	1
1.1.2	Focusing and deceleration of molecules in low-field-seeking quantum states	2
1.1.3	Focusing and deceleration of molecules in high-field-seeking quantum states	4
1.2	Large neutral molecules in the gas phase	5
1.3	Outline of this thesis	7
2	The asymmetric rotor	9
2.1	Introduction	9
2.2	The field-free asymmetric rotor	10
2.3	Nuclear spin statistical weights	15
2.4	Stark effect of the asymmetric rotor	18
3	Alternating gradient focusing	25
3.1	Introduction	25
3.2	General principles	25
3.3	Electrode geometries	27
3.4	Solving the equations of motion	33
3.4.1	Equations of motion in the harmonic approximation	33
3.4.2	Matrix method to calculate solutions of Hill's differential equation	35
3.4.3	Analytic solution for a piecewise constant wave form	36
3.5	Stability, selectivity, and the role of the duty cycle	37
3.6	Numerical simulations	42
3.6.1	Electric field	42
3.6.2	Simulations for individual quantum states	42
3.6.3	Simulation of a molecular beam	43

4	Fourier-transform microwave spectroscopy to determine molecular constants of 3-aminophenol	45
4.1	Introduction	45
4.2	Experimental setup	47
4.3	Calibration of the Stark measurements	48
4.4	Computational details	49
4.5	Results	50
4.6	Summary	56
5	Laser-induced alignment and orientation of quantum-state-selected large molecules	59
5.1	Introduction	59
5.2	Experimental setup	60
5.3	Electrostatic deflection of cold molecular beams	62
5.4	Alignment of quantum-state-selected large molecules	70
5.5	Orientation of quantum-state-selected large molecules	74
5.6	Summary	78
6	Conformer selection of large neutral molecules with static electric fields	81
6.1	Introduction	81
6.2	Experimental setup	83
6.3	Results	84
6.4	Summary	86
7	Selector for structural isomers of neutral molecules	89
7.1	Introduction	89
7.2	Experimental setup	89
7.2.1	Source	91
7.2.2	Design of the selector	93
7.2.3	High-voltage switching schemes	95
7.2.4	Detection	97
7.3	Alternating gradient focusing of ammonia	99
7.4	Conformer selection of 3-aminophenol	106
7.5	Improving selectivity – changing the duty cycle	111
7.6	Summary	116
8	Outlook	119
8.1	The next generation μ/m -selector	119
8.2	What's next?	127
	Bibliography	129
	Samenvatting	145

Summary	149
Acknowledgements	153
Curriculum Vitae	155
List of publications	157

Chapter 1

Introduction

1.1 Manipulation of molecular beams with electric and magnetic fields

1.1.1 The early days

“When God said ‘Let there be light’ he surely must have meant perfectly coherent light.” [1] This statement by Nobel Laureate Charles H. Townes, one of the pioneers of laser physics, summarizes the importance of coherent light sources for many applications in chemistry and physics. Nowadays, lasers are used in countless laboratories around the world to sensitively and quantum-state-selectively detect atoms and molecules. Of great importance for the development of coherent light sources – and for the field of chemistry and physics in general – was the introduction of atomic and molecular beam methods [2, 3].

In principle, an atomic or molecular beam is nothing but a “leak in a vacuum system”, as John B. Fenn phrases it [4]. By expanding atoms or molecules from a reservoir at high pressure into vacuum, an isolated environment is provided, where their intrinsic properties can be investigated under collision-free conditions, independent from interactions with other species. In the early 20th century, when the beam method was developed, laser-based quantum-state-selective detection techniques were still lacking. In 1921 Otto Stern proposed that the trajectories of silver atoms on their way to the detector could be characteristically altered, depending on their quantum state, when the atomic beam was exposed to an inhomogeneous magnetic field [5]. In a ground-breaking experiment, Walter Gerlach and Otto Stern demonstrated in 1922 [6] that indeed quantum-state selectivity could be achieved in the detection process by sorting different quantum states *via* space quantization, a concept

that has been extensively used ever since. The possibility to deflect polar molecules in a molecular beam with an electric field was conceived at the same time. It was first theoretically described by Hartmut Kallmann and Fritz Reiche in 1921 [7], and later experimentally demonstrated by Erwin Wrede in 1927 [8].* As early as 1926, Stern suggested that the technique could be used for the quantum-state separation of small diatomic molecules at low temperatures [9]. Over the years, various experimental geometries were designed to create strong field gradients on the beam axis in order to efficiently deflect particles. In 1938/1939 Isidor Rabi introduced the molecular beam magnetic resonance method, by using two deflection elements of oppositely directed gradients in succession, to study the quantum structure of atoms and molecules [10, 11]. In his setup, the deflection of particles caused by the first magnet was compensated by a second magnet such that the particles reached the detector on a sigmoidal path. If in between the two magnets a transition to a different quantum state was induced, this compensation was incomplete and a reduction of the detected signal could be observed. Since these early days of molecular beam deflection experiments, the deflection technique has been widely used as a tool to determine dipole moments and polarizabilities of molecular systems ranging from diatomics [8] to clusters [12, 13] to large biomolecules [14].

1.1.2 Focusing and deceleration of molecules in low-field-seeking quantum states

Whereas deflection experiments allow for the spatial dispersion of quantum states, they do not provide any focusing. For small molecules in eigenstates whose energy increases with increasing field strength, so-called low-field-seeking (lfs) states, this issue could be resolved by using multipole focusers. Both magnetostatic [15, 16] and electrostatic [17] devices were developed in the early 1950s by Wolfgang Paul's group in Bonn. Independently, an electrostatic quadrupole focuser, i. e., a symmetric arrangement of four cylindrical electrodes around the beam axis that are alternately charged by positive and negative high voltages, was built in 1954/55 by James Gordon, Herbert Zeiger and Charles Townes in New York to couple a beam of ammonia molecules into a microwave cavity [18]. Only ammonia molecules in the upper component of the inversion doublet of the $J_K = 3_3$ rotational state could be focused by the quadrupole field, resulting in a population inversion in the cavity. This inverted population distribution led to a spectacular "microwave amplification by stimulated emission of radiation" [19], the so-called maser. This coherent light source was the precursor of the nowadays omnipresent laser. By using

*In fact, Stern states in a footnote that the publication [5] describing the theory of his famous experiment was motivated by Kallmann and Reiche's article, of which he had received the galley proofs.

several multipole focusers in succession with interaction regions with electromagnetic radiation in between them, many setups were developed to unravel the quantum structure of atoms and molecules – very similar to Rabi’s molecular beam magnetic resonance method. About ten years after the invention of the multipole focusing technique, molecular samples in a single rotational state were used for state-specific inelastic scattering experiments by the Bonn group [20] and, shortly thereafter, for reactive scattering studies [21, 22]. In the following decades, multipole focusers were extensively used to study steric effects in gas-phase reactive scattering experiments, i. e., how the orientation of the colliding partners influences the reactivity [23, 24]. The preparation of oriented samples of state-selected molecules using electrostatic focusers was also essential for the investigation of steric effects in gas-surface scattering [25] and photodissociation [26] experiments. Variants of multipole focusing setups were implemented in many laboratories all over the world and yielded important information on stable molecules, radicals, and molecular complexes.

Until 1999, when the so-called Stark decelerator was realized [27], the manipulation of molecular beams with external fields exclusively concerned the transverse motion of the molecules. Typically, the gradients of the electric fields were directed perpendicular to the molecular beam axis providing a two-dimensional trap with a minimum of the potential on the axis. At the experimentally feasible electric field strengths on the order of 100 kV/cm, potential wells with a depth of typically 1 cm^{-1} can be created [28]. These wells are perfectly suitable to transversally confine the molecules because, in a typical molecular beam experiment, the transverse velocity distribution is centered around zero with a velocity spread of several tens of m/s; this corresponds to a kinetic energy spread of less than 1 cm^{-1} . However, the forward velocity of a molecular beam is much larger and typically centered around 250–2000 m/s, depending on the mass of the carrier gas (or the mass of the species itself when no carrier gas is used) and the expansion conditions. The resulting kinetic energy is on the order of 100 cm^{-1} or larger, too large to be substantially influenced by a single electrostatic lens. However, when about 100 lenses which create an electric field with a gradient perpendicular to the propagation direction are arranged along the beam axis, and the fields on adjacent electrode pairs are switched on and off at the appropriate times, a traveling potential well can be created that gradually slows down the molecules to a standstill [27–29]. Using Stark-decelerated molecular beams a variety of new experiments became feasible. Slow dipolar molecules could be trapped [30, 31], loaded into a storage ring [32] and a synchrotron [33], and used for high-resolution inelastic scattering experiments [34]. The long trapping times could be exploited to measure lifetimes of vibrationally [35] and electronically [36] excited states, and to investigate the effects of blackbody radiation on trapped molecules [37]. Recently, the optical [38] and magnetic [39–41] analogs of the Stark decelerator have also been demonstrated. Furthermore, metastable CO molecules have

been brought to a standstill using a miniaturized Stark decelerator on a chip [42].

The invention of multipole focusers and the Stark decelerator opened up new vistas and established a variety of new experiments, facilitated by the unprecedented control over the molecules' internal and external degrees of freedom. Unfortunately, both methods – static multipole focusing and Stark deceleration – only work for small molecules in lfs quantum states. However, the ground state of any molecule, as well as all low-lying rotational states of heavy or large molecules are high-field seeking (hfs) at the practically relevant fields, i. e., they feel a force towards regions of high electric field strength. Gaining similar control over these systems is more difficult and requires alternative approaches.

1.1.3 Focusing and deceleration of molecules in high-field-seeking quantum states

Large or heavy molecules have small rotational constants and, as a consequence, a high density of rotational states. Coupling between closely spaced states of the same symmetry turns lfs states into hfs states already at relatively weak electric field strengths (compared to the field strengths that are required for efficient focusing). In order to focus molecules in these states, a maximum of the electric field in free space would have to be created. Since Maxwell's equations do not allow for the creation of such a field with static fields alone [43, 44], static multipole fields cannot be applied to focus molecules in hfs states. The situation is analogous to charged particle physics in that ions also cannot be confined with static fields alone. This focusing problem for ions was solved when Ernest Courant, Stanley Livingstone, and Hartland Snyder introduced the principle of "alternating gradient (AG) focusing" in the 1950s [45, 46]. The basic idea is to create an array of electrostatic lenses that focus the particles along one transverse coordinate while defocusing them along the orthogonal transverse axis. Alternating the orientation of these fields at the appropriate frequency results in a net focusing force along both transverse coordinates. This principle is exploited to confine ions, for instance, in quadrupole mass filters [47, 48], in Paul traps [47, 49], and in virtually all particle accelerators. The application of AG focusing to neutral polar molecules was first proposed by Daniel Auerbach, Edward Bromberg, and Lennard Wharton [50] and experimentally demonstrated by Kakati and Lainé for ammonia molecules in hfs states [51–53]. Later, focusing of KF [54, 55] and ICl [56] molecules was also achieved. More recently, slow ammonia molecules were guided from an effusive source using a bent AG focuser [57], but molecules in lfs and hfs states could not be distinguished because the detection process was not state selective. Furthermore, CaF molecules have been guided using a 1 m-long straight AG

focuser [58].[†]

The first attempt to manipulate the forward velocity of molecules in hfs states was reported in the 1960s, when the group of Lennard Wharton at the University of Chicago set up an 11 m-long machine to accelerate LiF molecules [65, 66]. While these early experiments were unsuccessful and stopped after the PhD student had finished his thesis, a decelerator design that exploits the AG principle for transverse confinement of the molecules was successfully implemented in 2002 [67], inspired by the successful deceleration of small molecules with the Stark decelerator. Since then, so-called AG decelerators were used to decelerate CO [67, 68], YbF [69], and benzonitrile [70, 71] molecules. Deceleration of OH radicals in both hfs and lfs states was demonstrated using an AG decelerator as well [71, 72]. In these proof-of-principle experiments on high-field-seeking molecules, up to 30% of the kinetic energy was removed, but so far it has not been possible to decelerate molecules to velocities that are low enough for trapping. Nevertheless, AC trapping of para-ND₃ in the hfs component of its ground state was achieved by decelerating the molecule in a lfs state with a conventional Stark decelerator and subsequently transferring the population to the hfs state using microwave radiation [73, 74].

1.2 Large neutral molecules in the gas phase

During the last decades, the properties of biomolecules in the gas phase have been studied in ever greater detail [75–77]. Although the study of biomolecules outside of their natural environment was met with skepticism in the beginning, spectroscopic studies on isolated species in a molecular beam have proven to be very powerful for understanding their intrinsic properties. Moreover, their native environment can be mimicked by adding solvent molecules one by one [77–79]. These studies on well-defined biomolecular systems are particularly relevant to benchmark theoretical calculations. Even in the cold environment of a molecular beam, biomolecules exist in various conformational structures [80]. The existence of multiple conformers (structural isomers) has been observed in the study of glycine for the first time [81] and in numerous experiments since then. In many cases, the individual conformers are identified via their different electronic spectra [80, 82]. This has been exploited in multiple-resonance techniques to measure, for instance, conformer-specific infrared spectra from which the conformational structures can be deduced [83, 84]. However, in many cases the structural differences are subtle, resulting in very

[†]Besides the AG focusing technique, various alternative approaches were implemented to focus molecules in hfs states, such as exploiting the fringe fields of ring-like electrode structures [59], the fields created by crossed wires [60], or the fields created by coaxial electrodes [61–64]. Most of these methods, however, were only used for proof-of-principle experiments and did not find applications afterwards.

similar vibrational frequencies. An alternative method demonstrated by Feng Dong and Roger E. Miller [85] exploits the angles between vibrational transition moments and the permanent dipole moments of oriented molecules to assign individual conformers. The different quadrupole coupling constants, determined by means of Fourier-transform microwave spectroscopy [86], and the different dipole moments, deduced from the rotationally resolved spectra [87] (see also Chapter 4), have also been used to obtain structural information on individual conformers. Apart from this information on the local minima on the potential energy surface, information on the barriers separating the conformers has been obtained in sophisticated multiple-resonance experiments [88].

The preparation of conformer-selected samples of biomolecules would enable a new class of experiments to be performed on these systems, e. g. , electron and X-ray diffraction [89, 90] and tomographic imaging experiments [91]. Ultrafast dynamics studies on the ground-state potential energy surface would benefit from the availability of these pure samples as well. For charged species, the separation of structurally different molecules has been demonstrated using ion mobility in drift tubes [92, 93]. For neutral molecules no such separation method exists. It has been demonstrated that the abundance of the conformers in the beam can be partly influenced by selective over-the-barrier excitation in the early stage of the expansion [94] or by changing the carrier gas [95]. These methods, however, are not generally applicable nor able to specifically select each of the conformers.

The conformers of a biomolecule have all the same mass and the same connectivities between the atoms (primary structure) but differ by the orientations of their functional groups in the molecular frame, i. e. , by their folding pattern (secondary structure). The vectorial sum of the local dipole moments of the functional groups largely determines the overall dipole moment of the molecule. The different dipole moments of the conformers can be exploited to select individual conformers using electric fields. There are different approaches to achieve this separation. For instance, static electric fields can be used in a "Stern-Gerlach" type deflector, AC electric fields can be employed in a dynamic focuser, or the quantum-state selectivity of the AG deceleration process can be exploited. For biomolecules with several conformers, only electrostatic deflection experiments have been reported in the literature to date [14, 96–98]. However, all of these experiments were conducted on relatively warm beams at temperatures typically between 80 K and several 100 K. Deflection measurements under these conditions are not suitable for conformer separation, because large molecules are floppy and different conformers interconvert at these temperatures [97]. Furthermore, conformers with different permanent dipole moments will respond similarly to an electric field at high temperatures (see Chapter 7). In the framework of this thesis, it is demonstrated that both electrostatic beam deflection and AG focusing can be used to select conform-

ers of large molecules, when the techniques are applied to rotationally cold molecules in a supersonic jet. In principle, the AG decelerator could also be used for the same purpose, since the deceleration process is quantum-state selective and thus intrinsically conformer selective. However, AG deceleration is technically more challenging and so far no species with multiple conformers has been decelerated.

1.3 Outline of this thesis

This thesis describes how electric fields can be used for the quantum-state selection and conformer separation of large neutral molecules in supersonic jets. In Chapter 2, the theoretical background that is required to understand the interaction of polar asymmetric top molecules with DC electric fields is summarized. Chapter 3 describes the theory of AG focusing, how optimum electrode geometries for AG focusing can be found, and how an AG focuser can be operated under conditions that are best for conformer separation experiments. Furthermore, the numerical simulations that are employed to interpret the experimental data are outlined. In order to calculate the interaction of a molecule with electric fields, its rotational constants and its dipole moment components in the molecular frame have to be known. One method to obtain these molecular constants is Fourier-transform microwave spectroscopy in electric fields and Chapter 4 presents such experiments on 3-aminophenol. In Chapter 5, electrostatic molecular beam deflection experiments on benzonitrile and iodobenzene molecules are shown. Section 5.3 demonstrates how this method can be used to determine the rotational temperature of cold molecular beams and to quantum-state select large neutral molecules. When these quantum-state-selected molecules are used as targets, unprecedented degrees of laser-induced alignment and mixed-field orientation are achieved, as shown in Sections 5.4 and 5.5. In Chapter 6, the quantum-state selectivity of the electrostatic deflection process is exploited to spatially separate the cis and trans conformers of 3-aminophenol. Chapter 7 describes the implementation of an AC focuser and its application as a dipole moment to mass filter for neutral molecules. The setup of the machine is detailed in Section 7.2 and the focusing properties of the device are investigated in Section 7.3, where AG focusing experiments on ammonia in lfs and hfs quantum states are presented. Section 7.4 shows conformer-selection experiments on 3-aminophenol that are complementary to the results obtained with the electrostatic deflector. Then, in Section 7.5, it is experimentally demonstrated how the selectivity of the focuser can be improved by changing the duty cycle of the switching sequence. Finally, the different approaches to separate conformers are compared and an outlook on possible future experiments is given in Chapter 8.

Chapter 2

The asymmetric rotor

2.1 Introduction

In this work, asymmetric top molecules are manipulated with strong electric fields. In order to simulate the experiments, the populations of the individual quantum states and the forces acting on a molecule in a given quantum state have to be known. The population of a quantum state in the molecular beam depends on its field-free energy and the degeneracy of the energy level. The force acting on a molecule depends on its quantum-state-dependent Stark shift. This chapter summarizes the theoretical background that is required to understand the interaction of polar asymmetric top molecules with DC electric fields.

In quantum mechanics, the energy W of a molecule is calculated from the Schrödinger equation

$$H\Psi = W\Psi, \quad (2.1)$$

where H denotes the Hamiltonian in the center-of-mass frame and Ψ is the internal wave function. In the Born-Oppenheimer approximation [99], couplings between the motion of the nuclei and the motion of the electrons are neglected. If this approximation is valid and the Eckart conditions [100] are satisfied, the internal wavefunction can be written as the product of electronic, vibrational, rotational, and nuclear spin wave functions, which are denoted as $\Psi_{\text{el}}, \Psi_{\text{vib}}, \Psi_{\text{rot}},$ and $\Psi_{\text{ns}},$ respectively [101]:

$$\Psi = \Psi_{\text{el}} \Psi_{\text{vib}} \Psi_{\text{rot}} \Psi_{\text{ns}} \quad (2.2)$$

The total internal energy is then given by the sum of electronic (W_{el}), vibrational (W_{vib}), rotational (W_{rot}) and spin energies (W_{ns}):

$$W = W_{\text{el}} + W_{\text{vib}} + W_{\text{rot}} + W_{\text{ns}} \quad (2.3)$$

Because of the low temperatures (on the order of 1 K) achieved in supersonic jets, the molecules are practically all in the electronic and vibrational ground state. For large molecules with small rotational constants they remain, however, distributed over many rotational quantum states and it is important to calculate the field-free energies and Stark shifts of all of these individual states. This is summarized in Sections 2.2 and 2.4, respectively. W_{ns} is typically on the order of a MHz (see Chapter 4), much smaller than W_{rot} and the Stark energy even in modest fields, and can thus be neglected when calculating energies and forces for the purpose of this work. However, the spin wave functions have to be taken into account in the calculation of the populations of specific rovibronic quantum states, because their degeneracies determine the spin statistical weights, as will be discussed in Section 2.3.

2.2 The field-free asymmetric rotor

Asymmetric top molecules are characterized by three non-equal and non-zero principal moments of inertia I_a , I_b , and I_c . By convention, the principal axes a , b , and c are labelled such that $I_a < I_b < I_c$. In molecular spectroscopy often the rotational constants are used instead of the moments of inertia. The rotational constants, expressed in units of MHz, are defined as

$$A = \frac{h}{8\pi^2 I_a}, \quad B = \frac{h}{8\pi^2 I_b}, \quad C = \frac{h}{8\pi^2 I_c}, \quad (2.4)$$

with the moments of inertia in units of $\text{u} \cdot \text{\AA}^2$ and $h = 3.9903 \cdot 10^7 \text{u} \text{\AA}^2 \text{MHz}$. The asymmetry of a molecule can be characterized by Ray's asymmetry parameter $\kappa = \frac{2B-A-C}{A-C}$ [102], with $-1 \leq \kappa \leq 1$. For the most asymmetric molecules $\kappa = 0$. In the limit of $\kappa = 1$ ($A = B$) the molecule is an oblate symmetric top, whereas it is a prolate top for $\kappa = -1$ ($B = C$). The quantum-mechanical Hamiltonian describing the rotation of a rigid asymmetric rotor $H_{\text{rot}}^{\text{rigid}}$ can be expressed in terms of the operators of the components of the angular momentum P_a , P_b , and P_c about the principal axes [103, 104]:

$$H_{\text{rot}}^{\text{rigid}} = \frac{P_a^2}{2I_a} + \frac{P_b^2}{2I_b} + \frac{P_c^2}{2I_c} = \frac{4\pi^2}{h} (AP_a^2 + BP_b^2 + CP_c^2). \quad (2.5)$$

The Schrödinger equation for this Hamiltonian cannot be solved directly and no closed analytic form for the asymmetric rotor wave functions can be derived. It is possible, however, to expand the asymmetric rotor wave functions $|J_{K_a K_c} M\rangle$ in terms of symmetric rotor wave functions [103]:

$$|J_{K_a K_c} M\rangle = \sum_{J, K, M} a_{JKM} |J, K, M\rangle. \quad (2.6)$$

a_{JKM} are numerical constants and $|J, K, M\rangle$ are the symmetric top wave functions, whose explicit form is given elsewhere [103]. For the symmetric rotor the total angular momentum quantum number J , the quantum number characterizing the projection of the total angular momentum onto its figure axis K , and the quantum number characterizing the projection of the total angular momentum onto a space fixed Z -axis M are “good” quantum numbers. For an asymmetric rotor only the total angular momentum operator P^2 and its projection operator onto the Z -axis P_Z commute with H_{rot} . K is not a “good” quantum number anymore. Instead, pseudo quantum numbers, usually written as subscripts of J , are used to label the $(2J+1)$ distinct rotational sublevels for each value of J . Here, the double subscript system introduced by King et al. [105] is used. Each of the J -sublevels of the asymmetric rotor can be connected to two limiting symmetric top rotational states as κ evolves from -1 to 1 as shown in Figure 2.1. The K quantum numbers of these limiting symmetric top energy levels are used to label the asymmetric top states, where K_a (K_c) denotes the K quantum number of the limiting prolate (oblate) symmetric top quantum state. As shown in Figure 2.1, each symmetric top quantum state for $K \neq 0$ connects to two asymmetric top states. Whereas the symmetric top states with quantum numbers $|J, K, M\rangle$ and $|J, -K, M\rangle$ are degenerate, this degeneracy is lifted for the asymmetric rotor levels.

In order to determine the explicit energies of the asymmetric top rotational quantum states, the Hamiltonian is set up in the basis of symmetric top wavefunctions. There are six different possibilities to identify the principal axes of inertia a , b , and c with the molecule-fixed cartesian coordinates x, y , and z . Here the representation I' is used (see reference 103, Table 7.3). The non-vanishing matrix elements of the rigid-rotor Hamiltonian are [106]:

$$\langle J, K, M | H_{\text{rot}}^{\text{rigid}} | J, K, M \rangle = \frac{B+C}{2} (J(J+1) - K^2) + AK^2 \quad (2.7)$$

$$\begin{aligned} \langle J, K \pm 2, M | H_{\text{rot}}^{\text{rigid}} | J, K, M \rangle &= \left(\frac{B-C}{4} \right) \sqrt{J(J+1) - K(K \pm 1)} \\ &\cdot \sqrt{J(J+1) - (K \pm 1)(K \pm 2)} \end{aligned} \quad (2.8)$$

So far it has been assumed that the molecule is rigid. However, in particular for higher rotational quantum states, the molecule’s rigid body is distorted by centrifugal forces. An accurate description of these rotational states requires to include also centrifugal distortion constants in the field-free Hamiltonian. The Hamiltonian can then be written as

$$H_{\text{rot}} = H_{\text{rot}}^{\text{rigid}} + H_{\text{rot}}^{\text{cd}}, \quad (2.9)$$

where the matrix elements of $H_{\text{rot}}^{\text{cd}}$ accounting for the centrifugal distortion are,

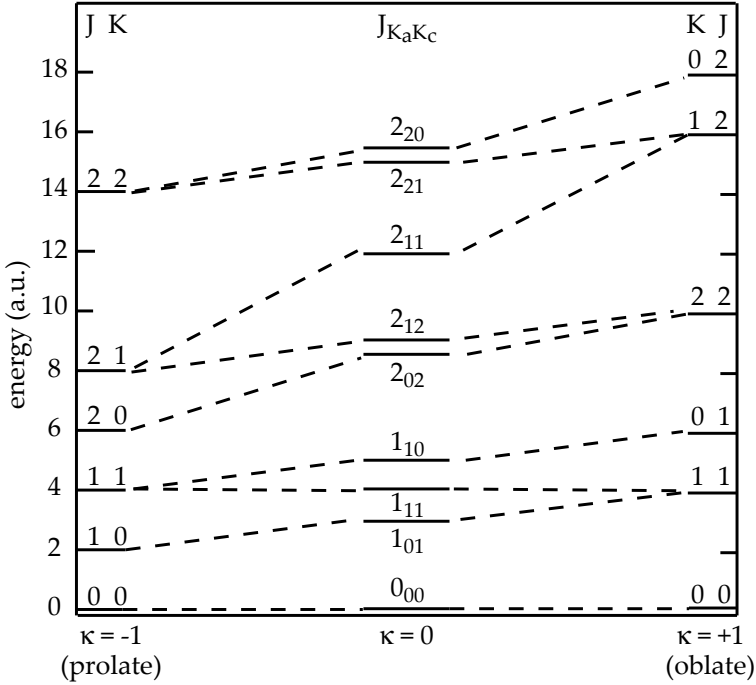


Figure 2.1: The rotational quantum states of asymmetric rotors are labelled by the pseudo quantum numbers K_a and K_c , which denote the symmetric top K quantum numbers of the limiting prolate and oblate symmetric top, respectively. Figure adopted from reference [103].

in Watson's A-reduction [107]:

$$\langle J, K, M | H_{\text{rot}}^{\text{cd}} | J, K, M \rangle = -\Delta_J J^2 (J+1)^2 - \Delta_{JK} J (J+1) K^2 - \Delta_K K^4 \quad (2.10)$$

$$\begin{aligned} \langle J, K \pm 2, M | H_{\text{rot}}^{\text{cd}} | J, K, M \rangle = & \left(-\delta_J J (J+1) - \frac{\delta_K}{2} \left((K \pm 2)^2 + K^2 \right) \right) \\ & \cdot \sqrt{J(J+1) - K(K \pm 1)} \\ & \cdot \sqrt{J(J+1) - (K \pm 1)(K \pm 2)} \end{aligned} \quad (2.11)$$

In principle, the energy levels of the field-free asymmetric rotor can be found by diagonalizing the Hamiltonian matrix in the basis of symmetric top wave functions. However, in order to determine if real or avoided crossings can occur between two given rotational quantum states in an electric field (see Section 2.4), the symmetry properties of the Hamiltonian have to be considered. The ellipsoid of inertia of an asymmetric top is symmetric under the identity operation E and under any rotation by 180° about its principal axis of inertia. These

symmetry	E	C_2^a	C_2^b	C_2^c
A	1	1	1	1
B_a	1	1	-1	-1
B_b	1	-1	1	-1
B_c	1	-1	-1	1

 Table 2.1: Character table of the Four-group $V(a, b, c)$.

rotations are designated as C_2^a , C_2^b , and C_2^c , respectively. The set of symmetry operations, E , C_2^a , C_2^b , and C_2^c , forms a group, which is called the Four-group $V(a, b, c)$ [103]. The Hamiltonian possesses the symmetry of the Four-group and every asymmetric top wave function can be classified according to its behaviour under the symmetry operations of V . The character table of the Four-group is shown in Table 2.1. Wave functions that belong to symmetry species A are symmetric under all operations of the Four-group. Symmetry species B_a corresponds to wave functions that are symmetric with respect to a rotation by 180° about the a -axis and antisymmetric with respect to rotations about b and c . Likewise, wave functions belonging to B_b (B_c) are symmetric with respect to rotations about b (c) and antisymmetric with respect to rotations about the other two principal axes. While the asymmetric top wave functions do belong to the Four-group, the symmetric top wave functions that have been used as the basis functions so far do not. It would be advantageous, however, to carry out the calculations of the rotational energy levels in a basis set that belongs to V . In this case, the Hamiltonian matrix could be factorized in blocks that only contain wave functions of the same symmetry and the resulting energy levels could easily be classified according to the symmetry species of the Four-group. Such a change of basis set can be achieved by applying a Wang transformation to obtain the symmetrized basis functions $|J, K, M, s\rangle$ [103, 108, 109]:

$$|J, K, M, s\rangle = \frac{1}{\sqrt{2}} (|J, K, M\rangle + (-1)^s |J, -K, M\rangle), \quad \text{for } K \neq 0 \quad (2.12)$$

$$|J, 0, M, 0\rangle = |J, 0, M\rangle, \quad \text{for } K = 0 \quad (2.13)$$

Here, K is always positive and s can be either 0 (for the symmetric Wang functions) or 1 (for the antisymmetric Wang functions). The Wang transformation can be expressed in matrix form. Introducing the Wang transformation matrix

X ,

$$X = X^{-1} = \tilde{X} = \frac{1}{\sqrt{2}} \begin{bmatrix} \ddots & & & & & & \\ & -1 & 0 & 0 & 0 & 1 & \\ & 0 & -1 & 0 & 1 & 0 & \\ \dots & 0 & 0 & \sqrt{2} & 0 & 0 & \dots \\ & 0 & 1 & 0 & 1 & 0 & \\ & 1 & 0 & 0 & 0 & 1 & \\ & \ddots & & & & & \ddots \end{bmatrix}, \quad (2.14)$$

which is of order $(2J + 1)$ for a given value of J , the change of basis can be written as $\Psi^{\text{Wang}} = \tilde{X}\Psi$. For fixed values of J and M , the vector Ψ consists of $(2J + 1)$ symmetric top basis functions, whereas Ψ^{Wang} is the vector of new basis functions that contains the $(2J + 1)$ symmetrized $|J, K, M, s\rangle$ -functions:

$$\Psi^{\text{Wang}} = \begin{pmatrix} |J, J, M, 1\rangle \\ |J, (J-1), M, 1\rangle \\ \vdots \\ |J, 1, M, 1\rangle \\ |J, 0, M, 0\rangle \\ |J, 1, M, 0\rangle \\ \vdots \\ |J, (J-1), M, 0\rangle \\ |J, J, M, 0\rangle \end{pmatrix}, \quad \Psi = \begin{pmatrix} |J, -J, M\rangle \\ |J, (-J+1), M\rangle \\ \vdots \\ |J, -1, M\rangle \\ |J, 0, M\rangle \\ |J, 1, M\rangle \\ \vdots \\ |J, (J-1), M\rangle \\ |J, J, M\rangle \end{pmatrix} \quad (2.15)$$

The Hamiltonian matrix in the new basis now factorizes into four sub-matrices that are historically denoted as E^+ , O^+ , E^- , and O^- [108, 109]:

$$H_{\text{rot}}^{\text{Wang}} = \tilde{X}H_{\text{rot}}X = E^+ + O^+ + E^- + O^- \quad (2.16)$$

The sub-matrices can be classified by the evenness and oddness of K and s , as shown in Table 2.2. Matrices that contain wave functions with even K are labelled E , those containing wave functions of odd K are labelled O . The superscript differentiates matrices with symmetric Wang functions (+) from those with antisymmetric Wang functions (-). The $|J, K, M, s\rangle$ wave functions within each individual sub-matrix all belong to the same symmetry species of V as pointed out by King, Hainer and Cross [105]. Therefore, Equation 2.16 can also be expressed in terms of A , B_a , B_b , and B_c

$$H_{\text{rot}}^{\text{Wang}} = H_A + H_{B_a} + H_{B_b} + H_{B_c}, \quad (2.17)$$

where H_Γ is a matrix containing only wave functions that belong to symmetry species Γ of V . The correlation between Equation 2.16 and Equation 2.17 is

Submatrix	K	s	J_{even}	J_{odd}
E^+	e	e	$A(\text{ee})$	$B_a(\text{eo})$
E^-	e	o	$B_a(\text{eo})$	$A(\text{ee})$
O^+	o	e	$B_c(\text{oe})$	$B_b(\text{oo})$
O^-	o	o	$B_b(\text{oo})$	$B_c(\text{oe})$

Table 2.2: Symmetry classification of the submatrices in $V(a, b, c)$ for representation I^r . The symmetry species of a rotational wave function is determined by the evenness or oddness of K_a and K_c , which is indicated in parentheses in columns 4 and 5.

given by Table 2.2 [103].

Applying the Wang transformation has two advantages. First, the size of the matrices to be diagonalized for the calculation of the field-free energy levels is reduced. Instead of the full J -matrix, only the four smaller sub-matrices of Equation 2.17 have to be diagonalized. Secondly, the Wang transformation allows for the classification of the rotational quantum states according to the symmetry species of V . This classification is important for the calculation of the adiabatic Stark curves, which will be discussed in detail in Section 2.4.

2.3 Nuclear spin statistical weights

In order to simulate an ensemble of molecules in a molecular beam, the relative populations of the individual rovibronic quantum states have to be calculated. If there are two identical atomic constituents in the molecule, i. e., symmetry-equivalent nuclei of the same isotope in identical chemical environments, then these populations will be influenced by nuclear spin statistics. For asymmetric top molecules there cannot be more than two symmetry-equivalent nuclei, but several pairs of such nuclei may occur. A physical observable must not change by the permutation of identical particles or, in other words, the Hamiltonian commutes with such a permutation operation [110, 111]. The permutation symmetry of any particle is conserved and a permutation of two identical fermions will always change the sign of the wave function, whereas a permutation of two identical bosons will not. Therefore, the complete internal wavefunction, which can be expressed in the Born-Oppenheimer approximation as the product of electronic, vibrational, rotational, and nuclear spin wave functions (see Equation 2.2), must be antisymmetric with respect to an odd number of permutations of identical fermions and symmetric with respect to an even number of such permutations. It will always be symmetric with respect to an arbitrary number of permutations of identical bosons [111]. A rovibronic wave function belonging to symmetry species Γ_{rve} can only be combined with nuclear spin wave functions of symmetry Γ_{ns} , if the product of their symmetries is an allowed symmetry

species for the complete internal wave function. Thus, the number of spin wave functions that a given rovibronic wave function can be combined with depends on its symmetry. This is the origin of nuclear spin statistical weights [111].

Figure 2.2 A shows the molecular structures of benzonitrile, iodobenzene, and 2,6-difluoroiodobenzene. These are planar molecules of $C_{2v}(M)$ symmetry that each have two pairs of identical fermions. A permutation of nuclei number 1 and 4 and a simultaneous permutation of nuclei number 2 and 3 is a symmetry operation and corresponds to a rotation by 180° about the a -axis, i. e., the symmetry operation C_a^2 of V . Because this operation involves two permutations of fermionic particles, the complete internal wave function must not change sign and, therefore, its symmetry species Γ_{int} has to be either A or B_a (see Table 2.1). Γ_{rve} is determined by the product of the symmetries of electronic wave function Γ_e , vibrational wave function Γ_v , and rotational wave function Γ_{rot} . At the cold temperatures in a molecular beam, the molecules relevant for this work are typically in the vibronic ground state $S_0(v=0)$. These electronic and the vibrational wave functions belong to symmetry species A (i. e., they are totally symmetric). Thus, Γ_{rve} is given by Γ_{rot} , which can be determined from the pseudo quantum numbers K_a and K_c as shown in Table 2.2. Rotational wave functions with even (odd) K_a are symmetric (antisymmetric) with respect to a rotation about the a -axis and have to be combined with a symmetric (antisymmetric) spin wave function to obtain a complete internal wave function of allowed symmetry.

The identical nuclei shown in Figure 2.2 are all fermions with spin $I = 1/2$. There are two possible projections of the spin relative to a space-fixed axis and thus two spin states per nucleus exist that are denoted as $|\uparrow\rangle$ and $|\downarrow\rangle$, respectively. The spin function of a pair of nuclei may be written as $|\uparrow\uparrow\rangle$, $|\downarrow\downarrow\rangle$, $|\uparrow\downarrow\rangle$, or $|\downarrow\uparrow\rangle$. While the first two spin functions are symmetric with respect to a permutation of the nuclei, the latter two are neither symmetric nor antisymmetric. It is, however, possible to construct symmetric or antisymmetric spin functions in the following way [112]:

$$|\uparrow\downarrow\rangle + |\downarrow\uparrow\rangle \quad (\text{symmetric}) \quad (2.18)$$

$$|\uparrow\downarrow\rangle - |\downarrow\uparrow\rangle \quad (\text{antisymmetric}) \quad (2.19)$$

Thus for two spin $1/2$ particles, three symmetric and one antisymmetric spin functions can be constructed. In general, for a nucleus with spin I there are $(2I + 1)$ possible projections of the spin onto a space fixed axis. The number of symmetric spin functions that can be constructed for a pair of such nuclei is [112]

$$n_s = (2I + 1)(I + 1), \quad (2.20)$$

whereas the number of antisymmetric spin functions is

$$n_a = (2I + 1)I. \quad (2.21)$$

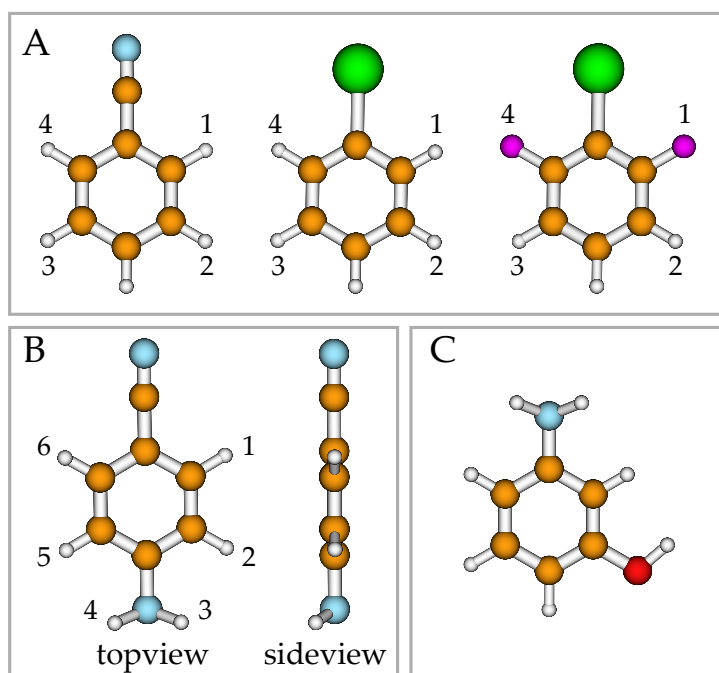


Figure 2.2: Molecular structures of asymmetric top molecules relevant for this thesis. Atomic constituents are shown in different colors, where hydrogen is shown in grey, carbon in orange, nitrogen in blue, oxygen in red, iodine in green, and fluorine in magenta. Fermionic nuclei that have identical counterparts are numbered. A) From left to right: benzonitrile, iodobenzene, and 2,6-difluoriodobenzene all have 2 pairs of identical fermions. B) para-aminobenzonitrile has 3 pairs of identical fermions. C) trans-3-aminophenol has no pair of identical fermions.

Now let there be two pairs of identical nuclei in the molecule. Let $n_{s,i}$ be the number of symmetric spin functions and $n_{a,i}$ the number of antisymmetric spin functions for pair i , where $i = 1, 2$. The product of the spin functions will give $n_{s,1}n_{s,2} + n_{a,1}n_{a,2}$ symmetric and $n_{s,1}n_{a,2} + n_{a,1}n_{s,2}$ antisymmetric spin wave functions. A general expression for the number of symmetric spin wave functions for m pairs of identical nuclei can be derived [112]:

$$n_s = \frac{1}{2} \left[\prod_{j=1}^m (2I_j + 1) \right] \left[\prod_{j=1}^m (2I_j + 1) + 1 \right] \quad (2.22)$$

The corresponding number of antisymmetric wave functions is

$$n_a = \frac{1}{2} \left[\prod_{j=1}^m (2I_j + 1) \right] \left[\prod_{j=1}^m (2I_j + 1) - 1 \right]. \quad (2.23)$$

Thus, for the molecules shown in Figure 2.2 A, there are 10 symmetric spin wave functions to be combined with symmetric rotational wave functions and 6 antisymmetric spin wave functions to be combined with antisymmetric spin wave functions. In this way the nuclear spin statistical weights that are listed in Table 2.3 are obtained.

Figure 2.2 B shows the molecular structure of para-aminobenzonitrile ($C_{2v}(M)$ symmetry). The calculated equilibrium structure yields out-of-plane positions for the two hydrogen atoms of the amino group that are labelled 3 and 4 [106]. However, the inversion tunnelling rate of the two amino hydrogens is expected to be similar to the one of aniline (1 THz) [113] and much faster than the timescale of the molecular rotation. Therefore, the averaged structure over one rotational period is expected to be planar. In this time-averaged structure three pairs of identical fermions occur and Γ_{int} has to be antisymmetric with respect to simultaneous permutations of all identical nuclei. The resulting spin statistical weights are calculated as described before and are also given in Table 2.3. Finally, 3-aminophenol, which is depicted Figure 2.2 C, has no pair of identical nuclei and thus nuclear spin statistics does not influence the relative populations of the rovibronic quantum states.

2.4 Stark effect of the asymmetric rotor

The shifting and splitting of molecular energy levels caused by an external electric field \vec{E} , which here is taken to be directed along the space-fixed Z-axis, is known as the Stark effect. For large asymmetric top molecules, the Stark effect is due to mixing of closely spaced rotational quantum states of the same symmetry. Because the field couples states with $\Delta M = 0$ and $\Delta J = 0, \pm 1$, M remains as the only good quantum number in an electric field. States with

molecule	formula	n_{pairs}	$g_{ns}(ee, eo)$	$g_{ns}(oo, oe)$
3-aminophenol	C_6H_7NO	0	1	1
benzotrile	C_7H_5N	2	5	3
iodobenzene	C_6H_5I	2	5	3
2,6-difluoriodobenzene	$C_6H_3F_2I$	2	5	3
p-aminobenzotrile	$C_7H_6N_2$	3	7	9

Table 2.3: Chemical formula, number of pairs of identical fermions n_{pairs} , and resulting relative nuclear spin statistical weights g_{ns} for rotational energy levels of relevant asymmetric top molecules. The labels in parentheses denote the parities of K_a and K_c .

$M = 0$ are singly degenerate, whereas states with $M \neq 0$ are doubly degenerate. The rotational Hamiltonian in the presence of an electric field $H_{\text{rot,E}}$ can be written as the sum of the field-free Hamiltonian (see Equation 2.9) and the Stark-contribution H_{Stark} :

$$H_{\text{rot,E}} = H_{\text{rot}} + H_{\text{Stark}} \quad (2.24)$$

For molecules with a permanent electric dipole moment $\vec{\mu}$, H_{Stark} can be expressed in terms of the direction cosines (i. e., the projections of the principal axes onto the field direction) $\Phi_{Z\alpha}$ [103]:

$$H_{\text{Stark}} = -\vec{\mu}\vec{E} = -E \sum_{\alpha=a,b,c} \mu_{\alpha}\Phi_{Z\alpha} =: \sum_{\alpha=a,b,c} H_{\text{Stark}}^{\alpha} \quad (2.25)$$

Here, μ_{α} are the components of $\vec{\mu}$ along the principal axes, E is the magnitude of the electric field, and $H_{\text{Stark}}^{\alpha}$ is the contribution of μ_{α} to H_{Stark} . The corresponding non-zero matrix elements of H_{Stark} in the basis of prolate symmetric top wave functions are [106, 107]: *

$$\langle J, K, M | H_{\text{Stark}}^a | J, K, M \rangle = -\frac{MK}{J(J+1)}\mu_a E \quad (2.26)$$

$$\begin{aligned} \langle J+1, K, M | H_{\text{Stark}}^a | J, K, M \rangle &= \langle J, K, M | H_{\text{Stark}}^a | J+1, K, M \rangle \\ &= -\frac{\sqrt{(J+1)^2 - K^2} \sqrt{(J+1)^2 - M^2}}{(J+1) \sqrt{(2J+1)(2J+3)}} \mu_a E \end{aligned} \quad (2.27)$$

*Note that in reference 106 representation l^l is used

$$\langle J, K \pm 1, M | H_{\text{Stark}}^b | J, K, M \rangle = -\frac{M \sqrt{(J \mp K)(J \pm K + 1)}}{2J(J + 1)} \mu_b E \quad (2.28)$$

$$\begin{aligned} \langle J + 1, K \pm 1, M | H_{\text{Stark}}^b | J, K, M \rangle &= \langle J, K \pm 1, M | H_{\text{Stark}}^b | J + 1, K, M \rangle \\ &= \pm \frac{\sqrt{(J \pm K + 1)(J \pm K + 2)} \sqrt{(J + 1)^2 - M^2}}{2(J + 1) \sqrt{(2J + 1)(2J + 3)}} \mu_b E \end{aligned} \quad (2.29)$$

$$\langle J, K \pm 1, M | H_{\text{Stark}}^c | J, K, M \rangle = \pm i \frac{M \sqrt{(J \mp K)(J \pm K + 1)}}{2J(J + 1)} \mu_c E \quad (2.30)$$

$$\begin{aligned} \langle J + 1, K \pm 1, M | H_{\text{Stark}}^c | J, K, M \rangle &= \langle J, K \pm 1, M | H_{\text{Stark}}^c | J + 1, K, M \rangle \\ &= -i \frac{\sqrt{(J \pm K + 1)(J \pm K + 2)} \sqrt{(J + 1)^2 - M^2}}{2(J + 1) \sqrt{(2J + 1)(2J + 3)}} \mu_c E \end{aligned} \quad (2.31)$$

In order to calculate the Stark energies, $H_{\text{rot,E}}$ is set up for each M individually including all $|J, K, M\rangle$ -states for $J < J_{\text{max}}$ and subsequently Wang-transformed according to Equation 2.16. If the molecule's dipole moment is parallel to the principal axis of inertia α , then the Hamiltonian matrix is factorized into two sub-matrices H_1 and H_2 by this transformation according to the remaining symmetry in the field:

$$H_{\text{rot,E}}^{\text{Wang}} := \tilde{X} H_{\text{rot,E}} X = H_1 + H_2 \quad (2.32)$$

This factorization can be understood from the symmetry properties of the direction cosines [103]. $\Phi_{Z\alpha}$ does not change sign under the Four-group operations C_2^α and E , whereas it changes sign under the operations $C_2^{\alpha'}$, with $\alpha' \neq \alpha$. In other words, it transforms according to symmetry species B_α (see Table 2.1). The integral $\langle J, K, M, s | \Phi_{Z\alpha} | J', K', M', s' \rangle$ can only be non-zero, if it remains unchanged by any operation that transforms the system into a configuration that is indistinguishable from the original, i. e., if the integral belongs to symmetry species A . Therefore, only matrix elements between states whose symmetry products equal the symmetry of $\Phi_{Z\alpha}$ are non-zero.

From the multiplication table of V (see Table 2.4) it can be seen that in order to achieve this, either states of symmetry A can be combined with states of symmetry B_α or states of symmetry $B_{\alpha'}$ can be combined with states of symmetry $B_{\alpha''}$, where $\alpha \neq \alpha' \neq \alpha'' \neq \alpha$. In summary, the Wang transformation factorizes the Hamiltonian matrix into two submatrices, where the matrix H_1 contains only states of symmetry species A and B_α , whereas the matrix H_2 contains only states that belong to the remaining two symmetry species of V . These two sub-matrices are independently diagonalized, which ensures that only states of the same symmetry are coupled and that real and avoided crossings of states can be distinguished. Within each sub-matrix all crossings

	<i>A</i>	<i>B_a</i>	<i>B_b</i>	<i>B_c</i>
<i>A</i>	<i>A</i>	<i>B_a</i>	<i>B_b</i>	<i>B_c</i>
<i>B_a</i>	<i>B_a</i>	<i>A</i>	<i>B_c</i>	<i>B_b</i>
<i>B_b</i>	<i>B_b</i>	<i>B_c</i>	<i>A</i>	<i>B_a</i>
<i>B_c</i>	<i>B_c</i>	<i>B_b</i>	<i>B_a</i>	<i>A</i>

Table 2.4: Multiplication table of the Four-group $V(a, b, c)$.

are avoided and the energetic order of the states is always the same. For the correct assignments of the states to the adiabatically corresponding field-free rotor states, first the field-free energies are calculated for $J < J_{\max}$ as described in Section 2.2. Then, the field-free states are sorted by energy and assigned to either H_1 or H_2 depending on their Four-group symmetry. This assignment is straightforward, since it is easily determined from the evenness or oddness of K_a and K_c which energy level may be found in which sub-matrix (see Table 2.2). Now that the order of states within each sub-matrix is known, the correct “adiabatic quantum number labels” $\tilde{J}_{\tilde{K}_a\tilde{K}_c}\tilde{M}$ can be assigned to the rotational quantum states in an electric field.

If the dipole moment is not parallel to a principal axis, then no factorization of $H_{\text{rot,E}}$ is possible and the full Hamiltonian matrix must be diagonalized. In this case, the individual rotational states all have the same symmetry and no real crossings between individual states can occur. The energetic order of states is always the same and can be obtained from the calculation of the field-free energies as described above. Thus, the assignment of $\tilde{J}_{\tilde{K}_a\tilde{K}_c}\tilde{M}$ is straightforward. (For simplicity, in the remaining text the field-free quantum numbers $J_{K_aK_c}M$ will be used to label the corresponding quantum states in the electric field).

In practice, the calculation of the Stark energies is performed for a number of electric field strengths – typically in steps of 1 kV/cm from 0 kV/cm to 200 kV/cm – and the resulting energies are stored for later use in simulations using the libcoldmol program package [115]. As a typical example, the calculated Stark curves for the lowest-lying rotational quantum states of p-aminobenzonitrile, whose molecular structure is illustrated in Figure 2.2 B, are shown in Figure 2.3. The dipole moment of p-aminobenzonitrile is directed along the a -axis. Quantum states that belong to symmetry species A and B_a are found in H_1 and are shown in black in Figure 2.3. States of B_b and B_c symmetries that are found in H_2 are shown in blue. The typical electric field strengths that are applied in this work to manipulate the motion of the molecules are on the order of 100 kV/cm. At these field strengths the Stark curves of all low-lying states have a negative slope. Typically, the effective dipole moment μ_{eff} is introduced as

$$\mu_{\text{eff}}(E) = -\frac{\partial W}{\partial E} \quad (2.33)$$

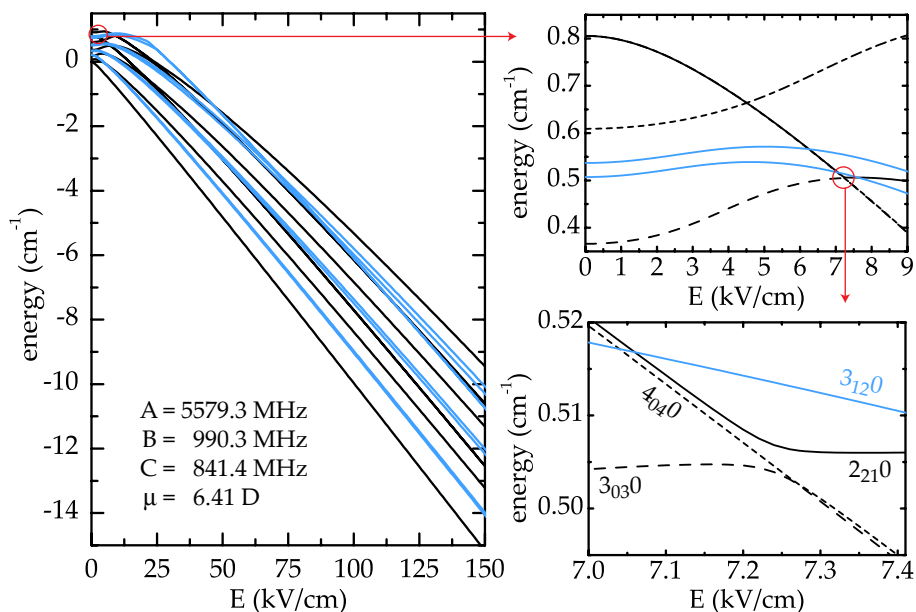


Figure 2.3: The Stark-curves for the lowest rotational quantum states of p-aminobenzonitrile. The two symmetry species that remain in the electric field are shown in different colors. In the inset the molecular constants are given [114]. On the right hand side, the Stark curves in the region indicated by the red circles are shown on an enlarged scale.

Molecules in states with $\mu_{\text{eff}} > 0$ feel a force towards regions of high electric field strength and are, therefore, called high-field seeking. Analogously, molecules in quantum states with a negative μ_{eff} are called low-field seeking. On the right hand side of Figure 2.3 some of the Stark curves are shown on an enlarged scale for small electric field strengths. At these fields many avoided crossings occur between neighbouring states of the same symmetry. While at small electric field strengths both hfs and lfs quantum states exist, the avoided crossings ultimately turn any lfs quantum state into a hfs state at high electric field strength. This ultimate turning point shifts to higher electric fields with increasing rotational energy. The effective dipole moments for the quantum states shown on the left hand side of Figure 2.3 are illustrated in Figure 2.4. While μ_{eff} changes rapidly at small electric field strengths, it becomes almost constant at fields larger than 100 kV/cm (at least for the low-lying states shown here). At infinitely high electric fields, the effective dipole moments of all states converge to the value of the permanent dipole moment $\mu = 6.41$ D [114], which is indicated as the red

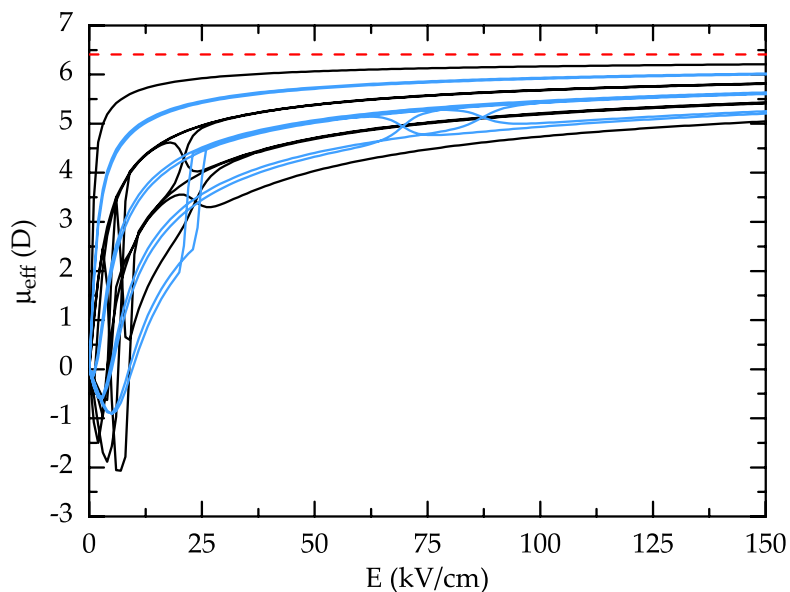


Figure 2.4: The effective dipole moments for the lowest rotational quantum states of p-aminobenzonitrile. The two distinct symmetry species that exist in the electric field are shown in black and blue. The red dashed line indicates the value of the permanent dipole moment $\mu = 6.41$ D [114].

dashed line in Figure 2.4. [†]

[†]A dipole moment of 1 D corresponds to $0.0168 \text{ cm}^{-1}/(\text{kV cm}^{-1})$.

Chapter 3

Alternating gradient focusing

3.1 Introduction

Electrostatic multipole fields have been used for decades to focus beams of small molecules in low-field-seeking quantum states. These focused beams have proven to be extremely beneficial for a large variety of experiments, as described in Chapter 1. Gaining similar control over large molecules is more difficult, because these molecules are in high-field-seeking quantum states at the practically relevant electric field strengths and cannot be focused using electrostatic multipole fields. The situation is analogous to the one in charged particle physics; also ions cannot be confined with static fields alone. Here, the problem was solved using dynamic focusing schemes, usually referred to as “alternating gradient (AG) focusing”. In the following sections its application to neutral polar molecules will be discussed. This has been proposed by Auerbach, Bromberg, and Wharton [50] and was discussed recently in detail in the context of AG deceleration [68] and AG focusing [116] of polar molecules. The basic principles outlined in said references shall be summarized in this chapter.

3.2 General principles

Polar molecules experience a force \vec{F} in an inhomogeneous electric field due to the spatial variation of their potential energy. This force can be used to keep a polar molecule on a stable trajectory around $\vec{r} = 0$, where \vec{r} denotes the molecule’s position in the laboratory frame, if two prerequisites are fulfilled. The force must vanish at $\vec{r} = 0$ and, for small spatial deviations, the force must restore the molecule’s position towards $\vec{r} = 0$. The latter requirement is fulfilled

if the divergence of the force field is negative, i. e. , $\vec{\nabla} \cdot \vec{F} \leq 0$ is required.* The properties of the force that an inhomogeneous electric field exerts on a polar molecule shall be investigated here. This force is given by the negative gradient of the Stark energy W_{Stark} , which depends on the magnitude of the electric field $E = |\vec{E}|$:

$$\vec{F}(\vec{r}) = -\vec{\nabla}W_{\text{Stark}}(E) \quad (3.1)$$

For molecules with a linear Stark effect, the Stark energy can be written as

$$W_{\text{Stark}} = -\mu_{\text{eff}} E. \quad (3.2)$$

The effective dipole moment μ_{eff} depends on the molecule's quantum state and is defined in Equation 2.33. In a region devoid of charges the electric field may be written as the negative gradient of a scalar potential Φ , which satisfies Laplace's equation, i. e. , $\vec{\nabla}^2\Phi = 0$:

$$\vec{E}(\vec{r}) = -\vec{\nabla}\Phi(\vec{r}) \quad (3.3)$$

Written in components and using Equation 3.2, the force can then be expressed as:

$$F_j = \frac{\mu_{\text{eff}}}{E} \sum_{i=1}^3 \left(\frac{\partial\Phi}{\partial x_i} \right) \left(\frac{\partial^2\Phi}{\partial x_i \partial x_j} \right) \quad (3.4)$$

The divergence of the force field $\vec{\nabla} \cdot \vec{F}$ is given by:

$$\sum_{j=1}^3 \frac{\partial F_j}{\partial x_j} = \frac{\mu_{\text{eff}}}{E^3} \sum_{i,j,k=1}^3 \left[\left(\frac{\partial\Phi}{\partial x_k} \right)^2 \left(\frac{\partial^2\Phi}{\partial x_i \partial x_j} \right)^2 - \left(\frac{\partial\Phi}{\partial x_k} \right) \left(\frac{\partial\Phi}{\partial x_i} \right) \left(\frac{\partial^2\Phi}{\partial x_i \partial x_j} \right) \left(\frac{\partial^2\Phi}{\partial x_k \partial x_j} \right) \right] \quad (3.5)$$

Exploiting Schwarz's inequality,

$$\left(\sum_{i=1}^n x_i y_i \right)^2 \leq \left(\sum_{i=1}^n x_i^2 \right) \left(\sum_{i=1}^n y_i^2 \right) \quad \text{for } x_i, y_i \in \mathbb{R}, \quad (3.6)$$

it is seen that the sum in the right hand part of Equation 3.5 is always positive and, therefore, the sign of μ_{eff} determines the sign of $\vec{\nabla} \cdot \vec{F}$. For molecules in low-field-seeking quantum states μ_{eff} is negative and focusing is readily achieved using static electric fields. For molecules in high-field-seeking quantum states μ_{eff} is positive and focusing is more difficult. The situation is analogous to the manipulation of ions with electric fields, where $\vec{\nabla} \cdot \vec{F} = q\vec{\nabla} \cdot \vec{E}$ with q being the charge of the ion. In this case, the divergence of the force field is zero in free space and electrostatic fields alone cannot be used to confine the particles.

*This condition is necessary but not sufficient for focusing. Even for $\vec{\nabla} \cdot \vec{F} \leq 0$ a particle's trajectory might become unstable if parametric amplification of the transverse motion occurs [117].

However, focusing and trapping of charged particles can still be achieved using dynamic focusing schemes. This principle is exploited, for instance, in quadrupole mass filters [47, 48] and accelerators [45] for charged particles. The basic idea is to create an array of electrostatic lenses that focus the particles along one transverse coordinate while defocusing it along the orthogonal transverse axis. Alternating the orientation of these fields at the appropriate frequency results in a net focusing force along both transverse coordinates. On average, the molecules are further away from the molecular beam axis in focusing lenses than in defocusing lenses. Since the force the particle experiences increases with the distance from the beam axis, the focusing force is on average larger than the defocusing force. Using the same idea, also three dimensional confinement can be achieved in Paul traps [47, 49]. Because the particle’s motion itself stabilizes its trajectory, this focusing is also referred to as “dynamic focusing”. The application of this method to neutral molecules has been theoretically proposed by Auerbach et al. [50] and it has been experimentally demonstrated for the first time by Kakati and Lainé [51] in the alternating gradient focusing of ammonia in high-field-seeking quantum states, and in numerous experiments since then [57, 67, 69, 70, 73, 118].

3.3 Electrode geometries

In Section 3.2, the principle of alternating gradient focusing has been introduced. Now it shall be discussed how to find electrode geometries that are suitable for AG focusing. Ideally, these electrodes result in an harmonic interaction potential in order to minimize focusing aberrations. For molecules with a linear Stark shift and a constant μ_{eff} , the ideal electric field is also harmonic: $E(x, y) \propto (x^2 - y^2)$. The discussion presented here will be limited to the 2-dimensional case assuming infinitely long electrodes with a constant electric field along the z -axis. This simplification is well justified within the context of this work, because for the 1 m-long m/μ -selector described in Chapter 7, the electric field typically is switched on and off when the molecules are inside the high-voltage electrodes. Thus, in contrast to, for instance, an AG decelerator [68], where the fringe fields of electrostatic lenses are used to manipulate the molecule’s longitudinal velocity, here the molecule does not see the fringe fields of the electrodes at all and the electric field can indeed be considered to be constant along z .

It is instructive to start with the multipole expansion of the electrostatic potential in two dimensions. This is the most general form of the electric potential that is consistent with Laplace’s equation and can be written in cylindrical coordinates, with $r = \sqrt{x^2 + y^2}$ and $\theta = \tan^{-1}(y/x)$, as:

$$\Phi(r, \theta) = \Phi_0 \left[\sum_{n=1}^{\infty} \frac{a_n}{n} \left(\frac{r}{r_0} \right)^n \cos(n\theta) + \sum_{n=1}^{\infty} \frac{b_n}{n} \left(\frac{r}{r_0} \right)^n \sin(n\theta) \right] \quad (3.7)$$

Here, a_n and b_n are dimensionless constants, r_0 is a characteristic lengthscale for the chosen electrode geometry and Φ_0 is a constant that characterizes the voltage applied to the electrodes. Φ_0 is related to the magnitude of the electric field strength on the molecular beam axis E_0 by $E_0 = (\Phi_0/r_0)\sqrt{a_1^2 + b_1^2}$. The magnitude of the desired electric field should be non-zero at the origin because a maximum of the electric field along one spatial direction and a minimum along the perpendicular axis is needed. Furthermore, the magnitude of the electric field should be symmetric under reflection about the x - and y -axis in order to create a good lens. In order to achieve this, the electric potential is made symmetric with respect to a reflection about the x -axis and anti-symmetric with respect to a reflection about the y -axis. Such a potential is obtained by setting all $b_n = 0$ and keeping only the odd a_n -terms of Equation 3.7. Higher order terms in the multipole expansion will introduce focusing aberrations (*vide infra*) and are undesired. Keeping only the leading a_1, a_3 , and a_5 terms and using $x = r \cos(\theta)$ and $y = r \sin(\theta)$, the multipole expansion can be written in cartesian coordinates:

$$\Phi(x, y) = \Phi_0 \left(a_1 \frac{x}{r_0} + a_3 \frac{(x^3 - 3xy^2)}{3r_0^3} + a_5 \frac{(x^5 - 10x^3y^2 + 5xy^4)}{5r_0^5} \right) \quad (3.8)$$

From this potential the magnitude of the electric field, $E(x, y) = |\vec{E}(x, y)|$, is obtained by calculating its derivative with respect to x and y :

$$E(x, y) = \sqrt{\left(\frac{\partial\Phi}{\partial x}\right)^2 + \left(\frac{\partial\Phi}{\partial y}\right)^2} \quad (3.9)$$

For small deviations from the molecular beam axis, i. e. , for $r < r_0$, and under the assumption that $a_1 \gg a_3 \gg a_5$, the electric field can be expanded as a power series:

$$E(x, y) = E_0 \left(1 + \frac{a_3}{a_1} \frac{(x^2 - y^2)}{r_0^2} + 2 \left(\left(\frac{a_3}{a_1}\right)^2 - 3\frac{a_5}{a_1} \right) \frac{x^2y^2}{r_0^4} + \frac{a_5}{a_1} \frac{(x^4 + y^4)}{r_0^4} \dots \right) \quad (3.10)$$

Equation 3.10 shows that the two leading terms of the expansion have the desired form for AG focusing and that the higher terms indeed introduce focusing aberrations. The harmonic term that provides the focusing is of order a_3/a_1 , while the first anharmonic terms are of order $(a_3/a_1)^2$ and a_5/a_1 , respectively. Thus, for the desired AG focusing potential, a_5 vanishes while a_3 is chosen such that it is large enough to provide sufficient focusing and at the same time small enough to prevent detrimental aberration effects. The strategy to find the best electrode geometry follows the one outlined in [68]: First of all, the equipotential lines of the desired electric potential are plotted. Then, electrode shapes are sought that match these equipotentials as closely as possible. Finally,

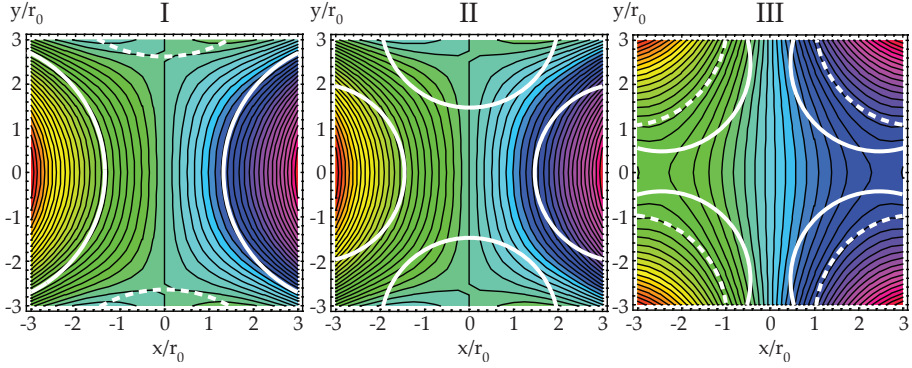


Figure 3.1: Contour plots of the electric potentials suitable for alternating gradient focusing. Figures I and II correspond to $a_3/a_1 = 1/7$, whereas Figure III is calculated for $a_3/a_1 = -1/7$. The white lines indicate round electrode shapes that approximate the equipotentials. The electrodes used in this work are shown as solid white lines in Figures II and III.

the potential created by the chosen electrodes is calculated numerically and fitted to the multipole expansion (Equation 3.8) in order to determine the expansion coefficients a_1 , a_3 , and a_5 . This procedure is repeated until the optimal electrode geometry is found that results in favourable expansion coefficients for AG focusing.

The sign of a_3/a_1 can be freely chosen and Figure 3.1 shows contour plots of electrostatic potentials with $a_3/a_1 = 1/7$ (Figure 3.1 I and II) and $a_3/a_1 = -1/7$ (Figure 3.1 III) together with round electrode shapes that approximate the equipotential lines. The white solid lines in Figure 3.1 represent two cylindrical electrodes of radius $3r_0$ at a high voltage of $\pm V_0$ with their surfaces separated by a gap of $2r_0$. Such electrodes with $V_0=10-20$ kV and $r_0 = 1$ mm have been used in the recently demonstrated AG-decelerator experiments [67, 69, 70]. A fit to the numerically calculated potential yields $a_3/a_1 = a_5/a_3 = 0.143$. Obviously the electrodes do not perfectly match the equipotentials and, therefore, higher order terms appear in the fitted multipole expansion. Introducing two grounded electrodes indicated by the dashed lines in Figure 3.1 I results in more favourable ratios of $a_3/a_1 = 0.157$ and $a_5/a_3 = 0.070$ as pointed out by Bethlem et al. [68].

In order to achieve dynamic focusing, the electric field has to be rotated by 90° in subsequent electrostatic lenses. This rotation can be achieved in different ways. For instance, an array of short cylindrical electrodes that match the contours of the electrodes shown in Figure 3.1 can be used, where subsequent lenses are physically rotated in space. In this case, the high voltages applied to the electrodes do not necessarily have to be switched and focusing can be achieved through the molecules' forward velocity. This approach has been

used, for instance, in early AG focusing experiments on ammonia [51, 52] and KF [55]. In the technically more challenging setup of the alternating gradient decelerator [67, 69, 70], the focusing strength per lens can be additionally tuned by rapidly switching the high voltages on and off while the molecule is inside a single lens.

Alternatively, symmetric electrode geometries can be implemented, for which focusing and defocusing planes can be freely chosen by changing the voltages applied to the electrodes. In this case, long electrodes without gaps can be used and alternating gradient focusing is achieved by switching between two electric field configurations that are rotated by 90° with respect to each other. This approach has been used for filtering slow ammonia molecules from an effusive source [57] and it has also been implemented in this work. One suitable symmetric electrode geometry consists of four cylindrical electrodes of radius $2.3 r_0$ placed at the corners of a square with sides of length $3 r_0$ (dashed lines in Figure 3.1 III). These electrodes nicely match the equipotentials for $a_3/a_1 = -1/7$ and result in very favourable fitting parameters for AG focusing of $a_3/a_1 = -0.14$ and $a_5/a_3 = -0.015$. However, the magnitude of the electric field on the molecular beam axis is quite weak for this electrode geometry, because the distances of the surfaces of the electrodes from $x = y = 0$ are relatively large. The discussion of the harmonicity of the interaction potential presented here is based on the assumption that the effective dipole moment μ_{eff} is constant with respect to E . In the discussion of the Stark effect of asymmetric tops in Chapter 2, it has been shown that, for large molecules, this assumption is only valid for strong electric fields. Therefore, not only the shape of the electric field but also its magnitude plays an important role in the discussion of the harmonicity of the interaction potential. The actual electrode geometry chosen for this work represents a compromise between a potential that results in a harmonic field on the one hand, and a maximum field strength on the molecular beam axis on the other hand. The electrodes of the m/μ -selector built in this work have a radius $R = 2 r_0$, the spacing between opposing electrodes is $3 r_0$, and the gap between neighbouring electrodes is $0.94 r_0$. These electrodes are indicated by solid lines in Figure 3.1 II and III. If two opposing electrodes are switched to $\pm V_0$ and the other two at ground, a potential with a positive value of a_3/a_1 is approximated (see Figure 3.1 II) and fitting a multipole expansion yields $a_3/a_1 = 0.349$ and $a_5/a_3 = -0.070$. If two neighbouring electrodes are switched to V_0 and the other two at ground, a potential with a negative value of a_3/a_1 is approximated (see Figure 3.1 III) and fitting a multipole expansion yields $a_3/a_1 = -0.34$ and $a_5/a_3 = -0.172$. Even though the fitting parameters are slightly worse for the latter case, this geometry has been chosen for the experiments presented in this work for technical reasons.[†]

[†]Only one high-voltage power supply is needed for the case $a_3/a_1 < 0$. Furthermore, the probability for discharges between the high-voltage electrodes is smaller, when only positive high voltages are applied to the electrodes. Because such discharges caused problems during setup of the experiment, only the configuration with $a_3/a_1 < 0$ was used.

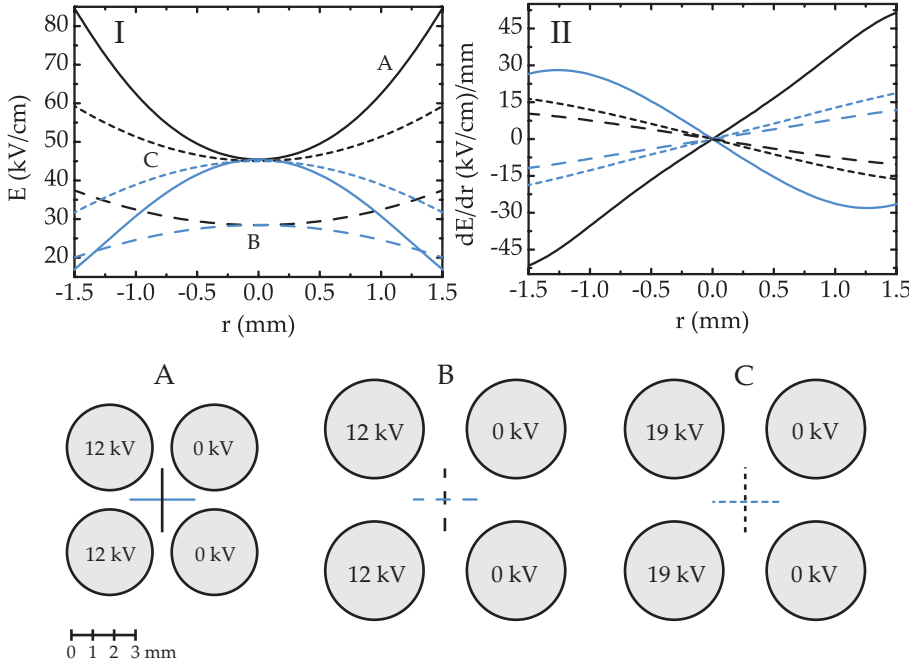


Figure 3.2: Comparison of the magnitude of the electric field (I) and its gradient (II) along the x - and y -axis for different electrode geometries. The cuts through the electric fields that are shown in Figures I and II are indicated by straight lines of the same color and style in Figures A-C.

Figure 3.2 I compares the electric field close to the molecular beam axis for the electrodes used in this work (A) and the electrodes that yield optimal fitting parameters (B and C, for which $a_3/a_1 = 0.349$ and $a_5/a_3 = -0.070$). For $V_0 = 12$ kV and $r_0 = 1$ mm the electric field in the center is 45 kV/cm for electrodes A and only 28 kV/cm for electrodes B. The same magnitude of the electric field in the center as in case A is obtained, when electrodes B are switched to 19 kV instead of 12 kV. However, the resulting gradient of the electric field is still smaller compared to case A, as shown in Figure 3.2 II, due to the small value of a_3/a_1 of electrodes B and C. This gradient determines the force in the equations of motion (see Section 3.5) and thus the switching frequency required for dynamic focusing. Due to the finite length of the m/μ -selector, the selectivity of the device increases with the number of switching cycles that the molecules experience. Furthermore, a larger field gradient results in higher overall transmission. A large gradient of the electric field and the resulting high switching frequency is, therefore, desirable for optimal performance of the

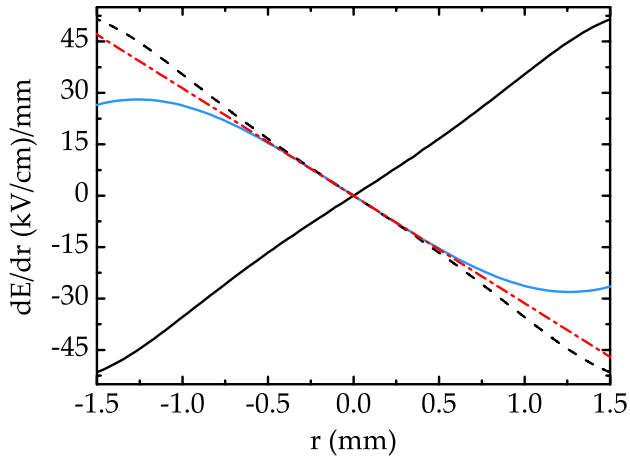


Figure 3.3: Gradient of the electric field strength along the y -axis (black solid line) and along the x -axis (blue line). For comparison, also the negative gradient along the y -axis (black dashed line) and a linear fit to the gradient along the x -axis in the center (red dash-dotted line) are shown.

selector and another argument in favor of the chosen electrode geometry.

Alternating gradient focusing works best, if the focusing and defocusing forces are of equal strength. In order to see in how far this condition is fulfilled for the chosen electrode geometry, the gradient of the electric field along the x - and y -axis and the negative gradient of the electric field along the y -axis are plotted in Figure 3.3. Also shown is a linear fit to the gradient along the x -axis for small deviations from the beam axis. Within the central 1 mm around the origin, focusing and defocusing forces are of equal strength and nicely follow the straight line resulting from the linear fit (red line in Figure 3.3). Further away from the molecular beam axis, both gradients deviate from the ideal linear behaviour and the gradient along the y -axis becomes stronger than the gradient along the x -axis. The influence of this deviation from the linear curve on the transmission of a molecule depends on the sign of μ_{eff} . For low-field-seeking molecules with $\mu_{\text{eff}} < 0$, the focusing force becomes larger than the defocusing force. In particular, for high switching frequencies, i. e., when the molecules see the effective time-averaged potential, the net potential is always focusing. For high-field-seeking molecules with positive μ_{eff} , however, the time-averaged potential becomes defocusing in the limit of high switching frequencies. The resulting difference in the transmission of the selector as a function of the switching frequency will be discussed in detail in Section 7.3.

In this section, design criteria for optimal lenses for AG focusing were

outlined. In practice, these considerations only represented the starting point for optimizing the electrode geometries. Since a device was to be built that separates species with different m/μ -ratios, numerical simulations of the transmission of two species with different m/μ -ratios (here cis- and trans-3-aminophenol) through different electrode geometries were performed to decide on the final electrode design. For these simulations the real Stark curves (see Chapter 2), numerically calculated electric fields (see Section 3.6.1), and Monte Carlo simulations of a molecular beam (see Section 3.6.3) were used, because the harmonic approximation does not represent a realistic description of the experiment. Nevertheless, this approximation is still very useful to illustrate the basic operation principles of a dynamic focuser and to illustrate how the selectivity of the focuser can be optimized, as will be shown in the following Sections.

3.4 Solving the equations of motion

In this Section, mathematical methods will be introduced to describe the performance of the m/μ -selector for polar molecules. The discussion will be limited to the ideal case of a harmonic interaction potential. As shown in Section 3.3, this approximation is only valid for a small area around the molecular beam axis and does not accurately describe the experimental situation. It is, nevertheless, instructive to derive stability criteria from the harmonic approximation and to compare the device with its analogue for charged particles: the quadrupole mass filter for ions [48].

3.4.1 Equations of motion in the harmonic approximation

As shown in Section 3.3, close to the origin the electric field of the m/μ -selector can be written as $E(x, y) = E_0 + \eta(y^2 - x^2)$. In this harmonic approximation, the interaction potential for a molecule with a constant μ_{eff} is given by:

$$W_{\text{Stark}} = -\mu_{\text{eff}}(E_0 + \eta(y^2 - x^2)) \quad (3.11)$$

For high-field-seeking molecules and $\eta > 0$ this field represents a focusing lens in x -direction and a defocusing lens in y -direction. The equations of motion within this single lens can be written as

$$\begin{aligned} m\ddot{x} &= -\frac{\partial W_{\text{Stark}}}{\partial x} = -2\mu_{\text{eff}}\eta x \\ m\ddot{y} &= -\frac{\partial W_{\text{Stark}}}{\partial y} = 2\mu_{\text{eff}}\eta y \end{aligned} \quad (3.12)$$

where m denotes the mass of the molecule. From Equation 3.10 it is seen that η is related to the multipole expansion parameters by $\eta = (E_0 a_3)/(a_1 r_0^2)$.

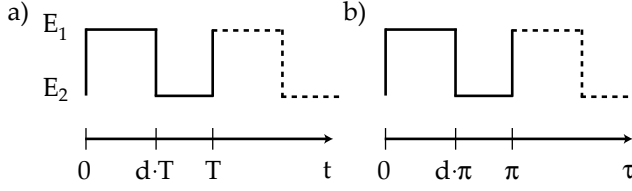


Figure 3.4: a) The electric field of the m/μ -selector is switched in a periodic square wave pattern with duty cycle d and period T between two configurations E_1 and E_2 . b) In the dimensionless time τ the switching sequence is π -periodic. See text for details.

In order to dynamically focus the molecule, the field is switched in a square wave pattern between two field configurations thereby interchanging focusing and defocusing directions. In the most general case, these two fields are characterized by different parameters η_1 and $-\eta_2$ and are applied for different time intervals dT and $(1-d)T$. Here, T denotes the period of the switching cycle with angular frequency ω and the parameter d , which is in the range $0 \leq d \leq 1$, is called the duty cycle of the switching sequence. The switching sequence is illustrated in Figure 3.4 a. The resulting time-dependent harmonic equations of motion can be written as

$$\begin{aligned} \ddot{x} + \frac{2\mu_{\text{eff}} \eta(t)}{m} x &= 0 \\ \ddot{y} - \frac{2\mu_{\text{eff}} \eta(t)}{m} y &= 0 \end{aligned}, \quad \text{where } \eta(t) = \begin{cases} \eta_1 & \text{for } 0 < t \leq dT \\ -\eta_2 & \text{for } dT < t < T \end{cases} \quad (3.13)$$

For the following discussion it is helpful to introduce the dimensionless time $\tau = \omega t/2$ and the corresponding second derivative with respect to time

$$\frac{d^2}{dt^2} = \frac{\omega^2}{4} \frac{d^2}{d\tau^2}. \quad (3.14)$$

Now Equation 3.13 can be expressed in terms of τ

$$\begin{aligned} \frac{d^2 x}{d\tau^2} + \frac{8\mu_{\text{eff}} \eta(\tau)}{m\omega^2} x &= 0 \\ \frac{d^2 y}{d\tau^2} - \frac{8\mu_{\text{eff}} \eta(\tau)}{m\omega^2} y &= 0 \end{aligned}, \quad \text{with } \eta(\tau) = \begin{cases} \eta_1 & \text{for } 0 < \tau \leq d\pi \\ -\eta_2 & \text{for } d\pi < \tau < \pi \end{cases} \quad (3.15)$$

and the equations of motion take the form of Hill's differential equation:

$$\frac{d^2 u}{d\tau^2} + f_u(\tau)u(\tau) = 0, \quad u = x, y \quad (3.16)$$

where $f_u(\tau) = f_u(\tau + \pi)$ is a π -periodic function in the dimensionless time τ . These equations are identical to the equations of motion of ions in a quadrupole mass filter with rectangular excitation [119, 120]. Therefore, methods that have been used to describe the motion of charged particles in the field of a quadrupole mass filter can also be applied to describe the motion of polar molecules in the m/μ -selector. Section 3.4.2 introduces a general matrix method to calculate solutions of Hill's differential equation, while Section 3.4.3 deals with the special case of a piecewise constant waveform, for which the equations of motion can be solved analytically. Both sections summarize the methods presented in references 121 and 122 in the context of charged particle physics.

3.4.2 Matrix method to calculate solutions of Hill's differential equation

If $u_A(\tau)$ and $u_B(\tau)$ are two linearly independent solutions of Equation 3.16 that are defined by the initial conditions

$$\begin{aligned} u_A(0) &= 1 & u_B(0) &= 0 \\ u'_A(0) &= 0 & u'_B(0) &= 1 \end{aligned} \quad (3.17)$$

then the general solution $u(\tau)$ of Equation 3.16 can be written as a linear superposition of these two solutions:

$$u(\tau) = u_0 u_A(\tau) + v_{0,\mu} u_B(\tau), \quad (3.18)$$

where the initial conditions are given by $u(0) = u_0, u'(0) = v_{0,\mu}$. At the end of the first switching period, i. e., for $\tau = \pi$, the initial phase-space position for the next switching period is reached:

$$u(\pi) = u_0 u_A(\pi) + v_{0,\mu} u_B(\pi) =: u_1 \quad (3.19)$$

$$u'(\pi) = u_0 u'_A(\pi) + v_{0,\mu} u'_B(\pi) =: v_{1,\mu} \quad (3.20)$$

Because $u_A(\tau)$ and $u_B(\tau)$ are π -periodic functions, at time τ in the second period, i. e., for $\pi < \tau < 2\pi$, the same solutions u_A and u_B are valid, and the following equations are obtained:

$$u(\tau) = u_1 u_A(\theta) + v_{1,\mu} u_B(\theta) \quad (3.21)$$

$$u'(\tau) = u_1 u'_A(\theta) + v_{1,\mu} u'_B(\theta), \quad (3.22)$$

with $\theta = \tau - \pi$. This procedure can be iteratively repeated and finally in the $(n + 1)$ th period, for $n\pi < \tau < (n + 1)\pi$ and $\theta = \tau - n\pi$, we obtain:

$$u(\tau) = u_n u_A(\theta) + v_{n,\mu} u_B(\theta) \quad (3.23)$$

$$u'(\tau) = u_n u'_A(\theta) + v_{n,\mu} u'_B(\theta) \quad (3.24)$$

This representation of the solution $u(\tau)$ is called a *state vector* representation and can be written in matrix form:

$$\begin{pmatrix} u_{n+1} \\ v_{n+1,u} \end{pmatrix} = M_u \begin{pmatrix} u_n \\ v_{n,u} \end{pmatrix} = M_u^{n+1} \begin{pmatrix} u_0 \\ v_{0,u} \end{pmatrix} \quad (3.25)$$

with

$$M_u = \begin{bmatrix} u_A(\pi) & u_B(\pi) \\ u'_A(\pi) & u'_B(\pi) \end{bmatrix} = \begin{bmatrix} m_{11} & m_{12} \\ m_{21} & m_{22} \end{bmatrix} \quad (3.26)$$

M_u is called the transfer matrix and can be used to calculate a particle's phase-space position at any time τ from the initial phase-space position at time $\tau = 0$. The trace of M_u determines the stability of the solution. Whereas the amplitude of the particle motion increases exponentially for $|\text{Tr}(M_u)| \geq 2$, stable trajectories exist for

$$-2 < \text{Tr}(M_u) < 2 \quad (3.27)$$

as discussed in reference 122. Using the transfer matrix formalism, the problem of solving the equations of motion is reduced to determining the pair of linearly independent solutions u_A and u_B during one period $0 < \tau < \pi$ and the subsequent iterative calculation of the state vectors.

3.4.3 Analytic solution for a piecewise constant wave form

Equation 3.16 can be solved analytically, if the period $[0, T]$ of the waveform applied to the electrodes can be divided in n sub-intervals at points τ_k , $k = 1, \dots, n-1$, where the voltage is kept constant. In the k th interval, where $f_u(\tau) = f_{k,u} = \text{const}$, two cases can be distinguished depending on the sign of $f_{k,u}$. In a focusing lens $f_{k,u}$ is positive and the function $u(\tau)$ that solves Equation 3.16 is

$$u(\tau) = u_k \cos((\tau - \tau_k) \sqrt{f_{k,u}}) + \frac{v_{k,u}}{\sqrt{f_{k,u}}} \sin((\tau - \tau_k) \sqrt{f_{k,u}}). \quad (3.28)$$

Here u_k denotes the position and $v_{k,u}$ denotes the velocity at the beginning of the k th interval. The transfer matrix for the k th interval is obtained by calculating $u(\tau_{k+1})$ and $u'(\tau_{k+1})$. It is given by

$$T(f_{k,u}, \Delta_k) = \begin{bmatrix} \cos(\Delta_k \sqrt{f_{k,u}}) & \frac{1}{\sqrt{f_{k,u}}} \sin(\Delta_k \sqrt{f_{k,u}}) \\ -\sqrt{f_{k,u}} \sin(\Delta_k \sqrt{f_{k,u}}) & \cos(\Delta_k \sqrt{f_{k,u}}) \end{bmatrix} \quad (3.29)$$

where Δ_k is the duration of the k th interval and given by $\Delta_k = \tau_{k+1} - \tau_k$. In a defocusing lens, where $f_{k,u}$ is negative, $u(\tau)$ reads as

$$u(\tau) = u_k \cosh((\tau - \tau_k) \sqrt{-f_{k,u}}) + \frac{v_{k,u}}{\sqrt{-f_{k,u}}} \sinh((\tau - \tau_k) \sqrt{-f_{k,u}}). \quad (3.30)$$

The transfer matrix for an interval representing a defocusing lens can thus be written as

$$T(f_{k,u}, \Delta_k) = \begin{bmatrix} \cosh(\Delta_k \sqrt{-f_{k,u}}) & \frac{1}{\sqrt{-f_{k,u}}} \sinh(\Delta_k \sqrt{-f_{k,u}}) \\ \sqrt{-f_{k,u}} \sinh(\Delta_k \sqrt{-f_{k,u}}) & \cosh(\Delta_k \sqrt{-f_{k,u}}) \end{bmatrix} \quad (3.31)$$

Finally the transfer matrix M_u for a full period of the switching cycle is obtained by multiplication of the transfer matrices for the n subintervals:

$$M_u = T(f_{n,u}, \Delta_n) \times T(f_{n-1,u}, \Delta_{n-1}) \times \dots \times T(f_{1,u}, \Delta_1) \quad (3.32)$$

This method cannot only be applied to square waves, but also to arbitrary periodic waveforms by subdividing these smooth waveforms into sufficiently small intervals of constant voltage [122].

3.5 Stability, selectivity, and the role of the duty cycle

The operation principle of the m/μ -selector for neutral molecules is analogous to the operation principle of a quadrupole mass filter for ions. The latter was first described by Paul and Steinwedel in 1953 [48]. They realized that species with distinct charge-to-mass ratios could be separated when passing an array of electrodes that create an oscillating quadrupole field. Typically, in mass spectrometry a potential Φ_0 having a DC amplitude U and a sinusoidally oscillating RF part with amplitude V is used:[‡]

$$\Phi_0 = U + V \cos \omega t \quad (3.33)$$

The equations of motion of ions in this potential take the form of the Mathieu equation, which is a special case of Hill's differential equation:

$$\frac{d^2 u}{d\tau^2} + (a + 2q \cos 2\tau)u = 0 \quad (3.34)$$

In this equation, two parameters a and q appear that are related to the DC and RF amplitudes, respectively. While a describes the average force constant over one RF period, q corresponds to the change of the force constant during one period. It turns out that the stability of the solutions of the equation of motion solely depends on the values of a and q . Therefore, a - q -maps can be drawn to visualize stable operation conditions and to illustrate the operation principle of the device [47, 48]. Such stability diagrams have also been introduced to describe the trapping of ammonia in an AC trap for neutral molecules [123]

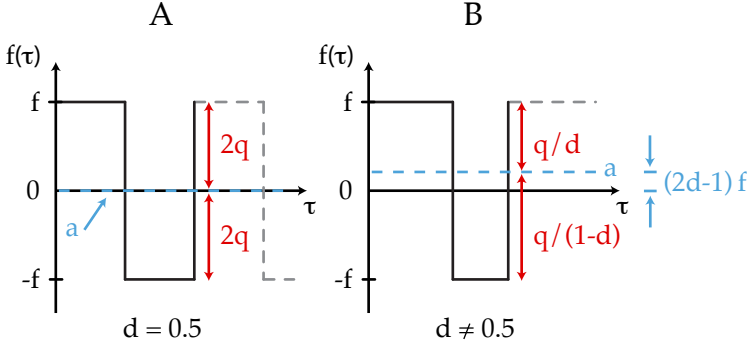


Figure 3.5: Illustration of parameters a and q that are used to describe the stability of the solutions of the equations of motion. A) duty cycle 0.5 B) duty cycle different from 0.5.

and shall be discussed here in the context of the m/μ -selector. In the case of the m/μ -selector, the waveform $f_u(\tau)$ that is applied to the electrodes is not sinusoidal but a square wave. It consists of two subintervals of duration $\Delta_1 = \pi d$ and $\Delta_2 = \pi(1-d)$, during which the function $f_u(\tau)$ takes the values $f_{1,u}$ and $f_{2,u}$, respectively. Introducing

$$f_1 = \frac{8\mu_{\text{eff}} \eta_1}{m\omega^2} \quad \text{and} \quad f_2 = -\frac{8\mu_{\text{eff}} \eta_2}{m\omega^2} \quad (3.35)$$

and recalling Equation 3.15, it is seen that $f_{1,x} = -f_{1,y} =: f_1$ and $f_{2,x} = -f_{2,y} =: f_2$. Analogous to the definition of the stability parameters a and q in the case of the quadrupole mass filter, these parameters can also be introduced for the m/μ -selector:

$$\begin{aligned} a_u &= d f_{1,u} + (1-d) f_{2,u} \\ q_u &= (f_{1,u} - f_{2,u}) d (1-d) \end{aligned} \quad (3.36)$$

For technical reasons, the selector is switched between two configurations of equal electric field strength (i. e., with $|\eta_1| = |\eta_2|$, see Equation 3.15). Therefore, also f_1 and f_2 are of the same magnitude f and only differ by their sign. Hence, Equation 3.36 can be simplified:

$$\begin{aligned} a &:= a_x = -a_y = (2d-1) f \\ q &:= q_x = -q_y = 2 f d (1-d) \end{aligned} \quad (3.37)$$

†The waveform does not necessarily have to be sinusoidal. Also other voltage forms can be used as, for instance, square waves [120].

Figure 3.5 illustrates the waveform applied to the selector and the meaning of a and q .[§] For a duty cycle of 0.5, the average a is always zero and the amplitude of the waveform is given by $2q$. If the duty cycle is different from 0.5, a differs from zero and q characterizes the change of f upon switching relative to the average value a . Stable trajectories are obtained, if both transfer matrices, M_x and M_y , fulfill the stability criteria given in Equation 3.27. These two matrices can be written as

$$\begin{aligned} M_x &= T(-f, \Delta_2) \times T(f, \Delta_1) \\ M_y &= T(f, \Delta_2) \times T(-f, \Delta_1) \end{aligned} \quad (3.38)$$

and be expressed in terms of a , q , and d :

$$\begin{aligned} M_x &= T\left(a - \frac{q}{1-d}, \Delta_2\right) \times T\left(a + \frac{q}{d}, \Delta_1\right) \\ M_y &= T\left(-a + \frac{q}{1-d}, \Delta_2\right) \times T\left(-a - \frac{q}{d}, \Delta_1\right) \end{aligned} \quad (3.39)$$

By evaluating the trace of the matrix, stability diagrams are obtained. Figure 3.6 shows such stability diagrams for duty cycles $d = 0.50$ and $d = 0.40$. Dark grey areas indicate parameters, where the motion along x is stable, whereas light gray areas indicate stable areas for the y coordinate. Only in the black areas, where both stability conditions are fulfilled, stable trajectories are obtained. The regions of stable parameters along both axes are symmetric with respect to a reflection about the a -axis for $d = 0.50$. For all duty cycles the stable regions are point symmetric about the origin. At constant ω , d and η , a given μ_{eff}/m -ratio corresponds to a specific operating point (q, a) in the stability diagram. The ratio a/q is constant, independent from μ_{eff}/m and depends only on the duty cycle. Therefore, all operating points in the stability diagram lie along a straight line through the origin with slope s ,

$$s = \frac{2d - 1}{2d(1 - d)} \quad (3.40)$$

and the actual range of μ_{eff}/m -ratios that are transmitted can be scanned by changing the AC frequency.

Figure 3.7 shows stability diagrams for different duty cycles together with the operation lines on an enlarged scale. For $d = 0.50$ (Figure 3.7 A and B) stable trajectories are obtained for $q < 0.715$ and $4.47 < q < 4.54$. Thus, all species with a μ_{eff}/m -ratio in the ranges

$$0 < \frac{\mu_{\text{eff}}}{m} < \frac{0.715\omega^2}{4\eta} \quad \text{and} \quad \frac{4.47\omega^2}{4\eta} < \frac{\mu_{\text{eff}}}{m} < \frac{4.54\omega^2}{4\eta} \quad (3.41)$$

[§]Note that in the current operation mode a and q cannot be varied independently for a given duty cycle. Nevertheless, these two parameters will be used to determine stable operation conditions in analogy to the usual treatment for a quadrupole mass filter.

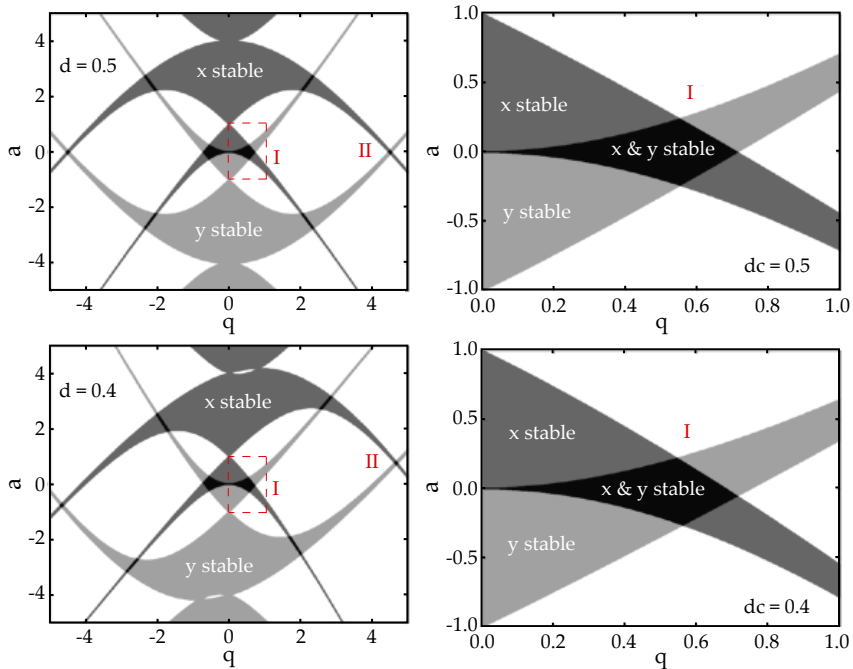


Figure 3.6: Stability diagrams for $d=0.5$ (top) and $d=0.4$ (bottom). Right panel: Zoom into the area indicated by the red box on the right hand side.

are transmitted. The μ_{eff}/m -resolution of the selector can be increased by operating the device at a duty cycle that differs from 0.50. Now the operation line is tilted away from the q -axis and cuts through the tip of the stable region as shown for $d = 0.45$ in Figure 3.7 C. Therefore, only species within a narrow range of μ_{eff}/m -ratios are transmitted. If d is decreased further, then the resolution is enhanced further (see Figure 3.7 D for $d = 0.40$).

The stability diagrams for duty cycles larger than 0.50 are obtained by reflecting the stability diagrams (and the operation lines) for $d < 0.50$ and the same $\Delta d = |d - 0.5|$ about the q -axis. Note that the second, narrow region around $q = 4.5$ that is stable for $d = 0.50$ (Figure 3.7 B), is not sampled when tuning the duty cycle away from 0.50. For $d < 0.50$ this region shifts upwards into the upper half plane of the a - q -diagram, whereas the operation line has a negative slope and only values in the lower half plane are sampled (*vide supra*). For $d > 0.50$ the situation is analogous, i. e. , the second stable region is shifted downwards and the operating line only covers the upper half plane of the a - q -map.

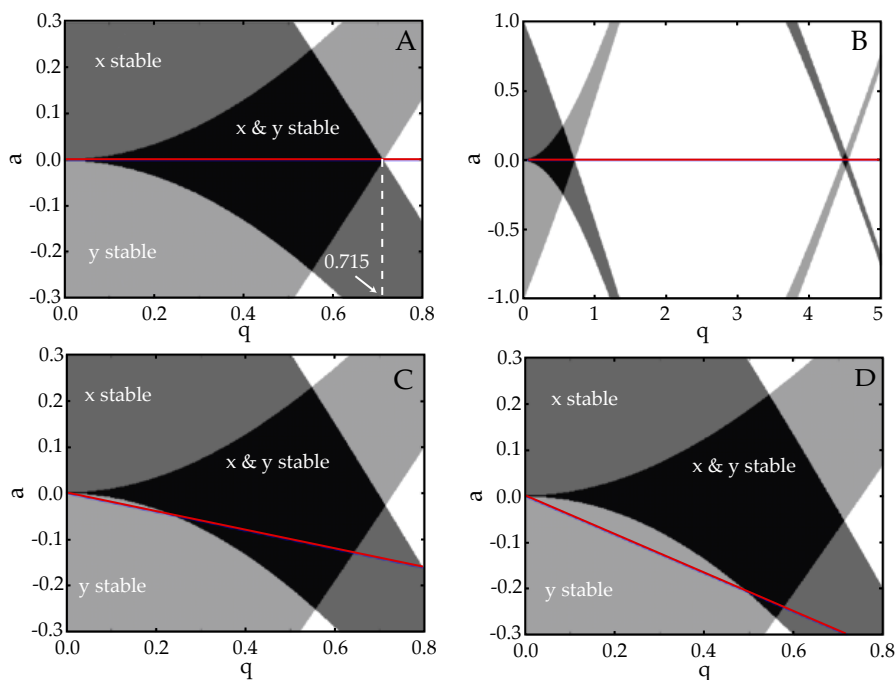


Figure 3.7: Stability diagrams for different duty cycles together with the operation line (red line). A and B: $d = 0.50$, C: $d = 0.45$, D: $d = 0.40$.

In summary, changing the duty cycle of the m/μ -selector increases the resolution in the same way as for the ion guide. It has the same effect as adding a DC offset to the RF potential in the commonly used quadrupole mass filter for ions with sinusoidal waveforms. In order to compare the conclusion drawn from the stability diagrams to real experiments, two things have to be remembered in addition to the harmonic interaction potential being only a crude approximation to the real fields. First of all, the stable areas in the a - q -maps indicate operation conditions, where the amplitude of the particle's motion remains finite, but this amplitude may be too large for the molecule to pass through the device. A molecule is lost once the amplitude of its motion becomes larger than the mechanical aperture of the selector, which is on the order of r_0 (see Figure 3.2). Secondly, particles whose trajectories are unstable in an infinitely long selector might in practice still reach the detection area on metastable trajectories, if the increase of their amplitude is slow compared to the time-of-flight through the selector. For quadrupole mass filters, it has been shown that 25 cycles are not enough to remove all unstable ions from the beam [124]. In the present work, typical switching frequencies are 2-8 kHz, the

molecules spend 1-2 ms in the selector and, therefore, they typically experience 10 switching cycles (see Chapter 7). Thus, it is expected that indeed particles on metastable trajectories are present in the detection region. In order to realistically simulate the experiments, numerical simulations, as described in the following section, are performed.

3.6 Numerical simulations

In this Section, the numerical simulations that are employed to interpret the experimental data are described in detail. Section 3.6.1 describes the numerical calculation of the electric field of both the selector (Chapter 7) and the deflector (Chapter 5). In Section 3.6.2 Monte Carlo simulations of a molecular packet that consists of molecules in a single quantum state are outlined. Finally, in Section 3.6.3, it is discussed how an ensemble of molecules distributed over many quantum states can be simulated.

3.6.1 Electric field

In order to describe the experimental conditions most realistically, the electric fields for the devices implemented in this work are calculated numerically using finite-element methods in the program package Comsol Multiphysics. The 2D electrostatics module of the software is used for the calculation of the electric field inside the selector. The four electrodes shown in Figure 3.2 A are placed in the center of a grounded cylinder with an outer diameter of 60 mm. A fine mesh ensuring smooth gradients of the electric field is chosen for the central area around the molecular beam axis. In the region outside the high-voltage electrodes, the mesh is relatively coarse to reduce computing time. The calculated magnitude of the electric fields in the central region, as well as the calculated gradients along both transverse coordinates, are exported on a 2.5×2.5 mm grid with a spatial resolution of $100 \mu\text{m}$ and stored in a compressed text file for usage in the libcoldmol program package [115]. The electric field of the deflector and its gradients are obtained in the same way.

3.6.2 Simulations for individual quantum states

Simulations of packets of molecules in our setup are performed with the home-built software package libcoldmol [115]. Trajectories for individual molecules in a given rotational quantum state are obtained from numerical integration of the 3D equations of motion using a Runge-Kutta algorithm. The initial phase-space distribution of the molecular packet in the transverse spatial coordinates, x and y , is described by the mean values and widths of circular uniform distributions. For the velocity coordinates, Gaussian distributions characterized by their mean values and full widths at half maximum are used.

Also the initial time spread of the molecular beam, which corresponds to the opening time of the valve, is described by a Gaussian distribution centered around t_0 . From the initial phase-space distribution, the position of a molecule in phase space is randomly chosen. Then, it is propagated through the beamline, which includes all mechanical apertures of the experimental setup. From the electric field applied in the experiment, which is calculated in two dimensions using finite-element methods (see Section 3.6.1), and the Stark energy (see Chapter 2), the acceleration field $\vec{a}(x, y)$ acting on the molecule in the transverse directions is obtained:

$$\vec{a}(x, y) = \frac{\mu_{\text{eff}}(E)}{m} \vec{\nabla} E(x, y) \quad (3.42)$$

The electric field is taken to be constant along z and fringe fields at the entrance and the exit of the selector are neglected. After leaving the electric field, the molecules are propagated through field-free space to the detection region. For each quantum state, typically 10^5 trajectories are calculated to obtain single-quantum-state intensities I_s .

3.6.3 Simulation of a molecular beam

The intensity $I(T_{\text{rot}})$ of an ensemble of molecules at a given rotational temperature T_{rot} in the detection region is calculated from the single-quantum-state intensities as follows:

$$I(T_{\text{rot}}) = \frac{1}{w} \sum_{s=1}^N w_s(T_{\text{rot}}) I_s \quad (3.43)$$

Here, N is the number of quantum states included in the simulations, where the summation only includes $M \geq 0^{\text{II}}$, and $w_s(T_{\text{rot}})$ is the population weight for a given quantum state:

$$w_s(T_{\text{rot}}) = g_M g_{\text{ns}} e^{-\frac{W_0 - W_s}{kT_{\text{rot}}}} \quad (3.44)$$

with W_0 being the field-free potential energy of the ground state and W_s the field-free energy of the current state; $g_M = 1$ for $M = 0$ and $g_M = 2$ otherwise; g_{ns} accounts for the nuclear spin statistical weight of the current state (see Section 2.3). The normalization is given by $w = \sum_{s=1}^N w_s$. In some cases, a molecular beam cannot be accurately described by a single rotational temperature [125]. Therefore, a two-temperature model is implemented in our simulations. In the two-temperature model, the low-temperature part of the molecular beam is calculated as described above. In order to realistically simulate the high-temperature component in the molecular beam, a very large number of quantum states would have to be included in the simulations for large asymmetric top molecules. Because these Monte Carlo simulations are very time consuming, the high-temperature component is approximated by

^{II} $|J_{K_a K_c} M\rangle$ - states for $M > 0$ are treated as one doubly degenerate state.

adding a small fraction of molecules, whose trajectories are obtained when all electrodes are grounded. These unmanipulated molecules approximate the high-temperature component well, because typical rotational temperatures for the high-temperature component in a molecular beam are on the order of 10 K and, for these temperatures, most of the molecules reside in high rotational quantum states that have a small Stark shift and remain almost unaffected by an electric field. Thus, the intensity of the ensemble $I_{2T}(T_{\text{rot}}, q)$ in the two-temperature model is calculated as

$$I_{2T}(T_{\text{rot}}, q) = q \cdot I(T_{\text{rot}}) + (1 - q) \cdot I_{\text{free}} \quad (3.45)$$

where $0 < q < 1$ and I_{free} denotes the intensity of the unmanipulated molecular beam.

If the detection process in the experiment is quantum-state selective (as, for instance, in the measurements presented in Section 7.4, where a two-color REMPI scheme is used for detection), also a state-selective detection efficiency is included in the simulations. This detection efficiency is implemented by multiplying the statistical weights for individual quantum states given in Equation 3.44 by a factor α_s that accounts for the state-specific detection efficiency. Here, α_s is calculated from a simulated spectrum using PGOPHER [126] and the known bandwidth of the detection laser, where a rectangular spectral profile of the laser is assumed.

Chapter 4

Fourier-transform microwave spectroscopy to determine molecular constants of 3-aminophenol*

4.1 Introduction

Since the observation of multiple conformers of tryptophan in a supersonic jet at low temperatures 20 years ago [80], such occurrence of multiple conformers (torsional isomers, rotamers) is quite common for the so called “building blocks of life under isolated conditions” [127, 128] and other modular molecules, even at the low temperatures in a cold supersonic jet. Vast progress was made on the electronic and vibrational spectroscopy of these species. Often the comparison of experimental and *ab initio* vibrational frequencies can be used to distinguish between the isomers [127, 128]. However, in many cases the structural differences are subtle, resulting in very similar vibrational spectra. Thus more sophisticated methods are required. Dong and Miller, for example, assigned individual isomers of cytosine exploiting the angles between vibrational transition moments and the permanent dipole moments of oriented cytosine [85].

Rotational spectroscopy provides precise moments of inertia (rotational constants), quadrupole coupling constants, and dipole moments, which allow for a detailed understanding of the structural and electronic properties of

*Based on: Precise dipole moments and quadrupole coupling constants of the cis and trans conformers of 3-aminophenol: Determination of the absolute conformation, F. Filsinger, K. Wohlfart, M. Schnell, J.-U. Grabow and J. Küpper, *Phys. Chem. Chem. Phys.* **10**, 666 (2008)

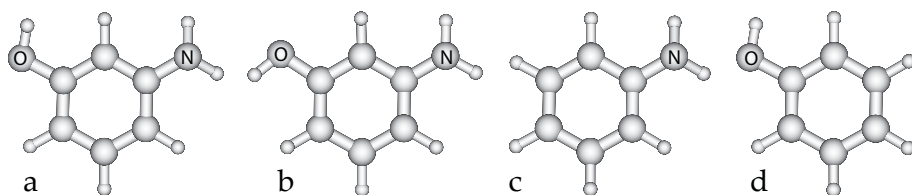


Figure 4.1: Structures of (a) cis- and (b) trans-3-aminophenol, compared to (c) aniline and (d) phenol

individual conformers. In principle, all of these parameters can be compared to results of *ab initio* calculations in order to assign the observed species to calculated structures. However, for structurally similar isomers (*vide supra*), i. e., when only the positions of some hydrogen atoms are different between the isomers, also the rotational constants cannot be used to assign the individual isomer. In such cases, the nuclear quadrupole coupling constants determined from FTMW spectroscopy have been used to discriminate between different calculated minimum structures of amino acids [86]. Similarly, the permanent dipole moments of the isomers can be used to unambiguously assign individual conformers [87].

Here, a detailed study of the individual conformers of 3-aminophenol (3AP) using Fourier-transform microwave spectroscopy (FTMW) is presented. 3AP exists in two distinct conformational configurations, cis-3-aminophenol (c3AP) and trans-3-aminophenol (t3AP), as shown in Figure 4.1. 3AP is a very interesting model system for studying primary molecular properties, because the two conformers are structurally very similar, varying only in the position of one single hydrogen atom, but the electronic properties are quite distinct. The two conformers have very similar rotational constants, but quite different dipole moments and thus Stark effects [87]. The individual conformers can also easily be selectively detected by REMPI-spectroscopy due to their different electronic properties [129, 130]. From a comparison of experimental vibrational frequencies and high-level *ab initio* calculations an assignment of the conformations was possible [129]. Moreover, 3AP is the chromophore of the essential amino acid tyrosine and closely related to dopamine, which also is a benzene derivative with a phenol group (OH) and an amino group (NH₂) substituent. From a detailed understanding of 3AP one can proceed to studies of these more complicated molecules.

The rotational spectra of the parent molecules phenol and aniline, shown in Figure 4.1, were extensively studied using microwave spectroscopy, including the hyperfine structure due to the nitrogen nuclear quadrupole moment for aniline [113] and the full substitution structures [131, 132]. The dipole moments of both species were also determined using Stark effect measurements [131, 132]. For 3-aminophenol, however, to our knowledge no microwave spectroscopy

has been performed. The rotationally resolved electronic excitation spectrum was obtained using high-resolution laser-induced fluorescence spectroscopy and the dipole moment was determined from Stark-effect measurements of these spectra [87], but this study did not provide any details on the hyperfine structure due to the nitrogen nuclear quadrupole moment.

In order to obtain the rotational constants and the dipole moment with high accuracy, the rotational constants, nuclear quadrupole coupling constants, and dipole moment components of c3AP and t3AP are determined using high-resolution FTMW spectroscopy without and with applied electric fields in the coaxially oriented beam-resonator arrangement (COBRA). These measurements are performed for the very lowest rotational states, because these states have the most sensitive Stark effect [103]. In the Stark-effect measurements special attention is given to an accurate calibration of the electric field strengths, which is detailed in Section 4.3.

In addition, high-level *ab initio* calculations are performed to test the quality of theoretical descriptions for these molecules. The comparisons of theoretical and experimental results will allow for the error estimation of theoretical rotational constants and dipole moments of similar molecules that might be studied in the future.

4.2 Experimental setup

The experimental setup of the Hannover COBRA-FTMW-spectrometer is described in detail elsewhere [133, 134]. In brief, 3-aminophenol (Sigma-Aldrich, purity $\geq 98\%$) is heated to 120°C and co-expanded in 2 bar of Ne through a pulsed nozzle (General Valve Series 9) with a 0.8 mm orifice into vacuum. The supersonic expansion is pulsed coaxially into the microwave resonator [133], which was specially developed to provide high sensitivity and resolution at low frequencies down to 2 GHz. The lowest rotational transitions of 3AP in the range of 3–7.5 GHz are recorded with a linewidth (FWHM) of 2.5 kHz and a frequency accuracy of 500 Hz.

Stark-shift measurements are performed with the Coaxially Aligned Electrodes for Stark-effect Applied in Resonators (CAESAR) setup [134]. This setup provides a homogeneous electric field over the entire volume, from which molecules are effectively contributing to the emission signal. The field strength is calibrated using the $J = 1 \leftarrow 0$ transition of OC^{36}S (0.02 % natural abundance) whose dipole moment is precisely known; see Section 4.3 for details. The dipole moment components of 3AP are determined from several hyperfine transitions of the $J = 1 \leftarrow 0$ band measured at different electric field strengths up to 205 V/cm. The individual measurements and the respective fitted Stark lobes are shown in Figure 4.2.

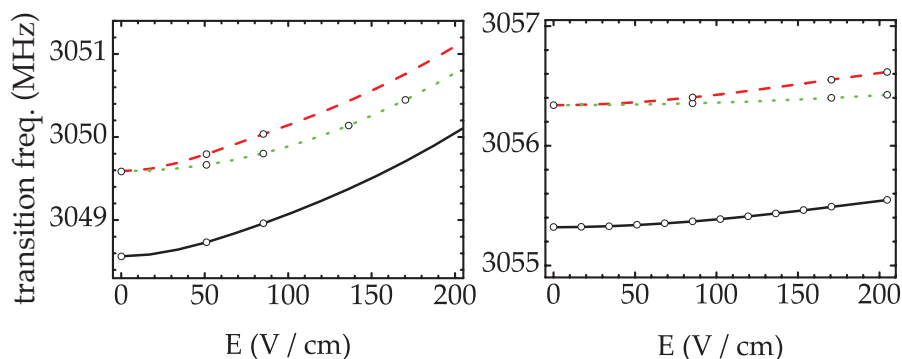


Figure 4.2: Stark-shift measurements (circles) and fitted Stark-lobes (lines) for cis-3-aminophenol (left) and trans-3-aminophenol (right). For both molecules the $J_{K_a, K_c} = 1_{01} \leftarrow 0_{00}, F = 0 \leftarrow 1, m_F = 0 \leftarrow 1$ (solid black lines), $F = 2 \leftarrow 1, m_F = 1 \leftarrow 0$ (dashed red lines), and $F = 2 \leftarrow 1, m_F = 2 \leftarrow 1$ (dotted green lines) transitions were measured.

4.3 Calibration of the Stark measurements

The most critical factor in the determination of electric dipole moments of molecules by Stark effect measurements are accurate values of the applied electric fields. Often sufficiently homogeneous electric fields are generated by applying a voltage difference using two plane-parallel electrodes [103]. For the large volumes sampled in FTMW spectrometers this is difficult and, therefore, in the Hannover COBRA-FTMW experiment a different approach is taken: Within the CAESAR setup, the two concave mirrors of the spectrometer resonator are used as the primary capacitor electrodes and electrode rings between them are used to create a homogeneous field over a very large fraction of the resonator volume [134]. Therefore, all detected molecules experience practically the same field strength, even for the large modes at frequencies below 3 GHz.

In all such experiments the field strength must be calibrated, which is often performed in turn by Stark-effect measurements for isotopologues of OCS, for which the Stark effect is known with high precision [103]. Such measurements yield an averaged effective parallel-plate separation d , which can then be used for the calculation of the electric field strength applied during other measurements performed in the same setup. In the CEASAR setup, however, the cavity mirrors serve as main electrodes. For different measurement frequencies these mirrors need to be moved to fulfill the resonance conditions of the cavity. Since the effective d has a slight dependence on the mirror separation, a linear correction for this effect is applied to all measurements.

First, an effective d from Stark-effect measurements on OC^{36}S is determined,

assuming a dipole moment of 0.71519 (3) D [135], at two very different relative mirror positions, namely $z_1 = 7.12$ mm and $z_2 = 46.13$ mm. These positions are specified relative to the zero-position of the moving cavity mirror and correspond to two quite extreme translational positions of the mirror. For these z -positions the effective plate separations are determined to be $d_1 = 0.58202$ (26) m and $d_2 = 0.59955$ (50) m.

For all Stark-effect measurements on 3AP the actual z -position is noted and the effective d for that measurement is determined by linear interpolation between the two calibration measurements. Including an estimated error in the z -position of 0.01 mm for all measurements and an accuracy of the applied voltages of 10 V this results in a relative uncertainty of the electric field strengths in the individual measurements below 10^{-3} . The resulting contribution to the error for the dipole moments of 3-aminophenol is less than $1.1 \cdot 10^{-3}$, and it is included in the error estimates given in Table 4.4.

4.4 Computational details

Ab initio calculations of c3AP and t3AP are performed using the Gaussian 03 program package [136]. Previously, rotational constants and dipole moments had been calculated using the B3PW91/6-31G* [87] and CASSCF and CASPT2/6-31G* [129] levels of theory. Here, these calculations are extended to multiple methods (B3LYP, B3PW91, MP2) using the same 6-31G* and the larger aug-cc-pVTZ basis sets. Fully relaxed geometry optimizations of both conformers are performed at these levels of theory and the dipole moments are calculated for the obtained minimum structures on the potential energy surface. However, this procedure yields considerable out-of-plane μ_c dipole moment components due to the non-planar structure around the nitrogen nucleus and the corresponding out-of-plane non-bonding sp^3 orbital on the nitrogen atom. These μ_c dipole moment components are, however, not experimentally observable as the zero-point vibrational level averages over all out-of-plane angles due to the inversion tunneling of the two amino hydrogen atoms. The tunneling rate is expected to be similar to the one of aniline (1 THz [113]) and much larger than the rotational frequency. To test the calculated dipole moments, also geometry optimizations for the planar transition states of the inversion motion were performed for both conformers in C_s symmetry. These calculations confirmed the previous reasoning and gave in-plane dipole moment components quite similar to the specified ones. The obtained rotational constants and dipole moments are presented together with the experimental results in Section 4.5. For an improved theoretical description, one would need to calculate the dipole moment function along the inversion motion coordinate and deduce the vibrationally averaged expectation values $\langle \mu_\alpha \rangle$, which is beyond the scope of this work.

$J'_{K'_a K'_c}$	←	$J''_{K''_a K''_c}$	F'	F''	comp.	obs. (MHz)	obs.–calc. (MHz)
1 ₀₁	←	0 ₀₀	0	1	1	3048.5622	-0.0017
			2	1	1	3049.5857	-0.0030
			1	1	1	3050.2767	0.0047
2 ₀₂	←	1 ₀₁	1	1	3	5978.8532	0.0009
			3	2	1	5980.0761	-0.0005
			2	1	1	5980.3687	0.0014
			1	0	3	5980.5581	-0.0023
2 ₁₂	←	1 ₀₁	2	2	2	5981.0511	0.0006
			1	1	2	7412.7858	0.0020
			3	2	3	7414.2197	-0.0024
			2	1	2	7414.8910	0.0021
			2	2	1	7415.5794	-0.0017

Table 4.1: Measured hyperfine-split transitions for cis-3-aminophenol with fit residuals. Also the number of clearly split components is given for each transition. Note that additional splittings, which are not resolved by our spectrometer, might be present. See text for details.

4.5 Results

The measured field-free microwave transitions of c3AP and t3AP are given in Table 4.1 and Table 4.2, respectively. For each conformer, all hyperfine transitions are fit to a rigid-rotor Hamiltonian, including nuclear quadrupole coupling for the nitrogen nucleus, using the computer program qstark [137, 138]. Several lines show additional splittings on the order of 5–10 kHz, as depicted in Figure 4.3 b. The number of clearly visible split components is given in Table 4.1 and Table 4.2. Many lines show additional shoulders which are not included in the tables, as it is not possible to reliably determine their frequency. These splittings are most likely due to magnetic spin-spin or spin-rotation coupling of the hydrogen atoms, which are not included in the used Hamiltonian. The magnetic-interaction energy of two hydrogen nuclei with parallel spins is approximately 6 kHz for a distance of 170 pm,[†] which corresponds to the distance of the two amine hydrogen atoms. The distance between the hydroxy hydrogen to the closest hydrogen atom on the ring is 230 pm yielding a somewhat smaller interaction energy of approximately 2.5 kHz. The spin-rotation interaction of the two amine hydrogen atoms, for example, can be estimated based on the NH₃ coupling constant (18.5 kHz [139]), scaled by the relative angular velocity of ammonia ($B + C \sim 500$ GHz) and 3AP ($B + C \sim 3$ GHz). The approximately 180 times smaller angular velocity of 3AP compared to ammonia suggests couplings, which are also two orders

[†]The interaction energy of two magnetic dipoles is given by $W = \frac{\mu_0 \mu \mu'}{4\pi r^3}$.

$J'_{K'_a K'_c}$	\leftarrow	$J''_{K''_a K''_c}$	F'	F''	comp.	obs. (MHz)	obs.-calc. (MHz)
1 ₀₁	\leftarrow	0 ₀₀	0	1	1	3055.3215	0.0021
			2	1	1	3056.3392	-0.0001
			1	1	2	3057.0218	0.0025
1 ₁₁	\leftarrow	0 ₀₀	0	1	1	4957.3704	0.0011
			2	1	2	4958.2638	0.0006
2 ₀₂	\leftarrow	1 ₀₁	1	1	1	5990.5985	0.0011
			3	2	1	5991.8183	-0.0007
			2	1	2	5992.1126	-0.0014
			1	0	1	5992.2975	0.0003
			2	2	2	5992.7950	0.0010
2 ₁₁	\leftarrow	1 ₁₀	3	2	1	6712.8958	-0.0016
2 ₁₂	\leftarrow	1 ₀₁	1	1	2	7413.1225	0.0001
			1	2	1	7413.8012	-0.0011
			1	0	1	7414.8210	-0.0013
			2	1	3	7415.2475	-0.0016
			2	2	1	7415.9312	0.0022

Table 4.2: Measured hyperfine-split transitions for trans-3-aminophenol with fit residuals. Also the number of clearly split components is given for each transition. Note that additional splittings, which are not resolved by our spectrometer, might be present. See text for details.

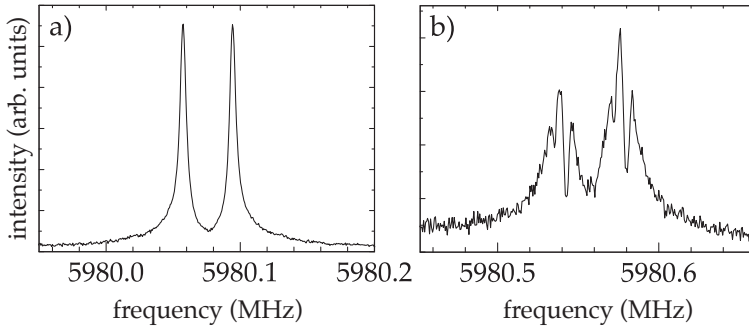


Figure 4.3: Amplitude spectrum of the $J'_{K'_a K'_c} F' \leftarrow J''_{K''_a K''_c} F'' = 2_{02}3 \leftarrow 1_{01}2$ (a) and $2_{02}1 \leftarrow 1_{01}0$ (b) hyperfine transitions for c3AP. The major doublet-splitting in both Figures is due to the Doppler splitting in the coaxial spectrometer-arrangement. Additional splittings of the individual Doppler components of this single quadrupole-component of the rotational transition are obvious in Figure (b). We attribute these splittings to partially resolved magnetic hyperfine structure due to the hydrogen nuclear spins; see text for details.

of magnitude smaller. On the other hand, the wider charge distribution of 3AP increases the induced magnetic field and, therefore, the coupling strength. Altogether, a spin-rotation coupling on the order of 1 kHz is estimated. From the number of resolved components for the different $J' \leftarrow J''$ transitions, given in Table 4.1 and Table 4.2, no systematic dependence on J can be derived. Splittings due to spin-rotation coupling are expected to increase with J , while for spin-spin coupling, one would expect a slight decrease of the splitting with increasing J [103]. Both effects are expected to result in a splitting comparable to the observed one. A detailed evaluation of these splittings would require even higher-resolution measurements, the examination of higher J -transitions, or, most probably, both, in order to sufficiently resolve and analyze the underlying hyperfine structure, as has been done for ammonia [139–141]. For the purpose of this work the line-center frequencies are determined as the intensity-weighted average of these split lines.

The fit to the experimental data is very good with remaining standard deviations of 2.93 kHz and 1.65 kHz for c3AP and t3AP, respectively. This is somewhat higher than usual because the experimental frequencies were obtained from intensity weighting of the underlying unassigned additional hyperfine structure (*vide supra*). The obtained rotational constants and quadrupole coupling constants are given in Table 4.3.

For comparison, also the values determined from the high-resolution electronic excitation spectrum [87] and the *ab initio* calculated rotational constants are shown. The agreement with the previous experimental values is good. The remaining differences might be attributed to the fact that the rotational constants were only determined from transitions between the very lowest rotational states, where centrifugal distortion effects are negligible. The previous electronic excitation spectroscopy experiment determined an average value over many more transitions, including transitions between much higher rotational states, where centrifugal distortion for such molecules is appreciable. Since, in that work, a rigid-rotor Hamiltonian was still used to fit the data, the thus obtained rotational constants are effective rotational constants including these centrifugal distortion effects in an averaged way.

The *ab initio* rotational constants agree reasonably well with the experimental results, but show a considerable spread for the different methods and basis sets. It is obvious that it would not be possible to determine the absolute configuration (cis or trans) of the two conformers from comparisons of experimental and theoretical rotational constants, because the experimental constants are very similar and the potential errors of the calculated rotational constants are too large for such an assignment. The planar moments of inertia[‡] of the vibrational ground state of $P_{cc}^0 = 0.2262 \text{ u}\text{\AA}^2$ for c3AP and $P_{cc}^0 = 0.21484 \text{ u}\text{\AA}^2$ for t3AP

[‡] The planar moments P_{gg} of a molecule calculate as $2 \cdot P_{gg}^v = I_{g'}^v + I_{g''}^v - I_g^v$. With $g = c, g' = a, g'' = b$, and $v = 0$ we get the planar moment P_{cc} with respect to the *ab*-plane of the principal axes of inertia of the oblate rotors in their vibrational ground state: $2 \cdot P_{cc}^0 = I_a^0 + I_b^0 - I_c^0$

method	exp.	exp.	B3PW91	B3LYP	B3LYP	MP2	CASSCF(8,10) ^a
basis set	(this work)	ref. ([87])	6-31G*	6-31G*	aug-cc-pVTZ	aug-cc-pVTZ	6-31G*
cis-3AP							
A (MHz)	3734.930 (14)	3734.4 (7)	3741	3728	3755	3748	3748
B (MHz)	1823.2095 (64)	1823.1 (1)	1825	1817	1829	1825	1830
C (MHz)	1226.493 (11)	1226.6 (1)	1228	1223	1231	1229	1231
χ_{aa} (MHz)	2.2776 (34)						
$\chi_{bb} - \chi_{cc}$ (MHz)	6.179 (14)						
χ_{bb} (MHz)	1.951						
χ_{cc} (MHz)	-4.228						
P_{cc}^0 (uÅ ²)	0.2262 (19)	0.26(2)					
σ (MHz)	0.002931	1.77					
number of lines	12	114					
trans-3AP							
A (MHz)	3730.1676 (14)	3729.5 (4)	3737	3723	3752	3737	3748
B (MHz)	1828.25774 (58)	1828.2 (1)	1829	1821	1833	1832	1833
C (MHz)	1228.1948 (10)	1228.2 (1)	1229	1224	1232	1231	1232
χ_{aa} (MHz)	2.2666 (15)						
$\chi_{bb} - \chi_{cc}$ (MHz)	6.2405 (48)						
χ_{bb} (MHz)	1.987						
χ_{cc} (MHz)	-4.254						
P_{cc}^0 (uÅ ²)	0.21484 (18)	0.23(2)					
σ (MHz)	0.001647	1.61					
number of lines	16	155					

Table 4.3: Rotational constant, ¹⁴N quadrupole coupling constants, planar moments of inertia P_{cc}^0 , overall standard deviations σ of the fit, and the number of lines included in the fit for cis- and trans-3-aminophenol.

^aPrivate communication with Markus Gerhards (2007); the values are determined from the calculations described in reference [129].

are comparable to the one of aniline ($P_{cc}^0 = 0.2557 \text{ u}\text{\AA}^2$ [131]). Phenol has a considerably smaller planar moment of $P_{cc}^0 = 0.01524 \text{ u}\text{\AA}^2$ [132]. These values indicate that the NH_2 configurations of c3AP and t3AP are similar to the one of aniline and no additional OH out-of-plane contributions compared to phenol are present.

The quadrupole coupling constants are also similar for the two conformers and compared to aniline [113], showing a similar chemical environment of the nitrogen nucleus in all three molecules. They would not allow to determine the absolute conformation, as was done for amino acids before [86]. Also the barriers to inversion of the amino group are calculated at the MP2/cc-VTZ level of theory as the energy difference between the minimum energy for a planar optimized geometry (C_s -symmetry) and the absolute minimum on the PES. The barrier heights obtained in that way are 604 cm^{-1} and 567 cm^{-1} for c3AP and t3AP, respectively. For comparison, the barrier for aniline is calculated at the same level of theory, which yields a value of 585 cm^{-1} in fair agreement with the experimental values of 525 cm^{-1} [142, 143] or 540 cm^{-1} [113], considering that the calculations neglect zero-point vibrational effects. Overall it is clear that the chemical environment of the amino group is quite similar for both conformers of 3AP and for aniline.

From the Stark-shift measurements the μ_a and μ_b dipole moment components of the two conformers are precisely determined by fitting the transition shifts with qstark [137, 138] using calibrated field strengths as described in Section 4.3. The experimental dipole moments are given in Table 4.4 together with *ab initio* values. The dipole moments of c3AP and t3AP are also calculated from the dipole moments of aniline [131] and phenol [132] using simple vector addition of the individual dipole moments in the aminophenol principal axis system. These values are in excellent agreement with the experimentally observed values, confirming the dipole additivity for the ground states of 3AP [87, 114]. Using either the dipole moments predicted by the vector model or by *ab initio* calculations, the absolute conformation of the molecules can easily be obtained. The assignment agrees with the previous Stark effect study by Reese et al. [87]. This procedure of distinguishing conformers based on their dipole moment orientation is quite comparable to the use of vibrational transition moment angles [85]. In that work the angle between permanent dipole moment and vibrational transition dipole moments was used to distinguish different conformers. Here the angle between the permanent dipole moment and the principal axes is used for the same purpose. Overall, it is a very helpful tool to employ experimental dipole moments to determine the absolute conformational structure of modular molecules.

The quality of the *ab initio* dipole moments is quite unsatisfactory. The calculated dipole moments for the more polar conformer c3AP are typically within 10 %. For the less polar conformer t3AP the calculated values differ even by considerably more than 10 % from the experimental values for all levels of theory. However, what is most discouraging for the calculation of

method	exp.	exp.	vector	B3PW91	B3PW91	B3LYP	B3LYP	MP2	MP2	CASSCF(8,10) ^{a,d}	CASPT2 ^{a,d}
basis set	(this work)	(ref. [87])	model	6-31G*	aug-cc-pVTZ	6-31G*	aug-cc-pVTZ	6-31G*	aug-cc-pVTZ	6-31G*	6-31G*
cis-3AP											
μ_a (D)	1.7735 (50)	1.77 (6)	1.70	1.85	1.85	1.81	1.86	1.72	1.68	1.68	1.73
μ_b (D)	1.5195 (83)	1.5 (2)	1.55	1.78	1.69	1.72	1.65	1.54	1.48	1.32	1.29
$ \mu $ (D)	2.3354 (92)	2.3 (2)	2.30	2.57	2.51	2.50	2.49	2.31	2.14	2.14	2.16
σ (MHz)	0.001286										
$n_{\text{meas.}}$	10										
trans-3AP											
μ_a (D)	0.5563 (13)	0.57 (1)	0.49	0.44	0.56	0.42	0.57	0.23	0.37	0.16	0.20
μ_b (D)	0.5376 (27)	0.5 (1)	0.56	0.51	0.43	0.54	0.48	0.81	0.63	1.05	1.09
$ \mu $ (D)	0.7736 (28)	0.7 (1)	0.74	0.67	0.71	0.68	0.75	0.84	0.73	1.06	1.11
σ (MHz)	0.000881										
$n_{\text{meas.}}$	19										

Table 4.4: Dipole moment components μ_a and μ_b , overall dipole moments $|\mu|$ of cis- and trans-3-aminophenol, standard deviations σ of the fits, and the number of measurements $n_{\text{meas.}}$ at different field strengths included in the fit. See text for details.

^aPrivate communication with Markus Gerhards (2007); the values are determined from the calculations described in reference [129]. The CASPT2 dipole moments are calculated at the CASSCF-optimized geometry.

dipole moments of large and modular molecules is the wide distribution of their calculated orientations, as can be seen from the individual components along the principal axes. Moreover, increasing the level of theory and using the larger basis set often even gives inferior results. For the CASSCF calculations systematic problems in the descriptions of hydroxybenzenes due to the neglect of σ -correlation have already been described [129]. Density-functional theory (esp. the B3LYP functional) using a large basis set (aug-cc-pVTZ) gives the best overall results for the two conformers of 3AP, but it has to be more carefully examined for a wider class of molecules whether this is serendipitous or a consistent quality of this method. Overall it must be concluded, that the *ab initio* methods used here, which are applied routinely in the calculation of structures and vibrational frequencies of molecules of similar size as 3AP, perform quite poorly for the calculation of electric dipole moments of these molecules. Therefore, one has to be careful when using such *ab initio* results for the calculation of Stark shifts of large molecules, as the dipole moment components directly enter the Hamiltonian matrix calculation (see Section 2.4).

The dipole moments also yield important information on the intermolecular interactions of molecules. However, in a recent study of the 3AP water cluster, only a single dimer structure could be observed, an OH–OH₂ bound hydrogen structure between the t3AP conformer and water. No c3AP-water cluster was found [144]. Considering the much larger dipole moment of c3AP this indicates that the local OH–OH₂ interaction and steric effects, which are favorable for t3AP-water, are dominating over the overall electrostatic interaction. For bulk solutions, on the other hand, the more polar c3AP conformer would be expected to have a stronger interaction with the solvent than the less polar t3AP.

4.6 Summary

Several hyperfine-resolved rotational transitions of the conformers of 3AP for the lowest J -values are measured using FTMW spectroscopy. From a rigid rotor analysis the rotational constants and ¹⁴N nuclear quadrupole coupling constants can be precisely determined. These nuclear quadrupole coupling constants and the calculated barriers to inversion are comparable to the values of aniline, confirming a similar electronic configuration around the nitrogen nucleus. In order to assign the absolute conformation of the individual species, the rotational constants and the quadrupole coupling constants cannot be used, as they are too similar for the two conformers. However, the dipole moments of both conformers are precisely determined using the Stark shifts of several of these lines. These dipole moments can be rationalized in terms of simple vector addition of the dipole moments of aniline and phenol, and they allow to unambiguously assign the absolute conformation, even without the need for *ab initio* calculations.

The precisely known rotational constants and dipole moment components

allow for the calculation of the Stark effect of the individual rotational states with good accuracy even for very high electric fields (i. e. , up to 150 kV/cm), as applied in this work. The Stark shifts of the two conformers are quite different, with ground-state effective dipole moments at 150 kV/cm of $0.0364 \text{ cm}^{-1}/(\text{kV cm}^{-1})$ for c3AP and $0.0113 \text{ cm}^{-1}/(\text{kV cm}^{-1})$ for t3AP. These different dipole moments can be exploited to spatially separate the two conformers using static or switched inhomogeneous electric fields, as described in Chapters 6 and 7.

Chapter 5

Laser-induced alignment and orientation of quantum-state-selected large molecules*

5.1 Introduction

For a large range of experiments in chemistry and physics, a high level of control over the external and internal degrees of freedom of molecules is very beneficial. This includes control over the translational and the rotational motions, as well as the selection of a single quantum state or a small set of states. Such quantum-state-selected targets provide unique possibilities, for example, for manipulating the external degrees of freedom with static electric fields [145, 146] or optical fields [147, 148], or both [149, 150]. The quantum-state selection also naturally discriminates between individual stereo-isomers of large molecules [118]. The resulting samples of aligned or oriented individual isomers offer unique prospects for novel experiments with complex molecules, such as femtosecond pump-probe measurements, X-ray or electron diffraction in the gas phase [151, 152], high-harmonic generation [153], or tomographic reconstructions of molecular orbitals [91]. Moreover, it would provide considerably increased control in reaction-dynamics experiments [24].

*Based on: Laser induced alignment and orientation of quantum-state-selected large molecules, L. Holmegaard, J. H. Nielsen, I. Nevo, H. Stapelfeldt, F. Filsinger, J. Küpper, and G. Meijer, *Phys. Rev. Lett.* **102**, 023001 (2009)

Quantum-state selection, alignment, and orientation of large molecules using static electric and laser fields, F. Filsinger, J. Küpper, G. Meijer, L. Holmegaard, J. H. Nielsen, I. Nevo, J. L. Hansen, and H. Stapelfeldt, *J. Chem. Phys.* **131**, 064309 (2009)

Strong cooling can be achieved in supersonic expansions of molecules seeded in an inert atomic carrier gas. For small molecules (consisting of just a few atoms) only a few rotational states are populated at the typical temperatures on the order of 1 K. For larger polyatomic systems rotational cooling down to or even below 1 K still leaves the molecular ensemble distributed over a considerable number of rotational states, thereby often masking quantum-state-specific effects.

This chapter describes how the deflection of cold molecular beams with static electric fields can be exploited for the quantum-state selection of polar molecules, a technique following a proposal of Otto Stern from the 1920s [9]. After briefly introducing the experimental setup in Section 5.2, details of the electrostatic beam deflection are presented. First, it is demonstrated in Section 5.3 how the rotational temperature of cold supersonic jets can be determined from deflection measurements and that indeed a small subset of quantum states can be addressed in deflected samples of large molecules. In particular, the ground state has the largest Stark shift and molecules residing in this state are deflected the most. The goal is to isolate and use samples of molecules in the few lowest-lying states, or even only in the ground state, as targets for various experiments. Since deflection does not change the initial state distribution but merely disperses it, it is crucial that the population of ground-state molecules in the molecular beam is initially as large as possible. Therefore, the rotational temperature of the molecular beam is made as low as possible using a high-pressure supersonic expansion [154]. In Sections 5.4 and 5.5, it is demonstrated how the resulting state-selected molecules can be used to improve one-dimensional (1D) laser-induced alignment [147, 155] and mixed-field orientation [156–158]. Here, alignment refers to confinement of a molecule-fixed axis (typically, the major polarizability axis) along a laboratory-fixed axis and orientation refers to the molecular dipole moments pointing in a particular direction. Alignment and orientation occur in the adiabatic limit where the laser field, used to align the molecules, is turned on and off slowly compared to the inherent rotational periods of the molecule [159]. The state selection leads to strong enhancement in the degree of orientation and alignment of iodobenzene molecules compared to that achieved when no deflection is used.

5.2 Experimental setup

A schematic of the experimental setup is shown in Figure 5.1. The molecular beam machine consists of three differentially pumped vacuum chambers; the source chamber housing a pulsed valve (pumped by a 2000 l/s turbomolecular pump), the deflector chamber (pumped by a 500 l/s turbomolecular pump) and

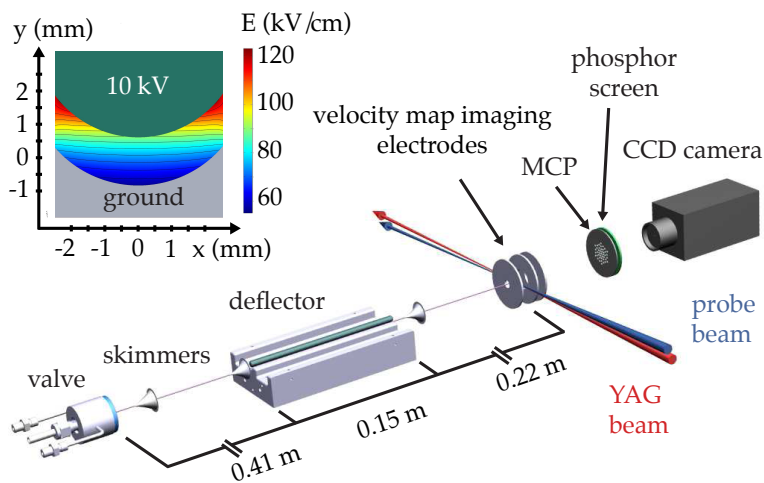


Figure 5.1: Scheme of the experimental setup. In the inset, a cut through the deflector is shown, and a contour plot of the electric field strength is given. Details of the velocity map imaging spectrometer are shown in Figure 5.7. See text for details.

the detection chamber housing the ion/electron spectrometer (pumped by a 500 l/s turbomolecular pump). About 3 mbar of iodobenzene (Sigma Aldrich, 98 % purity) or benzonitrile (Sigma Aldrich, 98 % purity) is seeded in an inert carrier gas and expanded through a pulsed valve into vacuum. In order to obtain optimal cooling of the molecular beam, a miniaturized, high-pressure Even-Lavie valve [154] is used operating at a backing pressure of 90 bar of He or 20 bar of Ne, limited by the onset of cluster formation. While rotational temperatures down to 0.4 K have been achieved under similar conditions [160], the typical rotational temperature in our experiments is ~ 1 K. Two 1 mm-diameter skimmers placed 15 cm (separating the source and the deflector chamber) and 38 cm downstream from the nozzle collimate the molecular beam before it enters a 15 cm-long electrostatic deflector. A cut through the electrodes of the deflector is shown in the inset of Figure 5.1 together with the electric field created. A trough with an inner radius of curvature of 3.2 mm at ground potential and a rod with a radius of 3.0 mm at high voltage create a two-wire field [2]. The vertical gap across the molecular beam axis is 1.4 mm, while the smallest distance between the electrodes is 0.9 mm. The two-wire field geometry is well suited for molecular beam deflection. The gradient of the electric field along the vertical direction is large and nearly constant over a large area explored by the molecular beam, while the electric field is very homogeneous along the horizontal direction. Thus, a polar molecule experiences a nearly constant force in the vertical direction independent of its position within the deflector,

while the force in the horizontal direction (i. e. , broadening of the beam in the horizontal direction) is minimized. In our setup, the deflector is mounted such that molecules in high-field-seeking (low-field-seeking) quantum states are deflected upwards (downwards).

After passing through the deflector, the molecular beam enters the differentially pumped detection chamber via a third skimmer of 1.5 mm diameter. In the detection area, the molecular beam is crossed by one or two laser beams that are focused by a spherical lens with a focal length of $f = 300$ mm. The lens is mounted on a vertical translation stage so that the height of the laser foci can be adjusted with high precision. In the first part of the experiment, where the beam deflection of iodobenzene and benzonitrile is characterized, only one laser, the probe laser, is used. This Ti:Sapphire laser (25 fs (FWHM) pulses, 800 nm, beam-waist $\omega_0 = 21$ μm) is used to determine the relative density in the molecular beam via photoionization. In the second part of the experiment, an additional laser pulse is included to study laser-induced alignment and orientation of iodobenzene. For these experiments, 10 ns (FWHM) long pulses from a Nd:YAG laser (1064 nm, $\omega_0 = 36$ μm) are overlapped in time and space with the probe laser pulses. While the YAG laser induces adiabatic alignment and orientation, here the fs-laser is used to determine the spatial orientation of the target molecules via multiple ionization and subsequent Coulomb explosion. Ionic fragments produced in the Coulomb explosion are accelerated in a velocity focusing geometry towards the detector. The detector can be gated with a time resolution of ~ 90 ns, which allows for mass-selective detection of individual fragments. A microchannel plate (MCP) detector backed by a phosphor screen is employed to detect the position of mass-selected ions. In particular, I^+ fragment ions, formed in the Coulomb explosion of iodobenzene, are particularly useful experimental observables since they recoil along the C-I symmetry axis of the molecule. Thus, 2D ion images of I^+ recorded with a CCD camera provide direct information about the instantaneous molecular orientation of the C-I bond axis with respect to the laboratory frame and are, therefore, the basic observables in these experiments. All experiments are conducted at 20 Hz, limited by the repetition rate of the YAG laser.

5.3 Electrostatic deflection of cold molecular beams

In the first experiment, the deflection of benzonitrile molecules (BN, $\text{C}_7\text{H}_5\text{N}$) seeded in 90 bar of He is investigated. BN is an ideal candidate for electrostatic beam deflection due to its large permanent dipole moment of 4.5 D. From the precisely known molecular constants [161] the energy of a given rotational quantum state can be calculated as a function of the electric field strength. The exact procedure is detailed in Chapter 2. Figure 5.2 shows the Stark energies for

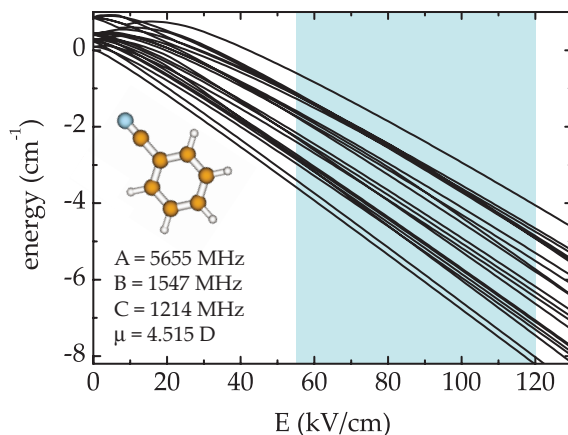


Figure 5.2: Energy as a function of the electric field strength for the lowest rotational quantum states of benzonitrile. The shaded area indicates the actual electric field strength inside the deflector. In the inset, the molecular structure is shown together with the relevant molecular constants [161].

the lowest rotational states of BN. Due to the small rotational constants and the resulting high density of rotational states, a large number of states is populated even under the cold conditions in a supersonic expansion. At a rotational temperature of 1 K, the typical temperature in our experiments (*vide infra*), 66 rotational quantum states (with 419 M -components) have a population larger than 1 % relative to the ground state. At the electric field strengths present in the deflector, indicated by the shaded area in Figure 5.2, all low-lying quantum states are high-field seeking. This is due to mixing of closely spaced states of the same symmetry and is typical for large asymmetric top molecules. The Stark shift and thus the force a molecule experiences in an inhomogeneous electric field depends on the rotational quantum state. Molecules in the ground state have the largest Stark shift and are, therefore, deflected the most. In general, the Stark shift decreases with increasing J quantum number. Thus, the lower the rotational temperature of the molecular beam is, the more the beam is deflected.

Figure 5.3 shows vertical intensity profiles of BN for various high voltages applied to the deflector. Vertical intensity profiles are obtained by recording the BN^+ signal from photoionization by the fs-laser as a function of the vertical position of the laser focus. If no high voltage is applied to the deflector, the molecular beam extends over ~ 2 mm. In this case, the size of the molecular beam in the detection region is determined by the mechanical aperture of the experimental setup, i. e. , by the dimensions of the deflector and the last skimmer

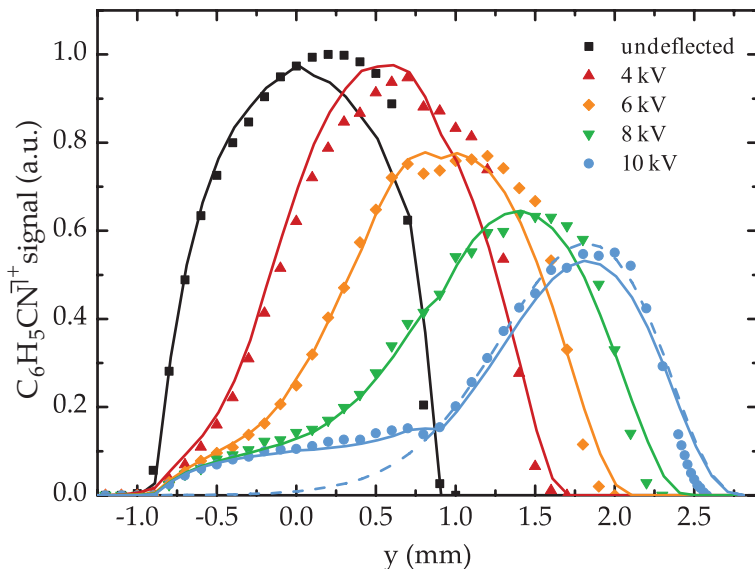


Figure 5.3: The vertical spatial profile of the molecular beam for different deflection voltages applied, measured by recording the laser-induced BN^+ signal (see text). The experimental data are shown as symbols together with the corresponding simulated profiles (lines).

before the detection region. As the high voltage is turned on, the molecular beam profile broadens and shifts upwards. At a voltage of 10 kV, a large fraction of the molecules is deflected out of the original, undeflected beam profile. A small fraction of the molecules, however, is almost unaffected by the deflector.

In order to understand these experimental findings, Monte Carlo simulations are employed, which are described in detail in Section 3.6. In brief, trajectory calculations are performed for molecular packets of individual rotational quantum states. These calculations yield single-quantum-state deflection profiles. Then, the single-state profiles are averaged according to the populations of the respective states in the original molecular beam (i. e., at the entrance of the deflector). From these simulations it is obvious that the molecules in the original beam are not rotationally thermalized, an effect that has previously been observed in rotationally resolved spectroscopy [125, 162]. A number of different descriptions of the populations of rotational states have been given [162]. Here, the formula for a two-temperature model originally proposed by Levy and coworkers [125] is used. For details and the approximation of the high-temperature component see Section 3.6.3. Finally, the rotational temperature of the low-temperature component in the molecular beam is obtained by fitting the simulated deflection

profiles to the experimental data using a local optimization algorithm. All deflection profiles measured at the different voltages are fitted simultaneously, where the fraction q of the low-temperature component, a general intensity scaling factor s of the deflected profiles (with respect to the undeflected beam profile), and the rotational temperature T_{rot} of the low-temperature component are the fitting parameters. Best agreement between experimental data and simulations is found for $q = 0.93$ and $T_{\text{rot}} = 0.8$ K. The resulting simulated deflection profiles nicely reproduce the experimental data as shown in Figure 5.3 (solid lines). In particular, the undeflected part of the molecular beam for 10 kV can be perfectly simulated, which indicates that the use of a two-temperature model was indeed justified. For comparison, also a simulated deflection profile for 10 kV using a one-temperature model is shown (dashed line in Figure 5.3).

In order to estimate the uncertainty of T_{rot} , deflection profiles are calculated for different rotational temperatures. For each fixed rotational temperature, the best values for s and q are determined using the fitting procedure outlined above and the resulting deflection profile for a voltage of 10 kV is plotted in Figure 5.4. With increasing T_{rot} , the peak of the beam profile shifts towards smaller y -values, while, at the same time, the intensity in the undeflected part of the beam profile is reduced. From the comparison of experimental data and simulation an uncertainty of T_{rot} of ± 0.2 K is estimated.

The deflection of iodobenzene molecules (IB, $\text{C}_6\text{H}_5\text{I}$) is investigated in the same way. Vertical intensity profiles are measured by recording the signal of I^+ ions, created by Coulomb explosion with a circularly polarized probe pulse, as a function of the vertical position of the probe laser focus. Figure 5.5a shows deflection measurements for IB seeded in 90 bar of He. IB (mass 204 u) is heavier than BN (mass 103 u) and has a considerably smaller dipole moment of only 1.625 D [163] compared to BN. Therefore, smaller deflection amplitudes are observed for IB under identical expansion conditions. However, the interaction time with the electric field and the time-of-flight from deflector to detection region can be increased when Ne is used as a carrier gas instead of He. Changing the carrier gas reduces the mean velocity of the molecular beam from ~ 1800 m/s to ~ 800 m/s and significantly enhances the observed deflection as shown in Figure 5.5b.[†] Following the fitting procedure outlined above, T_{rot} can be determined for IB as well. In the case of IB, a one-temperature model with a rotational temperature of 1.05 K fits the experimental data best for the deflection measurements in helium as well as in neon. The uncertainty of T_{rot} is estimated to be ± 0.1 K for IB seeded in Ne and ± 0.2 K for IB in He. The somewhat larger uncertainty for the measurements in He reflects the small deflections observed for He. The simulated deflection profiles for IB are shown

[†]Producing even slower beams by using heavier carrier gases like Ar, Kr, or Xe is inhibited by the onset of clustering in the gas jet and the resulting loss of flux.

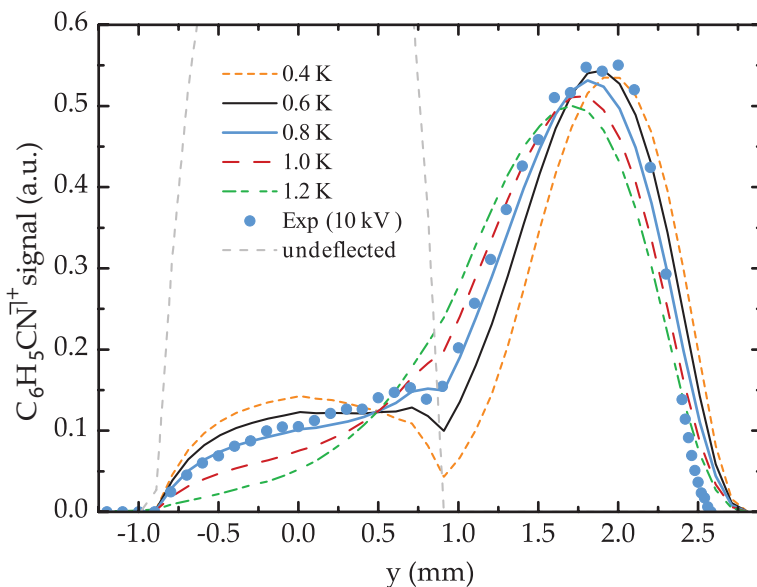


Figure 5.4: The vertical profile of the molecular beam measured by recording the laser-induced BN^+ signal (see text). The experimental data (symbols) are shown together with the corresponding simulated profiles (lines) for different rotational temperatures. Simulations are shown for the two-temperature model; see text for details. Note that the same scale as in Figure 5.3 is used and the peak value for the undeflected beam is 1.

as solid lines in Figure 5.5 and agree well with the experimental data.

The main purpose of the deflection studies presented in this work is to provide quantum-state-selected samples of large molecules for further experiments. The degree of deflection that a molecule experiences in the electric field of the deflector depends on its quantum state. The relevant quantity is the effective dipole moment, which depends on the electric field strength. Molecules residing in low rotational quantum states generally have the largest μ_{eff} and are, therefore, deflected the most. These molecules can simply be addressed by moving the laser focus in the detection region towards the upper cut-off of the molecular beam profile. In order to understand the laser-induced alignment and orientation experiments presented in Sections 5.4 and 5.5, it is crucial to know the relative populations of individual quantum states that are probed at a given height of the laser focus. The positions of the laser foci within the molecular beam profile during the alignment and orientation measurements are indicated by arrows in Figure 5.5. At this position, the

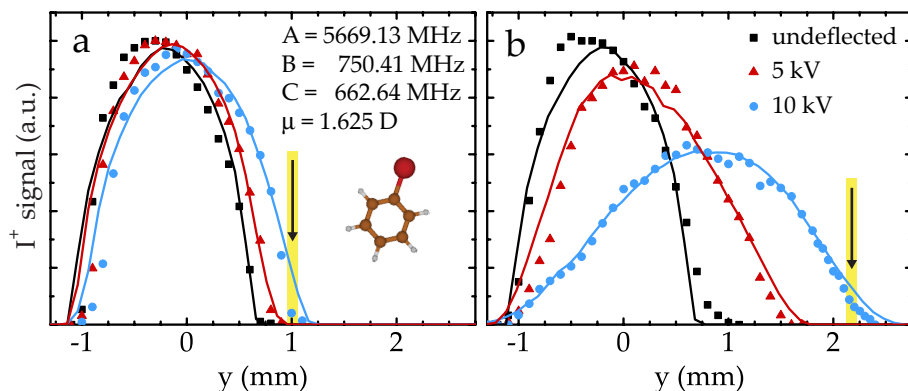


Figure 5.5: The vertical profile of the molecular beam for different deflection voltages applied, measured by recording the laser-induced I^+ signal (see text). The experimental data are shown together with the corresponding simulated profiles. Figure (a) shows the beam profiles for iodobenzene seeded in 90 bar He, and Figure (b) shows the respective profiles for iodobenzene seeded in 20 bar Ne. Arrows indicate the laser positions for alignment and orientation experiments (*vide infra*).

intensity of the deflected beam is 9 % of the undeflected peak intensity. The composition of the molecular packets in the detection region can be extracted from the simulated deflection profiles. Table 5.1 provides an overview of the most abundant quantum states present in different regions of the beam profiles for IB at a rotational temperature of 1.05 K.

For comparison, also the population of each rotational quantum state in the undeflected beam for this rotational temperature is given. At the position of the laser focus for the orientation experiments in Ne (column four in Table 5.1), the population of the lowest quantum states is significantly enhanced in the deflected beam compared to the undeflected beam. The fraction of ground state molecules is enhanced by a factor of five, for instance. About 97 % of the population resides in the quantum states listed in Table 5.1 with the $J_{K_a, K_c} = 3_{03}$ state being most abundant. Moving the laser focus even closer towards the upper cut-off in the beam profile should reduce the number of quantum states that are probed even further. If a reduction of the beam intensity by two orders of magnitude (compared to the undeflected beam) can be afforded, only 4 quantum states are predicted to be probed with 37 % of the molecules being in the $J_{K_a, K_c} = 3_{03}$ state. At first glance, it is surprising that this state and not the absolute ground state, which is expected to have the largest μ_{eff} , is populated the most in the deflected beam. In order to understand this, the Stark curves for the most deflected quantum states of IB are shown in Figure 5.6 a, together

5 Laser-induced alignment and orientation

$J_{K_a K_c}$	M	IB in He (at $0.01 \cdot I_{\text{peak}}$)		IB in Ne (at $0.01 \cdot I_{\text{peak}}$)		IB in Ne (at $0.09 \cdot I_{\text{peak}}$)		free jet
		$P_M(\%)$	$\Sigma P_M(\%)$	$P_M(\%)$	$\Sigma P_M(\%)$	$P_M(\%)$	$\Sigma P_M(\%)$	$P_{J_{K_a K_c}}^{\text{free}}(\%)$
0 ₀₀	0	17.51	17.51	26.06	26.06	6.24	6.24	1.15
1 ₀₁	0	0.02	7.71			3.90	13.61	3.24
	1	7.69				9.70		
1 ₁₁	0	1.92	17.58	23.84	23.84	2.37	7.79	1.55
	1	15.66				5.43		
1 ₁₀	0	1.81	1.82			2.41	6.26	1.55
	1	0.02				3.86		
2 ₀₂	1					0.57	7.74	4.75
	2					7.17		
2 ₁₂	0		3.22			0.23	7.90	2.28
	1					3.51		
	2	3.22				4.16		
3 ₀₃	0	0.01	29.73	36.61	36.61	2.93	19.00	5.47
	1	6.17				7.17		
	2	23.55				8.01		
	3					0.89		
3 ₁₃	2					0.20	2.98	2.65
	3					2.79		
4 ₀₄	0	0.01	3.99			2.12	7.68	5.43
	3	3.98				5.56		
4 ₁₃	1		10.52	13.49	13.49	2.12	7.58	2.54
	2	2.17				2.60		
	3	8.35				2.87		
5 ₀₅	1					0.19	6.73	4.80
	2					3.24		
	4					3.30		
5 ₁₄	0		1.66			0.08	1.90	2.22
	4	1.66				1.83		
5 ₂₃	3	0.06	5.67					1.92
	4	5.61						
6 ₁₆	2					0.19	1.26	1.91
	3					1.07		
Σ			99.41		100.00		96.67	41.46

Table 5.1: Relative population of individual quantum states in the deflected part of the molecular beam profile for $T_{\text{rot}} = 1.05$ K. Left: IB in He at 1 % of the peak intensity of the undeflected beam. Center: IB in Ne at 1 % of the peak intensity of the undeflected beam. Right: IB in Ne at 9 % of the peak intensity of the undeflected beam (here orientation images were taken). P_M denotes the relative population of individual M -sublevels in %, $P_{J_{K_a K_c}}$ the sum over all M -sublevels, and $P_{J_{K_a K_c}}^{\text{free}}$ the relative population of a given rotational quantum state in a free jet.

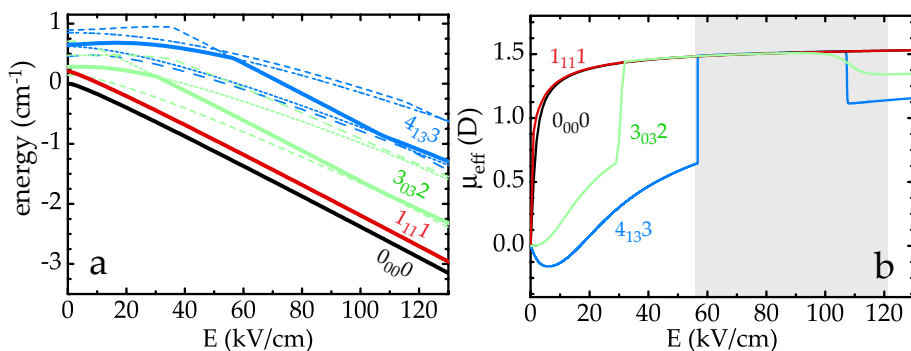


Figure 5.6: (a) Energy as a function of the electric field strength for selected quantum states of IB. Solid lines represent quantum states that are present close to the upper cut-off of the molecular beam profile for IB seeded in Ne. The respective $J_{K_a K_c} M$ quantum numbers are given in the figure. (b) Effective dipole moment for selected quantum states of IB. The shaded area represents the range of electric field strengths in the deflector at 10 kV.

with their effective dipole moments (Figure 5.6 b). Below the relevant electric field strengths both the $J_{K_a K_c} M = 3_{03}2$ and the $J_{K_a K_c} M = 4_{13}3$ M -sublevels have avoided crossings with close-by states of the same symmetry (dashed lines in Figure 5.6 a). These avoided crossings lead to large local effective dipole moments that are comparable to the ground-state μ_{eff} .[‡] Thus molecules in these quantum states are deflected as much as ground-state molecules. Furthermore, states with $M \neq 0$ are doubly degenerate, whereas the ground state with $M = 0$ is only singly degenerate. Therefore, the population of molecules in the $J_{K_a K_c} M = 3_{03}2$ in the undeflected beam is already larger than the population in the ground state.[§] From Table 5.1 it is clear, that it will be difficult to isolate the rotational ground state of iodobenzene in the present setup. Nevertheless, given that the fraction of ground-state molecules could be increased from 1 % in the undeflected to 26 % in the deflected beam, dramatic effects are to be expected for a variety of further experiments.

[‡]On the other hand, the local effective dipole moments of the neighboring states (dashed lines in Figure 5.6 a) are reduced by these crossings. At an avoided crossing, the two levels that are involved “exchange” their effective dipole moments. For large asymmetric top molecules, many avoided crossings can lead to a complicated shape of the adiabatic Stark curve and a strongly varying effective dipole moment with the electric field strength.

[§]In principle, deflection of the quantum states that are coincidentally polar for the range of electric field strengths in the deflector could be reduced by operating the deflector at a different high voltage. However, due to the large number of quantum states populated and the resulting large number of avoided crossings, other quantum states might be coincidentally polar for these operation conditions.

It is pointed out, that adiabatic following of potential energy curves is assumed in all simulations. Non-adiabatic transitions are unlikely in the strong fields inside the deflector, since the number of avoided crossings decreases and their energy gaps generally increase with electric field strength. Moreover, the probability for non-adiabatic following depends on the rate of change of the field strength, which is only due to the slow translational motion of the molecules. However, non-adiabatic transitions have been observed in different Stark-decelerator beamlines at real [72] and avoided crossings [164] for small electric fields. Similarly, when the deflected molecules in the experiments reported here enter a field-free region, scrambling of population over the various M -components of their rotational state will occur.

For small molecules, like OCS or ClCN, the preparation of an ensemble of molecules, all in a single quantum state will be feasible with the present setup. For these systems the number of quantum states that are populated in a supersonic jet is significantly smaller compared to large asymmetric top molecules like IB or BN. The spacing between neighboring quantum states is larger and the number of avoided crossings smaller. Thus, the differences in the effective dipole moment between individual quantum states are larger and, therefore, the degrees of their deflection will vary considerably.

5.4 Laser-induced alignment of quantum-state-selected large molecules

Now, the alignment induced by the YAG pulse is studied. The basic experimental observables are 2D I^+ ion images recorded when the iodobenzene molecules are irradiated with both the YAG pulse and the probe pulse. The geometry of the laser pulse polarizations with respect to the velocity map imaging spectrometer (VMI) is illustrated in Figure 5.7. The YAG pulse is linearly polarized along the vertical direction, i. e., in the detector plane. The probe pulse is linearly polarized perpendicular to the detector plane, which ensures that there is no detection bias on the molecular orientation in that plane. This results in a circularly symmetric I^+ image, when only the probe pulse is used (Figure 5.8 A1). When the YAG pulse is included (Figure 5.8 A2-A4) the I^+ images exhibit strong angular confinement along the polarization of the YAG pulse. The I^+ ions appear as two pairs of radially localized regions, corresponding to two different fragmentation channels of the Coulomb explosion. The radius of the outermost (and weakest) pair of rings is approximately $\sqrt{2}$ times larger than the radius of the innermost (and brightest) pair of rings. Since the radius is proportional to the velocity of the ions, the I^+ ions from the outermost pair of rings originate from a Coulomb explosion channel that releases twice as much kinetic energy as the channel producing the I^+ ions in the innermost pair of rings. As pointed

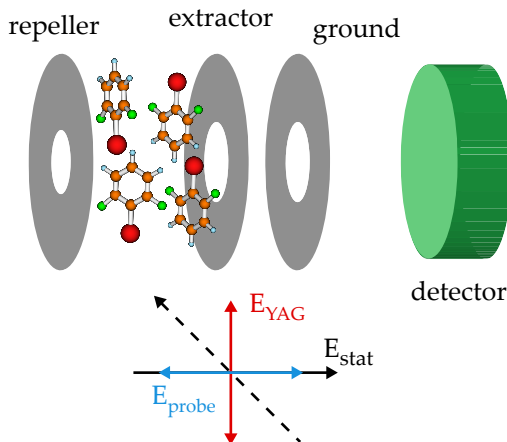


Figure 5.7: Schematic illustration of the polarization state of the YAG and the probe pulse with respect to the static electric field and the detector plane for the alignment measurements. The dashed line represents the propagation directions of the laser beams. Included is also a sketch of the resulting molecular alignment. Repeller, extractor and ground refers to the electrostatic plates of the velocity map imaging spectrometer.

out in several previous studies (see for instance reference [165]) this is only consistent with the innermost pair of rings originating from iodobenzene being doubly ionized by the probe pulse and fragmenting into an $I^+ + C_6H_5^+$ ion pair, and the outermost pair of rings originating from I^+ ions formed by triple ionization and fragmentation into an $I^+ + C_6H_5^{2+}$ ion pair. The pronounced angular confinement observed in images A2-A4 is quantified by calculating the expectation value of $\langle \cos^2 \theta_{2D} \rangle$, where θ_{2D} is the angle between the YAG pulse polarization and the projection of the I^+ recoil velocity vector onto the detector plane. In this work, $\langle \cos^2 \theta_{2D} \rangle$ values are calculated only from ions detected in radial region corresponding to the $I^+ + C_6H_5^{2+}$ channel. By doing so, the YAG intensities probed are restricted to a narrow range close to the maximum value, as the high nonlinearity of the multiphoton process occurs efficiently only in the spatial regions close to the focal point of the YAG beam.

Image A1, recorded with only the probe pulse present, corresponds to a target of randomly oriented molecules. As expected the image is circular symmetric and $\langle \cos^2 \theta_{2D} \rangle = 0.515$. When the YAG pulse is included (image A2) a pronounced angular confinement is observed along the polarization of the YAG pulse and $\langle \cos^2 \theta_{2D} \rangle$ is increased to 0.947. These observations are in complete agreement with previous studies [166]. When the deflector is turned on and the laser foci moved to the edge of the most deflected molecules (at

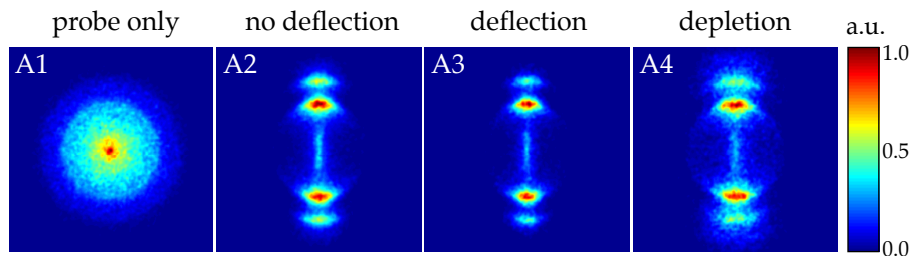


Figure 5.8: I^+ ion images illustrating alignment, recorded when the probe pulse Coulomb explodes the iodobenzene molecules seeded in He. The polarizations of the YAG and the probe pulses are kept fixed as illustrated in Figure 5.7. The labels “no deflection”, “deflection”, and “depletion” correspond to images recorded at lens position $y = 0.0$ mm, 1.0 mm and, -0.9 mm respectively, the latter two with the deflector at 10 kV (see Figure 5.5). The intensities of the YAG and probe pulses are 8×10^{11} W/cm² and 5×10^{14} W/cm², respectively. The color scale indicates the relative number of ions. This color scale is the same for all subsequent figures showing ion images.

the position marked in Figure 5.5 a), corresponding to molecules in the lowest rotational states, the angular confinement is further enhanced leading to a $\langle \cos^2 \theta_{2D} \rangle$ value of 0.968 (image A3). By contrast, when the experiment is conducted on the least deflected molecules in the depleted region, corresponding to molecules in the highest rotational states, the alignment is weakened and $\langle \cos^2 \theta_{2D} \rangle = 0.900$ (image A4).

The alignment measurements are repeated with iodobenzene seeded in Ne. The results are displayed in Figure 5.9. Like in the He case a pronounced improvement is observed when deflected rather than undeflected molecules are employed. Figure 5.9 shows images of I^+ recorded at three different intensities of the YAG laser for both undeflected and deflected molecules seeded in Ne. The effect of the deflector is clearly seen when comparing for instance image B1 (deflected) and A1 (undeflected). At this low YAG intensity (2.3×10^{10} W/cm²) weak alignment is obtained in the non-deflected beam with $\langle \cos^2 \theta_{2D} \rangle = 0.695$. Going to the edge of the deflected molecular beam (position indicated in Figure 5.5 b), a clear enhancement is observed with the $\langle \cos^2 \theta_{2D} \rangle$ value rising to 0.869 (image B1). Also, at high YAG intensity (1.2×10^{12} W/cm²) the difference in angular confinement comparing the undeflected (image A3) to the deflected molecules (image B3) is visible. While $\langle \cos^2 \theta_{2D} \rangle = 0.929$ represents the limit of the degree of alignment of iodobenzene seeded in Ne in the undeflected beam, employing the deflector leads to an unprecedented degree of laser-induced

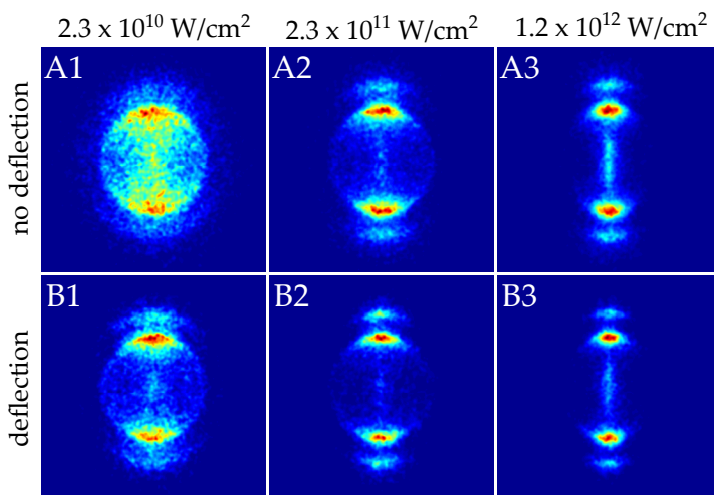


Figure 5.9: I^+ ion images illustrating alignment at different intensities of the YAG pulse, recorded when the probe pulse Coulomb explodes iodobenzene molecules seeded in 20 bar Ne. The labels “no deflection” and “deflection” correspond to images recorded at lens position $y = 0.0$ mm (deflector turned off) and 2.15 mm (deflector at 10 kV), respectively. The intensity of the probe pulse is 5×10^{14} W/cm².

alignment of $\langle \cos^2 \theta_{2D} \rangle = 0.972$. Note that the upper limit for $\langle \cos^2 \theta_{2D} \rangle$ is 1.

To quantify the angular information of the images, the $\langle \cos^2 \theta_{2D} \rangle$ values are plotted as a function of the YAG intensity, and the results are displayed in Figure 5.10. Even at very low laser intensities a high degree of alignment can be obtained from an ensemble of quantum-state-selected molecules. The tendency shown in this graph with a steep rise and early saturation of the degree of alignment agrees with previous results investigating the dependence of alignment on the rotational temperature of the ensemble of molecules [166]. Effectively, the quantum-state selection corresponds to a “colder” albeit non-thermal beam (see Section 5.3).

Note that the contrast between the undeflected and the deflected beam is expected to be greater if Ne is used instead of He as a carrier gas. In the undeflected beam the maximum degree of alignment that can be achieved is smaller in Ne because the rotational cooling in the supersonic expansion is less effective due to the lower stagnation pressure [154]. Additionally, in the deflected beam a better degree of alignment is expected for Ne, as the efficiency of the quantum-state selection in the present setup is significantly enhanced due to the longer residence time in the deflector (see Section 5.3).

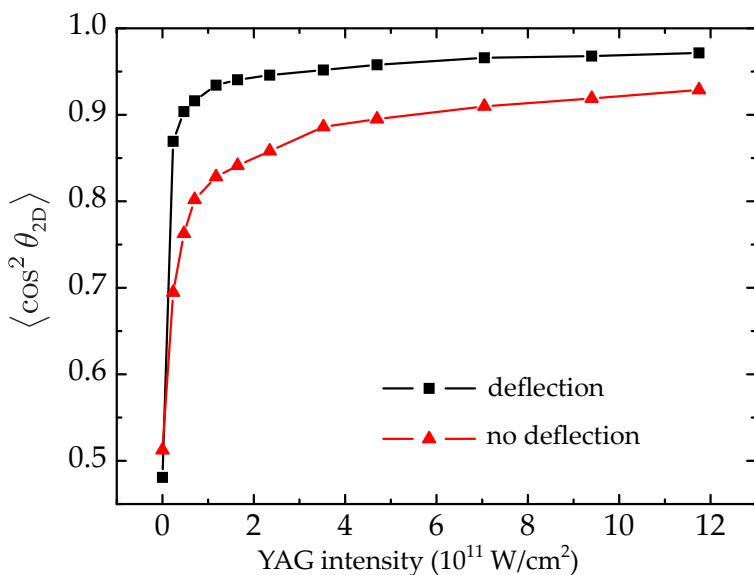


Figure 5.10: Degree of alignment as a function of the YAG intensity for iodobenzene seeded in 20 bar Ne. The labels “no deflection” and “deflection” correspond to images recorded at lens position $y = 0.0$ mm (deflector turned off) and 2.15 mm (deflector at 10kV), respectively. The intensity of the probe pulse is $5 \times 10^{14} \text{ W/cm}^2$.

5.5 Laser-induced orientation of quantum-state-selected large molecules

Next, the orientation due to the combined action on the molecules by the YAG pulse and the static electric field (E_{stat}) from the VMI electrodes [149, 150] is discussed. Figure 5.11 illustrates the polarization state of the YAG and the probe pulse with respect to the static electric field of the VMI electrodes. The important difference compared to the alignment data is that the YAG polarization is rotated away from the axis perpendicular to the static field. Thus, the orientation data result from geometries where the angle β , between the YAG polarization (the C-I bond axis) and the static electric field, is different from 90° - see Figure 5.11. To image orientation a circularly polarized probe pulse is used. This ensures that any molecule will be ionized - and thus detected - with the same probability independent of β . This circularly polarized probe will induce some bias on the angular distribution of the I^+ ions (see Figure 5.12 A1 and C1), however, importantly, it is up/down symmetric. Figure 5.12 shows I^+ ion images for different β values for both deflected and undeflected molecules seeded in He. As mentioned above, the circularly polarized probe alone gives

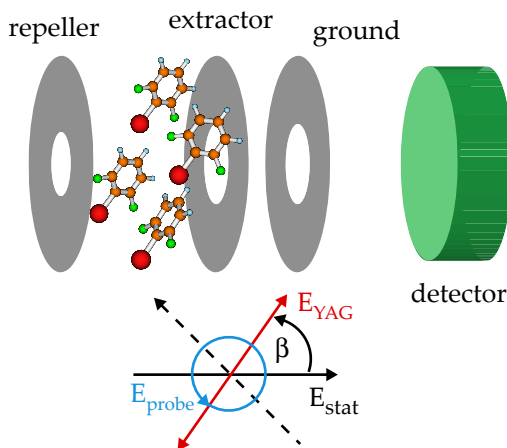


Figure 5.11: Schematic illustration of the polarization state of the YAG and the probe pulse with respect to the static electric field and the detector plane for the orientation measurements. The dashed line represents the propagation direction of the laser beams. A sketch illustrating the molecular orientation is included as well.

rise to an image that exhibits some angular confinement with $\langle \cos^2 \theta_{2D} \rangle = 0.70$ (Figure 5.12 A1). Consequently, including the YAG pulse at $\beta = 90^\circ$ results in an image (Figure 5.12 B1) that appears slightly different from the corresponding image with a linearly polarized probe (Figure 5.8 A2), but still shows that the molecules are tightly aligned.

Focusing first on the non-deflected data of Figure 5.12 (row A and B) two prominent changes are observed as the polarization of the YAG pulse is gradually rotated away from the detector plane (images A2-A6 and B2-B6). First, the location of the I^+ rings shifts closer to the center of the images. This is due to the fact that the C-I axis alignment, and thus the emission direction of the I^+ ions, follows the YAG pulse polarization. When the C-I axis is aligned at an angle β , the magnitude of the I^+ velocity vector recorded on the detector will be reduced by the factor $\sin \beta$. The detrimental effect on the radial (velocity) resolution is obvious at $\beta = 135^\circ / 45^\circ$ (image A5 and B5) and $30^\circ / 150^\circ$ (image A6 and B6), where the two I^+ explosion channels, $I^+ + C_6H_5^+$ and $I^+ + C_6H_5^{2+}$, become indistinguishable as they merge in the 2D projection onto the detector plane.

Secondly, as the YAG pulse polarization is turned away from 90° the up/down symmetry of the images, characteristic for the alignment data described in Section 5.4 (and Figure 5.12 column 1), is broken. For images with

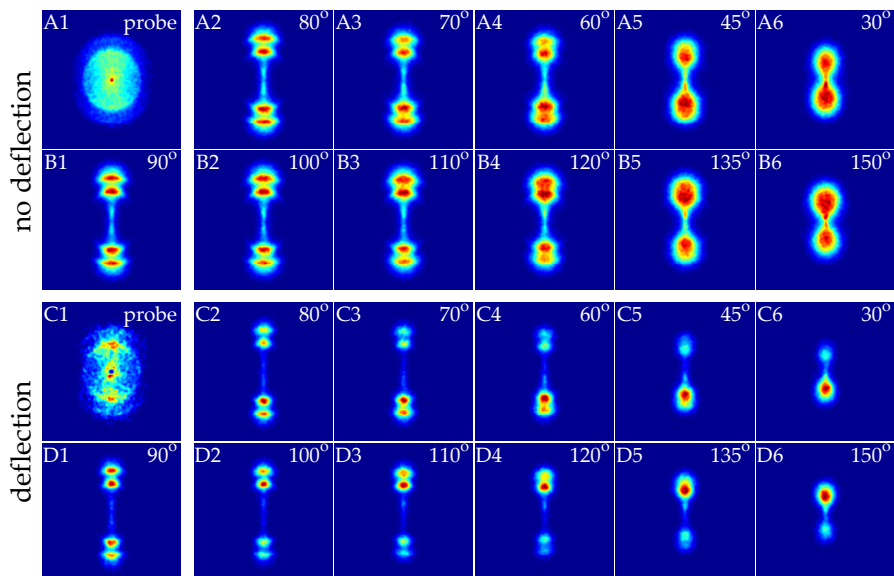


Figure 5.12: I^+ ion images illustrating orientation for different values of β , recorded when the circularly polarized probe pulse Coulomb explodes the iodobenzene molecules seeded in 90 bar He. The labels “no deflection” and “deflection” correspond to images recorded at lens position $y = 0.0$ mm (deflector turned off) and 1.0 mm (deflector at 10 kV), respectively. The intensity of the YAG and the probe pulse is 8×10^{11} W/cm² and 5×10^{14} W/cm², respectively. $E_{\text{stat}} = 594$ V/cm.

$90^\circ < \beta < 180^\circ$ (images B2-B6) more I^+ ions are detected in the upper part, whereas for $0^\circ < \beta < 90^\circ$ (images A2-A6) more I^+ ions are detected in the lower part. The asymmetry becomes more pronounced as the YAG polarization is rotated closer to the axis of the static field. These observations are interpreted as orientation due to the combined effect of the YAG laser field and the projection of the static electric extraction field (E_{stat}) on the YAG polarization axis. This projection (numerical value: $|\cos(\beta)| \cdot E_{\text{stat}}$) increases as β is rotated towards 0° or 180° , which is expected to cause an increase of the orientation [149, 150], in agreement with the experimental findings.

As discussed in Section 5.3, all states of iodobenzene are high-field seeking, hence the orientation is expected to place the I-end of the molecules towards the repeller plate (see Figure 5.11), where the electrical potential is highest, because the dipole moment of iodobenzene is directed along the C-I axis pointing from iodine (“negative end”) towards the phenyl ring (“positive end”). The expected

resulting molecular orientation at a given angle of β is sketched in Figure 5.11. Thus, for $0^\circ < \beta < 90^\circ$ the I^+ ions are expected to preferentially be ejected downwards, and for $90^\circ < \beta < 180^\circ$ they will be ejected upwards. This is in agreement with the up/down asymmetry in the images.

The alignment (image D1) and orientation (images C2–C6 and D2–D6) improves significantly when the deflector is turned on and the foci of the lasers are moved to the position of the most deflected molecules (position marked in Figure 5.5 a). The markedly better orientation resulting in a much more pronounced up/down asymmetry is clearly visible even when the YAG pulse is only turned slightly away from perpendicular, i. e. , comparing deflected and undeflected images for $\beta=100^\circ$ (image C2 and A2) and $\beta = 80^\circ$ (image D2 and B2). From the previous discussion it appears that the highest degree of orientation is achieved when β is rotated towards 0° or 180° . This is clearly seen from the images in row C and D and, again, the improvement obtained with deflected molecules is striking - compare image C6 to A6 (or D6 to B6).

Similar orientation measurements were conducted for iodobenzene seeded in Ne instead of He. Figure 5.13 shows I^+ images at a series of β values for two different intensities of the YAG pulse recorded with the deflector at 10 kV at the position marked in Figure 5.5 b. Compared to the images displayed in Figure 5.12 row A and B, although recorded at slightly different intensities of the YAG pulse, a significant improvement is observed. Furthermore even at low intensity of the YAG a high degree of orientation for iodobenzene seeded in Ne is achieved. At the same time some loss in the angular confinement, i. e. , in the alignment degree, is visible. The clear improvement in the up/down asymmetry is assigned to the more stringent state selection in Ne compared to He as described in Section 5.3, hence, manifesting itself in a higher degree of orientation.

To quantify the up/down asymmetry, i. e. , the degree of orientation, for each image the number of I^+ ions, $N(I^+)_{\text{up}}$, in the upper part of the $I^+ + C_6H_5^+$ and $I^+ + C_6H_5^{2+}$ channels (i. e. , ions detected in the upper half of the images) as well as the total number of ions, $N(I^+)_{\text{total}} (= N(I^+)_{\text{up}} + N(I^+)_{\text{down}})$, is determined. This ratio, as a function of β , is displayed in Figure 5.14. Focusing first on curves C and D, representing iodobenzene seeded in He, the difference between the data for the deflected molecules and the data obtained with the deflector turned off is striking and shows the advantage of selecting the lowest-lying rotational states for strongly increasing the degree of orientation. The further improvement when Ne is used instead of He is clear from curves A and B. These two curves also show that the pronounced degree of orientation is maintained when the intensity of the YAG pulse is lowered by an order of magnitude compared to the maximum value of $1.2 \times 10^{12} \text{ W/cm}^2$.

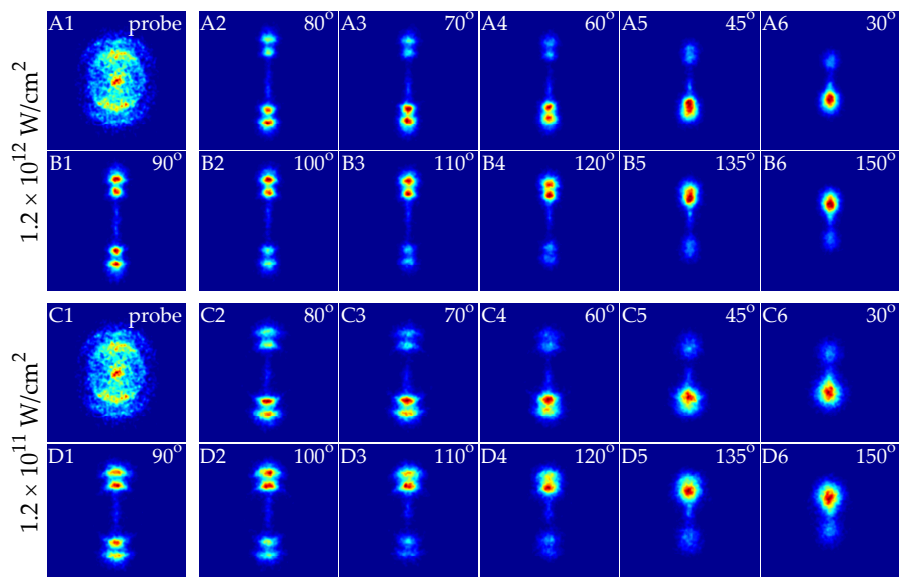


Figure 5.13: I^+ ion images of deflected iodobenzene seeded in 20 bar Ne, illustrating orientation at two different intensities of the YAG pulse. The images are recorded at lens position $y = 2.25$ mm with the deflector at 10 kV. The intensity of the probe pulse is 5×10^{14} W/cm². $E_{\text{stat}} = 594$ V/cm.

5.6 Summary

In conclusion, it is shown that deflection of cold molecular beams with an inhomogeneous static electric field enables the selection and the spatial separation of the most polar quantum states, i. e., the lowest-lying rotational states. The method demonstrated here is complementary to state selection for small molecules using a hexapole focuser, which has been suggested to be applied for improved alignment and orientation experiments [167] and which has recently been experimentally demonstrated [168]. While a hexapole focuser only works for small molecules in low-field-seeking quantum states, beam deflection will apply broadly to a wide range of molecules, from diatomics to large biomolecules. The deflection is strongest for molecules with a large permanent dipole moment to mass ratio. For a given molecule the deflection is optimized by employing stronger deflection fields, increasing the length of the deflector, or lowering the speed of the molecule, for instance, by using neon rather than helium as a carrier gas. For small molecules, the preparation of an ensemble of molecules all in a single quantum state should be feasible. As an application of the state-selected molecules it is shown, that selection of iodoben-

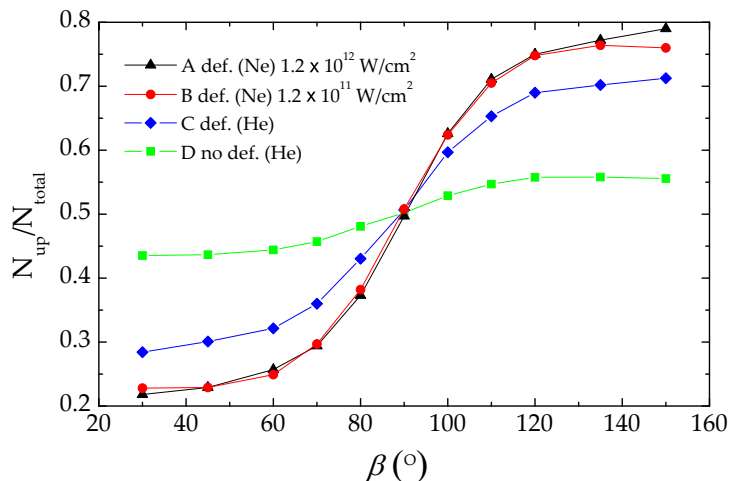


Figure 5.14: Orientation of iodobenzene, seeded in either He or Ne, represented by the number of I^+ ions in the upper half of the image (N_{up}) divided by the total number of I^+ ions in the image (N_{total}) as a function of β . For the experiments conducted with He as a carrier gas, curves C (lens position $y = 1.0$ mm and deflector at 10 kV) and D (lens position $y = 0.0$ mm and deflector off), the intensity of the YAG pulse was 7.8×10^{11} W/cm². For Ne as a carrier gas, curves A and B (lens position $y = 2.25$ mm and deflector at 10 kV), the intensities of the YAG pulse are displayed in the inset. The intensity of the probe pulse for all curves was fixed at 5×10^{14} W/cm², $E_{\text{stat}} = 594$ V/cm.

zene in low-lying rotational states allows to achieve unprecedented degrees of laser-induced adiabatic alignment and mixed laser- and static-field orientation. In particular, it is demonstrated that strong alignment and orientation can be maintained even when the intensity of the alignment pulse is lowered to the 10^{10} – 10^{11} W/cm² range. This can reduce unwanted disturbance from the laser field in future applications of adiabatically aligned or oriented molecules. Note that it should be possible to improve the degree of orientation obtained here simply by increasing the static electric field; due to experimental constraints this has not been implemented in the present work. Getting access to cold molecules in the gas phase typically involves using a molecular beam from a supersonic expansion that usually consists of more than 99 % carrier gas and less than 1 % of the specific molecules. In several types of experiments the atomic carrier gas can contribute to, or even completely overshadow the particular signal measured. The electrostatic deflection naturally separates the polar molecules from the unpolar carrier gas and thus removes this unwanted background. The

density in the original molecular beam is conservatively estimated to be 10^{11} molecules/cm³. In the experiments presented here the density in the deflected part of the beam is approximately 10^{10} molecules/cm³. This density should be sufficient for a variety of applications, such as photoelectron spectroscopy with VUV, EUV [169], or X-ray light sources, including attosecond pulses, or high harmonic generation experiments with fs laser pulses [170]. For all of these applications, which are discussed in more detail in Chapter 8, the separation of the molecular target from the carrier gas might be of great relevance.

Chapter 6

Conformer selection of large neutral molecules with static electric fields*

6.1 Introduction

Many complex molecules exhibit multiple structural isomers, i. e. , multiple local minima on their potential energy surface. About twenty years ago, it was observed, that multiple conformers of tryptophan are present even at the low temperatures of a few Kelvin in a supersonic jet [80]. Since then, these conformers have been studied extensively with sophisticated spectroscopic techniques. Individual conformers can be identified through their distinct electronic [80, 82] or microwave [81] spectra. Information on the conformational structures can be obtained using, for instance, microwave [171] or multiple-resonance infrared spectroscopy [83, 84]. In similar experiments it was even possible to obtain information on the barriers separating the conformers [88]. The preparation of spatially separated conformers would provide unique possibilities for advanced further investigations. It would allow to study directly the chemical properties of the individual species – and the differences between them – in reactive scattering experiments. Such pure samples would also enable a new class of experiments, e. g. , electron [89] and X-ray diffraction [90, 172] or tomographic imaging [91] experiments of complex molecules in the gas phase. Also, ultrafast dynamics studies on the ground-state potential energy surface would benefit from the availability of these pure samples.

*Based on: Pure samples of individual conformers: The separation of stereo-isomers of complex molecules using electric fields, F. Filsinger, J. Küpper, G. Meijer, J. L. Hansen, J. Maurer, J. H. Nielsen, L. Holmegaard, and H. Stapelfeldt, *Angew. Chem. Int. Ed.* **121**, 6900 (2009)

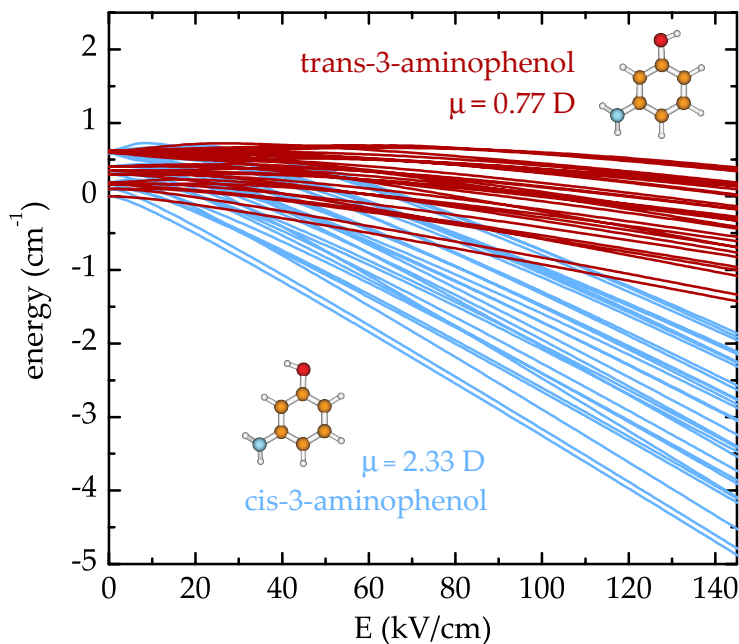


Figure 6.1: Molecular structures, dipole moments, and energies of the lowest rotational states of cis- and trans-3-aminophenol as a function of the electric field strength.

For charged species, the separation of molecules with different shapes has been demonstrated using the ions' mobility in drift tubes [92, 93]. For neutral molecules, the abundance of the conformers in molecular beams can be partly influenced by selective over-the-barrier excitation in the early stage of the expansion [94] or by changing the carrier gas [95]. This chapter describes an approach to spatially separate the conformers of large neutral molecules based on their distinct dipole moments. The conformers of a specific (bio-)molecule all have the same mass, but differ by the relative orientations of their functional groups. These functional groups typically have large local dipole moments associated with them and the vectorial sum of these local dipole moments largely determines the overall dipole moment of the molecule (see Chapter 4). In this work, experiments are conducted on the cis and trans conformers of 3-aminophenol, which are used here as prototypes for the conformers of biomolecules. Figure 6.1 shows the Stark curves for lowest rotational quantum states of both species. As shown in Chapter 5, species with different effective dipole moments can be separated using an electrostatic deflector. From Figure 6.1 it is clear that the effective dipole moments of the states of cis-3-aminophenol are considerably larger than for trans-3-aminophenol and,

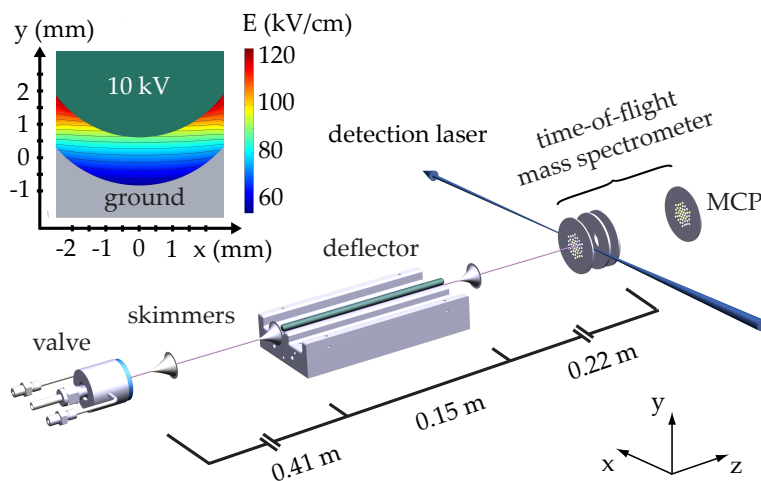


Figure 6.2: Scheme of the experimental setup. In the inset, a cut through the deflector is shown, and a contour plot of the electric field strength is given.

therefore, a strong spatial separation of the conformers can be obtained. The differences between the two conformers are most pronounced for the lowest rotational quantum states and the separation based on electric fields works best, when it is applied to intense beams of rotationally cold molecules produced by a state-of-the-art pulsed supersonic expansion source.

6.2 Experimental setup

A schematic of the experimental setup is shown in Figure 6.2. The same machine as for the experiments presented in Chapter 5 is used, and, since a detailed description is given in Section 5.2, only the differences between the two setups shall be mentioned here. For the experiments on 3-aminophenol (Sigma-Aldrich, 98 % purity) the Even-Lavie valve is heated to 110° C and operated at a backing pressure of 90 bar of helium or 25 bar of neon. In order to detect 3-aminophenol, the molecules are ionized in between the repeller plate and the extractor plate of the VMI spectrometer via resonance-enhanced two-photon ionization by a pulsed dye laser. 10 ns-long pulses focused by a lens with $f = 300$ mm are used with an energy of approximately 0.1 mJ per pulse. The VMI spectrometer is used here as a time-of-flight mass spectrometer and the mass-selected molecular ions are detected by an MCP detector. The two conformers of 3-aminophenol can be detected individually due to their distinct excitation wavenumbers of 34109 cm^{-1} (cis) and 34467 cm^{-1} (trans) [87].

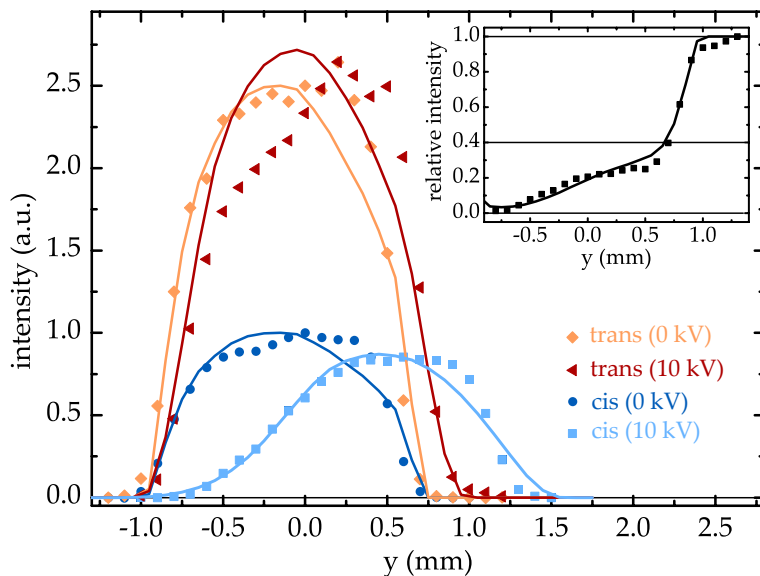


Figure 6.3: Molecular beam intensity profiles of cis- and trans-3-aminophenol seeded in He. Experimental data is given by symbols, simulations by solid lines. The dark blue and orange data are the beam profiles of cis- and trans-3-aminophenol, respectively, without applying voltages to the deflector. The light blue and red curves are the corresponding deflection profiles with high voltage (10 kV) applied to the deflector. In the inset the fractional population of the cis conformer is given, which is obtained by dividing the cis intensity profile by the sum of cis and trans profiles.

6.3 Results

The density of a specific conformer in the molecular beam is measured by recording the number of $\text{C}_6\text{H}_7\text{NO}^+$ ions, created by conformer-selective ionization, as a function of the height y of the detection laser focus. The obtained conformer-selective deflection profiles are shown in Figure 6.3 for 3-aminophenol seeded in He. When a high voltage of 10 kV is applied to the deflector, both conformers are deflected upwards. However, the shift is considerably larger for the more polar cis-3-aminophenol and above $y = 1$ mm a pure sample of cis conformers exists. Additionally, due to the low internal temperature (~ 1 K) of the initial molecular beam, the population of cis-3-aminophenol can be almost completely depleted for heights smaller than $y = -0.75$ mm and an almost pure sample of trans-3-aminophenol remains there. In the inset of Figure 6.3 the fractional intensity of the cis conformer in the deflected molecular beam is shown, which is obtained by dividing the cis intensity profile by the sum of cis and trans

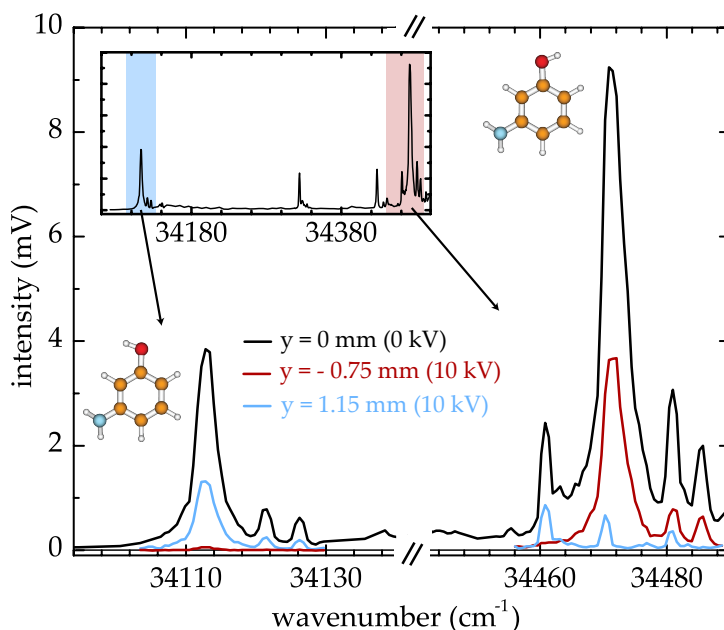


Figure 6.4: Electronic excitation spectra of 3-aminophenol for the original beam (black), the deflected ensemble (blue), and the depleted beam (red). The spectral signatures and the complete discrimination of the individual conformers are clearly demonstrated.

profiles. It is clear, that the fraction of *cis*-3-aminophenol in the probed sample can be continuously tuned by scanning the height of the probe laser focus and, importantly, at heights above the cut-off of the *trans*-3-aminophenol beam profile, the density of the *cis* conformers is still comparable to the density in the free jet. To support the experimental findings, Monte Carlo simulations are performed, as described for benzonitrile and iodobenzene in Chapter 5, and shown as solid lines together with the experimental data. The simulations nicely agree with the experimental deflection profiles. In particular, the fractional intensity of the *cis* conformer can be reproduced very well by the simulations (solid line in the inset).

The clean separation of the two conformers is also confirmed by the vibrationally resolved REMPI spectrum shown in Figure 6.4. The spectrum measured in the deflected part of the molecular beam ($y = 1.2$ mm, blue line in Figure 6.4) only contains bands due to *cis*-3-aminophenol. By contrast, the spectrum measured in the depleted beam ($y = -0.8$ mm, red line in Figure 6.4) shows only three features that can be assigned to the *trans* conformer. Inter-

estingly, a cis transition close to the origin of the trans conformer that cannot be resolved in the undeflected beam becomes clearly visible in the deflected part of the molecular beam. Of course, these conformer-specific UV spectra can also be obtained using double-resonance spectroscopy [129]. However, here these spectroscopic signatures are obtained using a single laser in order to demonstrate the spatial separation of the conformers.

In the experiments presented so far, the deflected cis-3-aminophenol sample is completely separated from trans-3-aminophenol molecules and the atomic seed gas. It is pointed out that the lowest rotational states of cis-3-aminophenol, which are the most polar ones, are deflected the most. As demonstrated in Chapter 5, molecules in these states can be aligned and oriented extremely well, providing the possibility for strong confinement of their rotational motion. On the other hand, the deflected sample of trans-3-aminophenol is separated from the seed gas as well, but still overlaid with cis-3-aminophenol molecules at a density comparable to the peak value in the undeflected beam. The cleanest sample of trans-3-aminophenol is obtained in the depleted part of the beam, where mostly unpolar high- J states are left. These samples are clearly not ideal for alignment and orientation experiments. In order to overcome this problem, the deflection measurements are repeated with neon as the carrier gas, and the results are shown in Figure 6.5. The molecular beam velocity in Ne is smaller compared to He and the transit time through the deflector is increased by about a factor of two. When 5 kV are applied to the deflector in Ne, approximately the same integrated force is applied to the molecules as for a voltage of 10 kV in He. However, due to the longer flight time from the exit of the deflector to the detection region, larger deflection amplitudes are observed in Ne (compare Figure 6.3 and Figure 6.5). Increasing the voltages to 10 kV strongly reduces the cis-3-aminophenol intensity in the detection region. Now the deflection of the cis conformer is so strong, that most of the molecules either hit the top electrode of the deflector or miss the last skimmer and do not reach the detection region. As a consequence, an almost clean sample of trans-3-aminophenol is obtained throughout the intensity profile, in particular also in the deflected part of the beam. These measurements show that, for species with multiple conformers, it might not only be possible to isolate the most polar conformer, but also conformers with intermediate dipole moments, provided that the rotational temperature is low enough and the differences in the dipole moments are big enough.

6.4 Summary

In summary, the spatial separation of the two conformers of the prototypical complex molecule 3-aminophenol using inhomogeneous electric fields is demonstrated. In the experiments with He as the carrier gas, a clean sample of

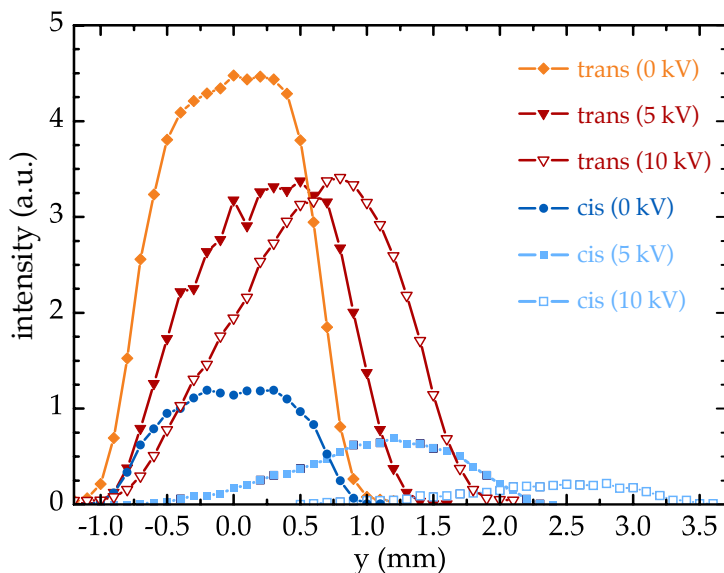


Figure 6.5: Molecular beam intensity profiles of cis- and trans-3-aminophenol seeded in Ne. The dark blue and orange data are the beam profiles of cis- and trans-3-aminophenol, respectively, without applying voltages to the deflector. The light blue and red curves with filled (open) symbols are the corresponding deflection profiles with a high voltage 5 kV (10 kV) applied to the deflector.

cis-3-aminophenol in the lowest rotational states, which are the most polar ones, is obtained. Exploiting the stronger deflection amplitudes that are observed when seeding in Ne, also an almost clean sample of trans-3-aminophenol in low rotational quantum states is obtained. The experiments presented here demonstrate that conformer-specific experiments are completely amenable using the prepared clean samples. While these populations are probed here using focused laser beams, one could perform any conformer-specific experiment either by spatially selective interactions, for example, in X-ray diffraction with upcoming XFEL sources or tomographic imaging using femtosecond lasers, or by completely separating part of the beam from the rest using mechanical means, i. e., adjustable slits. The deflected samples can be aligned or oriented especially well, providing the possibility for strong confinement of the rotational motion of the molecules. Therefore, one can envision to perform stereospecific experiments on these conformer- and state-selected samples.

Chapter 7

Selector for structural isomers of neutral molecules

7.1 Introduction

This chapter describes the implementation of an AC electric focuser for neutral molecules. Large molecules are in high-field-seeking quantum states at the practically relevant electric field strengths. In order to confine these molecules in space alternating gradient focusing has to be applied, which was introduced in Chapter 3. Alternating gradient focusing is a quantum-state-specific process that can be exploited for the spatial separation of molecules in different quantum states with distinct effective dipole moments. This quantum-state selectivity naturally implies that the individual conformers of neutral molecules can be separated – the main purpose of this work. The chapter is organized as follows: Section 7.2 details the experimental setup of the m/μ -selector. In Section 7.3 the selector is characterized by investigating the focusing of ammonia molecules in both low- and high-field-seeking quantum states. Section 7.4 describes a conformer-selection experiment on 3-aminophenol, before the optimization of the device is discussed in Section 7.5.

7.2 Experimental setup

A schematic of the experimental setup is shown in Figure 7.1 a. The molecules to be investigated are seeded in an inert carrier gas and injected through a pulsed valve into vacuum. Details on the preparation of the source and the valves used for the different experiments are given in Section 7.2.1. After passing two skimmers the molecules enter a second, differentially pumped vacuum chamber, where the m/μ -selector is placed (see Section 7.2.2). In brief,

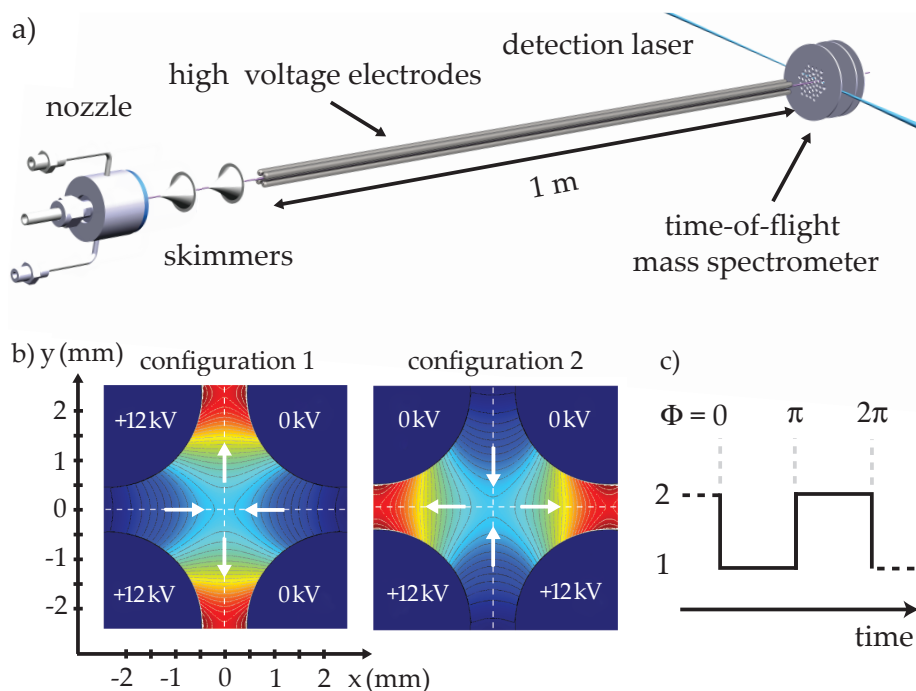


Figure 7.1: a) Scheme of the experimental setup. b) Cut through the high voltage electrodes and electric field configurations; red areas represent regions of strong electric field, blue areas regions of weak electric field. The electric field strength at the center is 45 kV/cm and contour lines are given every 4 kV/cm. White arrows indicate the direction of the force experienced by molecules in high-field-seeking quantum states. c) The electric field is switched in a square wave pattern between configurations 1 and 2.

the selector consists of four polished, 0.99 m-long cylindrical stainless-steel electrodes of 4 mm diameter. High voltages of 12 kV against ground are applied as shown in Figure 7.1 b. The gaps are 0.9 mm* between two adjacent electrodes and 3.0 mm between two opposing electrodes, resulting in a field strength of 45 kV/cm on the centerline and a maximum field strength of 135 kV/cm. Using three high-voltage switches, the field is rapidly switched ($< 1 \mu\text{s}$) between the two electric field configurations shown in Figure 7.1 b (see Section 7.2.3). This switching results in a dynamic focusing of neutral molecules as discussed in Chapter 3. The transmitted molecules are ionized, mass-selected in a time-of-flight mass spectrometer, and subsequently detected using a multi channel plate (MCP) detector. The ionization schemes used for the different experiments are detailed in Section 7.2.4. The molecular beam valve, the high-voltage switching sequences applied to the selector, the detection laser, and the detector are synchronized using a home-built delay generator.

7.2.1 Source

Ammonia

For the experiments on ammonia, a mixture of 12 % $^{14}\text{NH}_3$ and 88 % of Kr is prepared at a pressure of 2 Bar. This mixture is expanded at room temperature into vacuum using a General Valve Series 9 with a 0.8 mm orifice. At these conditions, the mean velocity of the molecular beam is approximately 470 m/s with a velocity spread (FWHM) of $\sim 10\%$. The valve is operated at 10 Hz repetition rate with a home-built pulsed nozzle driver, which provides an electronic pulse for the nozzle with a voltage of 300 V. The opening time of the valve depends on the operation conditions and typically is about 200 μs . Two skimmers (Beam Dynamics Model 2), placed 5 cm and 14 cm downstream from the nozzle, collimate the molecular beam. The first skimmer of 1.5 mm diameter provides a differential pumping stage between the source chamber and the vacuum chamber, where the m/μ -selector is placed. The second skimmer is mounted directly in front of the selector and has a diameter of 1 mm. The pressure in the source chamber, which is pumped by a 520 l/s turbomolecular pump, is $< 2 \cdot 10^{-5}$ mbar with the valve turned on.

3-aminophenol

For the measurements on 3-aminophenol (Sigma-Aldrich, 98 % purity), the same valve and the same skimmers as for the ammonia experiments are used. A sample of 3-aminophenol, which is solid at room temperature, is placed in a custom-made sample holder into the gas inlet system directly behind the valve. The valve itself and the part of the tubing containing the sample are

*The specified value is 0.94 mm. However, in practice the deviation from this ideal value is > 0.1 mm (*vide infra*)

embedded in a copper cylinder that is heated by a resistance wire to 113 °C. The temperature is measured using K-type thermocouples and stabilized to ± 0.2 °C by a proportional-integral-derivative (PID) temperature controller (Eurotherm model 2132). Krypton is used as a carrier gas at a backing pressure of 2 bar resulting in a molecular beam velocity of 480 m/s with a velocity spread (FWHM) of approximately 10 %.

p-aminobenzonitrile

A miniaturized high-pressure Even-Lavie valve [154] with an orifice of 150 μm diameter is used for the experiments on p-aminobenzonitrile (ABN). ABN is bought from Sigma-Aldrich (98 % purity) and dissolved in methanol. Filter paper is soaked with the saturated solution, dried over night at 50 °C in an oven, and placed in the sample reservoir of the valve. The whole valve is heated to 110 °C and operated at 10 Hz, limited by the repetition rate of the detection laser. The valve releases very short pulses – the typical opening time is on the order of 10 μs – and can be operated at backing pressures up to 100 bar. Even though this pressure is much higher compared to the experiments with the General valve, the gas load in the source chamber is actually reduced due to the shorter opening time of the Even-Lavie valve and the smaller nozzle diameter. Using the same turbomolecular pump as for the experiments described above, a pressure of $< 10^{-6}$ mbar can be maintained during operation. Due to the high backing pressure, the molecules are efficiently cooled during the supersonic expansion and rotational temperatures as low as 0.4 K have been reported for aniline seeded in He [160]. For heavier carrier gases, which yield slower molecular beams, the onset of clustering limits the maximum backing pressure that can be used and thus the cooling efficiency [154]. The experiments with the m/μ -selector work best for low beam velocities and low rotational temperatures. Therefore, ABN is seeded in 25 bar of Ne resulting in a mean beam velocity of 900 m/s and a rotational temperature on the order of 1 K, which represents a compromise between optimal cooling on the one hand and a low beam velocity on the other hand. The density in the molecular beam is much higher for the Even-Lavie valve compared to the General valve used for the experiments on ammonia and 3-aminophenol. Therefore, special care has to be taken in the choice of skimmer diameters, skimmer shapes, and distances to avoid disturbing the supersonic expansion. For the experiments presented here, two skimmers (Beam Dynamics model 50.8) are used and placed 15 cm and 25 cm downstream from the nozzle (The bases of the skimmers are still at the same position as for the experiments on ammonia and 3-aminophenol, but the valve is positioned 10 cm further away from the selector). The skimmer diameters are 3 mm and 2 mm, respectively. Both, the increased distance from the nozzle to the skimmers and the larger skimmer diameters compared to the experiments with the General valve, reduce the amount of collisions in the skimmers and ensure optimal expansion conditions for these high-density beams.

7.2.2 Design of the selector

A drawing of the complete selector assembly in the vacuum chamber is shown in Figure 7.2. The selector consists of four highly polished and surface-hardened stainless steel electrodes of 4 mm diameter and 990 mm length. Each electrode is mounted onto a separate aluminum backbone. Three MACOR spacers per electrode provide the electrical insulation against the backbone. The four subunits consisting of electrode, insulators and backbone are attached to a rigid frame. This frame is made of two aluminum rings connected by four 420 mm-long cylindrical stainless steel rods of 16 mm diameter. The frame is suspended with two threaded bolts in two 6 mm-thick plates welded into the two CF100 flanges at the top of the vacuum chamber. The holes drilled into the plates are larger than the bolt diameter so that the horizontal position and the height of the selector, as well as its angle with respect to the molecular beam axis can be adjusted. At the bottom of Figure 7.2 one of the electrode subunits of the selector is shown in more detail. Each high voltage electrode consists of three 330 mm long segments.[†] The two end segments are rounded off with a radius of 2 mm at one end and have flat surfaces with a central 4 mm deep blind hole of 2 mm diameter at the other end. The central segment has flat surfaces with 4 mm deep blind holes of 2 mm diameter at both ends. Neighboring segments are connected by C-shaped soft-iron clamps that fit into these blind holes. This type of connection ensures that the segments are conductibly connected, while at the same time the connection is mechanically flexible enough for the individual segments to be aligned individually. The connection is illustrated in detail in the inset of Figure 7.2 II. Each segment is mounted via two slotted pins to a 16 mm-thick MACOR insulator. The three MACOR insulators with the electrode segments of one subunit are installed together on a polished aluminum cuboid (25mm x 26mm x 760mm). As shown in Figure 7.2, this aluminum backbone is shorter than the electrode, and the outer insulators protrude the backbone. At the side facing the source chamber, the first pin holding the first electrode segment is elongated, reaches through the insulator, and is used to connect the electrode with a tantalum wire of 0.8 mm diameter to the high-voltage vacuum feedthrough.

It is known that any misalignment of the electrodes relative to each other will strongly effect the efficiency of AG focusing [58, 68, 71]. Therefore, special care is taken to align the electrodes of the selector. First, the three electrode segments of the subunits have to be aligned with respect to each other. For this purpose, the backbone of the electrode subunit is mounted into a home-built alignment tool. This tool holds the electrode parallel to a flat marble surface

[†]This approach was taken for technical reasons: It is very difficult to manufacture long electrodes of 4 mm diameter with high precision. Furthermore, all holes had to be eroded into the surface hardened electrodes and the dimensions of the eroding machine available posed an upper limit for the length of the segments.

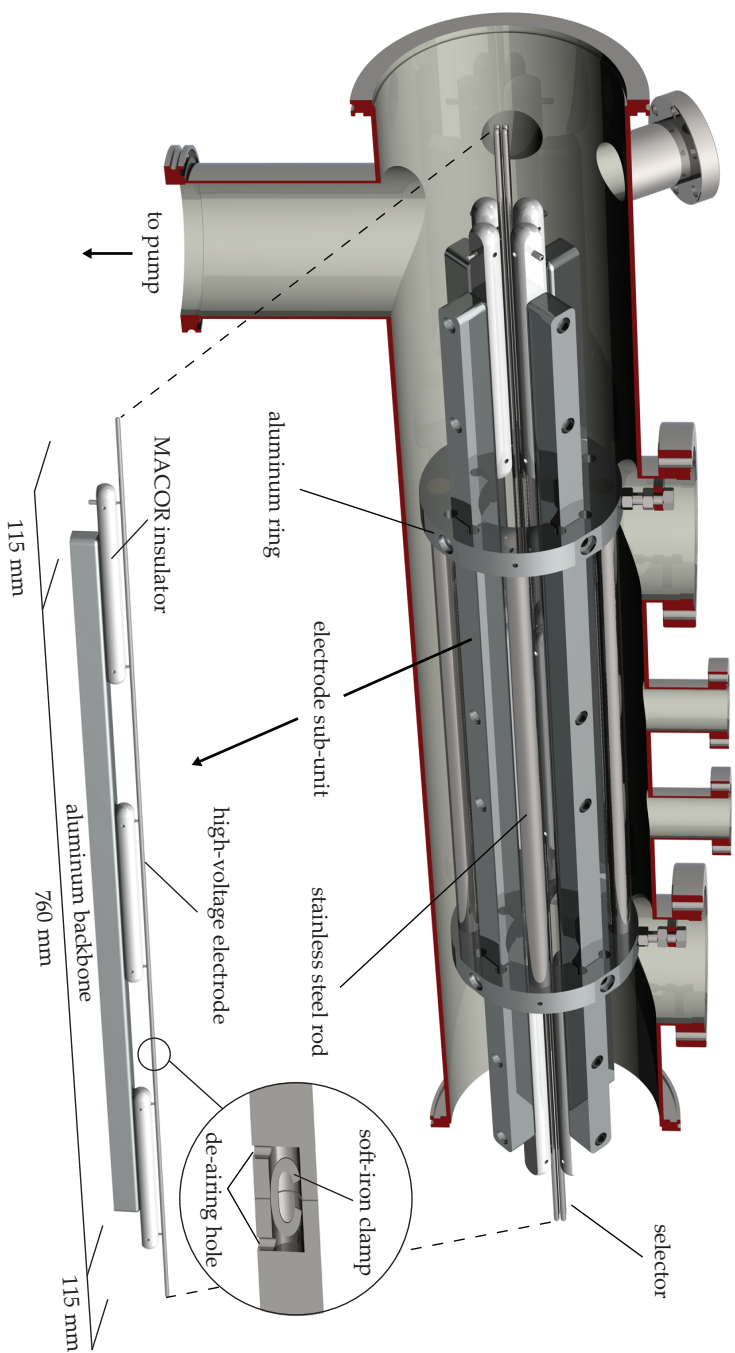


Figure 7.2: Top: The selector mounted in the vacuum chamber. Bottom: The electrode subunits consisting of aluminum backbone, MACCOR insulators, and high-voltage electrode. The high-voltage electrode is composed of three segments that are connected with soft-iron clamps, as illustrated in the inset.

with the surface normal of the electrode that points towards the molecular beam axis being perpendicular to the surface of the marble plate. By slightly pushing the segments into the slotted mounting pins or slightly pulling them out of these pins, the surfaces of the individual electrode segments are aligned to be parallel and at a constant height relative to the surface of the marble plate. Now the alignment tool is rotated by 90° so that the surface normal of the electrode that points towards the molecular beam axis is parallel to the surface of the marble plate. By slightly loosening the holding screws of the MACOR spacers and adjusting the spacer's positions using micrometer screws, the now upwards pointing surfaces of the electrode segments are aligned. The complete procedure is iterated several times to ensure optimal alignment of the electrode subunits. Note that the parallelism of the electrodes with respect to the marble surface is limited by the straightness of the individual electrode segments, which are bent due to the machining process, rather than by the accuracy of the alignment procedure.

Finally, the four electrode subunits are mounted into the rigid frame and aligned with respect to each other. This is achieved by adjusting the gaps between adjacent electrodes using precisely manufactured polyimide disks. The deviations of the gap sizes from the specified value are approximately $100\ \mu\text{m}$ in the central part of the selector. At both ends the deviations are slightly larger ($\sim 150\ \mu\text{m}$). Here, the individual electrode segments are rounded off and deviate more from the ideal straight form than in the center of the selector.

7.2.3 High-voltage switching schemes

A schematic of the electronics is shown in Figure 7.3. The individual electrodes $E1 - E4$ are connected via high-voltage vacuum feedthroughs to fast 30 kV push-pull switches (Behlke Electronics, denoted as $S1 - S4$) operating at positive high voltages. The voltages are switched in $< 1\ \mu\text{s}$ between ground potential and +12 kV. Trigger pulses are provided by a home-built burst unit (FHI ELab BU1708) with a time resolution of 10 ns. This burst unit is synchronized to the molecular beam valve using a home-built delay generator (FHI ELab DG 3008). Both units are controlled with the program package KouDA [173]. The high voltages are provided by a single 20 kV power supply (FuG, HCK400-20000, 40mA), which loads four 14.1 nF capacitors – one capacitor for each electrode – via a high-voltage tee junction. The capacitors are included to minimize the voltage drop over one switching sequence. Figure 7.4 illustrates the waveforms applied to the high-voltage electrodes. In order to create the electric field configurations required for AG focusing (see Figure 7.1 b), three of the four switches are required. Electrode $E4$ is kept at ground potential and $E2$ is switched to high voltage for the full duration of the switching sequence. Electrodes $E1$ and $E3$ are switched between ground potential and a positive high voltage with a frequency of 1-10 kHz and a relative phase difference of

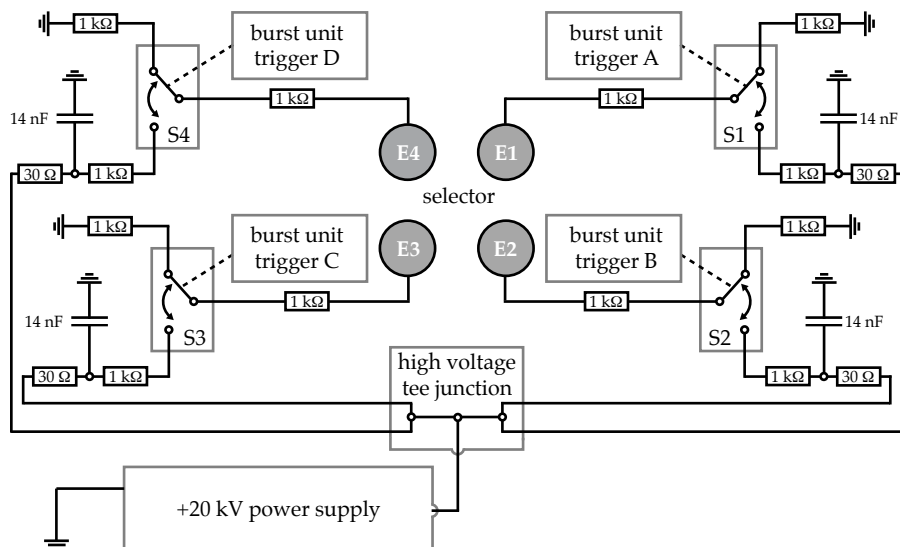


Figure 7.3: Schematic of the electronics setup used for the m/μ -selector. Using high-voltage push-pull switches (denoted as S1-S4) that are triggered by the burst unit, the voltages applied to the electrodes E1-E4 is switched between a positive high voltage and ground potential.

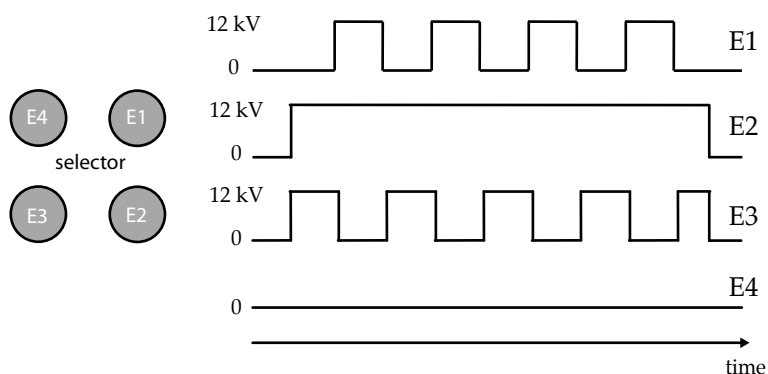


Figure 7.4: Schematic depiction of the waveforms applied to the electrodes of the selector.

180°. For all measurements – except for the experiments on ammonia, where the high voltage is varied – the selector is operated at 12 kV.

Before the selector is operated for the first time, it is exposed to DC voltages in a procedure called “current conditioning” [174] to reduce the risk of electric discharges and potential damaging of the electronic equipment. In this procedure, a small DC voltage is applied to one of the electrodes and slowly but continuously increased to 5 kV, while the other three electrodes are grounded. The currents through the individual electrodes, limited by 100 M Ω resistors, are monitored using digital multimeters. If no currents larger than 50 nA are observed within 10 minutes, the voltage is increased by 1 kV for voltages between 0 and 10 kV and by 0.5 kV otherwise. If larger currents are observed, the high voltage is kept constant for another ten minutes. This process is repeated until a DC voltage 15% above the voltage to be used during normal operation is reached. Here, a DC high voltage of 14 kV is successfully applied corresponding to a maximum field strength of 155 kV/cm on the surface of the electrodes. The conditioning procedure is performed for all electrodes everytime the selector has been exposed to air.

7.2.4 Detection

In all experiments presented in this chapter, the molecules are ionized in between the plates of a time-of-flight mass spectrometer (TOF-MS) using a resonance-enhanced multiphoton ionization (REMPI) scheme (see Figure 7.1). The molecular beam enters the detection region parallel to the axis of the TOF-MS through a mesh (for the experiments on ammonia and p-aminobenzonitrile) or a 2 mm circular aperture (for the experiments on 3-aminophenol) in the repeller plate. The mass-selected ions are detected in an MCP detector. The current generated by the MCP is converted to a voltage, amplified, and read out by a digital oscilloscope (Acquiris DC440), which is synchronized to the detection laser. Figure 7.5 illustrates the different REMPI schemes employed to detect the individual species.

Ammonia molecules in the $X(0)$, $J_K = 1_1$ state, the rotational ground state of para-ammonia, are ionized in a (2+1)-REMPI scheme, as shown in Figure 7.5 I. Molecules in the lfs $MK = -1$ component are selectively ionized via the $B(5) \leftarrow X(0)$ transition at 312 nm, whereas molecules in the hfs $MK = 1$ component are ionized via the $B(4) \leftarrow X(0)$ transition at 317 nm. The specific rotational lines used to detect the molecules are colored in the spectra shown in Figure 7.6, which are measured in the focused beam. The required laser light is obtained by frequency doubling the output of a pulsed dye laser (Radiant Dyes Narrowscan) that is pumped by a Nd:YAG laser (Innolas Spitlight 600). Typically, ~ 10 ns-long pulses with an energy of 0.5 mJ/pulse and a spectral bandwidth of 0.15 cm^{-1} are focused into the detection region by a lens with a focal length of 20 cm. The lens is mounted together with the last mirror on a

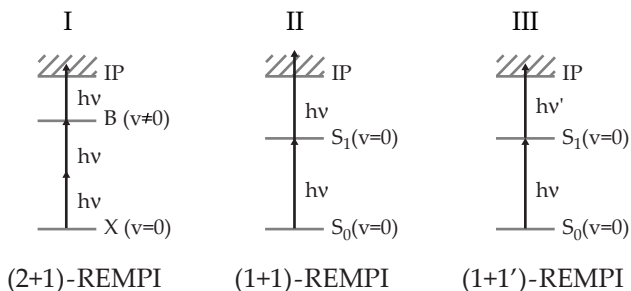


Figure 7.5: Illustration of the three resonance-enhanced multiphoton ionization (REMPI) schemes applied in this work. I) Ammonia is detected using (2+1)-REMPI. II) p-aminobenzonitrile is detected using (1+1)-REMPI. II) 3-aminophenol is ionized in a (1+1')-REMPI scheme using two lasers pulses with different frequencies ν and ν' .

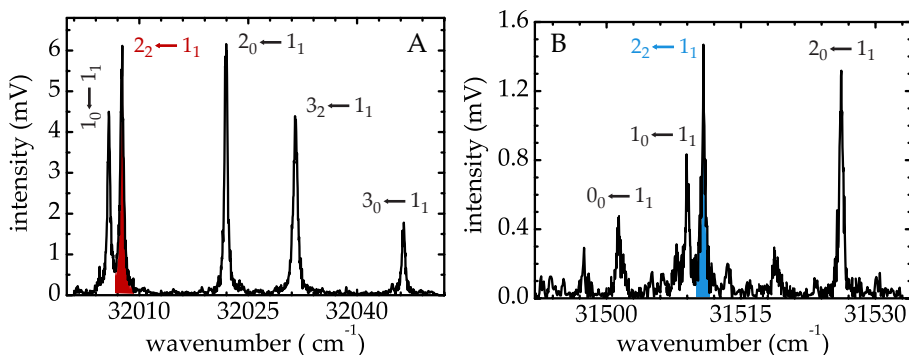


Figure 7.6: Rotationally resolved (2+1)-REMPI spectrum of NH_3 . The labels indicate the $J'_{K'} \leftarrow J_K$ quantum numbers for the individual lines. Molecules in the lfs $MK = -1$ component of the $J_K = 1_1$ state are ionized via the $B(5) \leftarrow X(0)$ transition (Figure A, measured at $\nu=4.90$ kHz and 10 kV), molecules in the hfs $MK = 1$ component are ionized via the $B(4) \leftarrow X(0)$ transition (Figure B, measured at $\nu=3.95$ kHz and 10 kV). The colored spectral lines are used to detect the molecules in the subsequent experiments.

vertical translation stage to adjust the height of the laser focus in the detection region. The detection laser intersects the molecular beam under an angle of 90° , 4 cm behind the selector and 1.21 m downstream from the nozzle.

For the experiments on 3-aminophenol, a (1+1')-REMPI scheme is used, as shown in Figure 7.5 III. The molecules are resonantly excited via the $S_1(v = 0) \leftarrow S_0(v = 0)$ transition at 290 nm using a pulsed dye laser (Radiant Dyes Narrowscan) and subsequently ionized by the 3rd harmonic of a Nd:YAG laser at 355 nm (Spectra Physics Quanta Ray). The cis and trans conformers can be selectively detected due to their distinct $S_1 \leftarrow S_0$ excitation wavenumbers of 34109 cm^{-1} and 34467 cm^{-1} , respectively [87]. The laser beams used for excitation and ionization are unfocused, and have diameters of 4 mm and 2 mm, respectively. To minimize saturation effects, the pulsed dye-laser for electronic excitation is reduced to $20 \mu\text{J}/\text{pulse}$, while the ionization laser is operated with $5 \text{ mJ}/\text{pulse}$. Because the lifetime τ of the electronically excited state is short ($\tau \sim 7 \text{ ns}$), the relative timing of the two laser pulses is adjusted with sub-ns precision by triggering the Q-switches of both lasers using the same delay generator (Stanford Research DG535).

In order to detect ABN, the molecules are ionized in a (1+1)-REMPI scheme (see Figure 7.5 II) via the $S_1(v = 0) \leftarrow S_0(v = 0)$ transition at 299 nm [175] using the frequency-doubled output of a pulsed dye laser (Radiant Dyes Narrowscan). The laser beam is unfocused, has a diameter of 3 mm and an energy of $1 \text{ mJ}/\text{pulse}$.

7.3 Alternating gradient focusing of ammonia

In order to characterize the m/μ -selector, initial experiments are performed using NH_3 in its $J_K = 1_1$ rotational state. NH_3 in this state exhibits a quadratic Stark effect at low and moderate electric field strengths that converges to a linear Stark shift once the Stark energy is comparable to the inversion splitting, as shown in Figure 7.7. Ammonia molecules in the $M_K = -1$ component are low-field seeking and can be focused using a static quadrupole field, which has been exploited already by Gordon and Townes in the original demonstration of the MASER [18, 19]. Also during the initial optimization of expansion conditions and laser detection in the present work a static quadrupole field is applied. Ammonia molecules in both polar quantum states ($M_K = -1$ and $+1$) can be confined to the beam axis using AG focusing as demonstrated by the measurements shown in Figure 7.8. The transmission of NH_3 in its hfs $J_K = 1_1, M_K = 1$ state is plotted in Figure 7.8 b as a function of the frequency ν used to switch between the two electric field configurations. At low switching frequencies, the molecules are strongly defocused in one spatial direction and lost from the selector before they are refocused towards the beam axis by switching the field to the second configuration. For $3 \lesssim \nu \lesssim 5 \text{ kHz}$ AG focusing works and the transmission is high with a maximum around 4 kHz. At higher

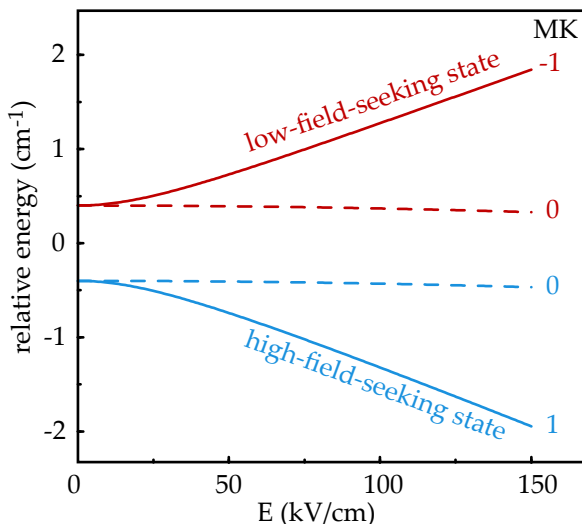


Figure 7.7: The energy of ammonia (NH_3) in its $J_K = 1_1$ rotational state as a function of electric field strength (neglecting hyperfine structure).

frequencies the time averaged potential is approximately flat and no focusing occurs. The overall shape of the transmission curve for ammonia in its lfs $J_K = 1_1, MK = -1$ quantum state, shown in Figure 7.8 a, is different. Similar to the transmission curve for the hfs state, a steep increase of the transmission is observed around $\nu = 3.5$ kHz. The transmission stays high, however, for the whole range of frequencies shown in Figure 7.8 a. This large transmission at high frequencies is due to the fact that the time-averaged electric field (the average of the two electric field configurations depicted in Figure 7.1 b) is not zero, but has a minimum on the molecular beam axis. Therefore, molecules in lfs states are focused, whereas molecules in hfs states are defocused. This minimum has a depth of 7.5 kV/cm, corresponding to a 2-dimensional trap depth for ammonia in its lfs state of 0.11 K.[‡]

The transmission curves shown in Figure 7.8 are clearly modulated for both hfs and lfs quantum states. This modulation is a consequence of the overlap between the strongly focused detection laser ($w_L \sim 40 \mu\text{m}$) and the molecular packet. The shape of the packet depends on the end phase in the switching cycle as schematically depicted in Figure 7.9. Due to the short focuser – corresponding to a short residence time of the molecules in the device – the start phase Φ_{start} , the end phase Φ_{end} , and the switching frequency cannot

[‡]A similar field could, of course, be created by applying DC voltages in a quadrupole arrangement of ± 0.6 kV, although the trap depth and characteristics would be different due to the approximately quadratic Stark effect of NH_3 at the resulting low field strengths.

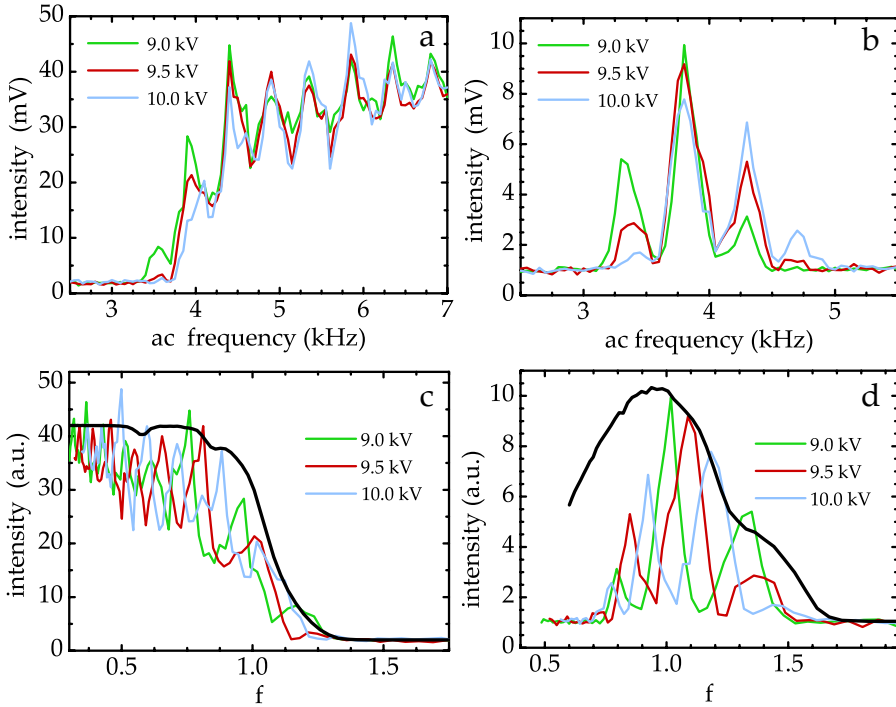


Figure 7.8: Transmission through the selector for ammonia in its lfs ($MK = -1$, left graphs) and hfs ($MK = 1$, right graphs) states of the $J_K = 1_1$ rotational state. a) and b): Transmission as a function of the switching frequency between the two electric field configurations, shown in Figure 7.1 b, for different applied voltages as indicated in the inset. c) and d): The same data plotted as a function of the dimensionless force parameter f introduced in Equation 3.35. The envelope of these data nicely represents the simulated overall transmission through the selector (solid black lines); see text for details.

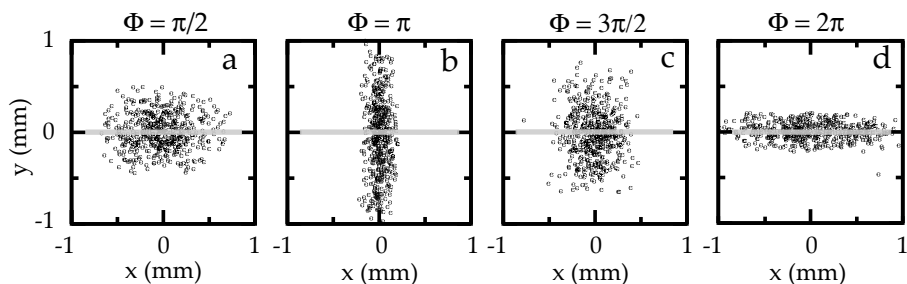


Figure 7.9: Transverse phase-space distribution of the molecular packet in the detection region for $\nu = 4.50$ kHz after 100 switching cycles as a function of the end phase Φ_{end} . The horizontal grey lines schematically depict the area probed by the focused detection laser.

independently be optimized. In Figure 7.8 all transmission curves are measured with a constant Φ_{start} , which, as will be shown later, determines the overall transmission. Φ_{end} is then determined from Φ_{start} and ν . In order to reduce the experimental artifacts of changing phases, the transmission curves are measured for different applied high voltages U . For comparison, the frequencies of these different measurements are then converted to the dimensionless force parameter f introduced in Equation 3.35. This parameter characterizes the effective focusing strength of the selector in the harmonic approximation. The resulting transmission characteristics are displayed in Figure 7.8 c and d. The envelope of these measurements clearly represents the expected overall transmission curve, free of strong effects due to changes in the detection efficiency. The remaining differences between experiment and simulation (shown as black lines in Figure 7.8 c and d) might be caused by misalignment of the electrodes (see Section 7.2.2), which is not included in the simulations. Such misalignment is known to affect both the overall transmission [71] and the shape of the frequency-dependent transmission curve of an AG focusing device [58].

In order to experimentally determine the optimal start phase of the switching sequence, the transmission of ammonia in the $MK = 1$ component is measured as a function of ν with constant Φ_{end} . The resulting transmission curve for $U = 10$ kV is shown in Figure 7.10 together with the calculated start phase. In the measurements presented here, the selector is tilted with respect to the incoming molecular beam by 0.25° in y and 0.21° in x , so that predominantly molecules that are transported through the selector enter the detection region. This tilt will be important for the conformer selection experiments on 3-aminophenol in order to suppress background signal caused by unpolar quantum states (see Section 7.4). For the tilted selector, the largest transmission is observed for $\Phi_{\text{start}} = 0$, i. e., when the switching sequence starts with a half-period of

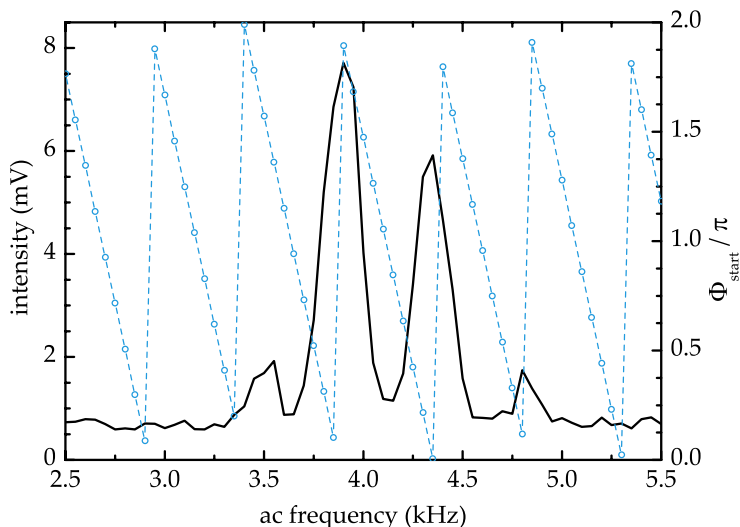


Figure 7.10: Transmission of ammonia in the hfs $MK = 1$ component of the $J_K = 1_1$ rotational state as a function of the AC frequency. The end phase of the switching cycle is 0.125π for all data points and the resulting start phase Φ_{start} is shown in blue.

focusing along the x -axis. A minimum of the transmission is obtained for $\Phi_{\text{start}} = \pi$ corresponding to a start with a half-period of focusing in y . In order to understand these experimental findings, Monte Carlo simulations are employed, which are shown in Figure 7.11. When the axis of the selector coincides with the molecular beam axis (Figure 7.11 a, black curve), the simulations predict the largest transmission to occur for $\Phi_{\text{start}} = 0.5\pi$ and $\Phi_{\text{start}} = 1.5\pi$. For these phases the overlap between the phase space acceptance of the selector and the phase space distribution of the molecules at the entrance of the selector is optimal. For symmetry reasons the two peak transmissions are equally large (for a duty cycle of 0.50). When the selector is slightly tilted away from the molecular beam axis along one transverse direction, this symmetry is broken. For a tilt along the x -axis (y -axis) the transmission is expected to be higher when the switching sequence starts with the field configuration that is focusing in y (x), as depicted in Figure 7.11 a.

In the simulations shown in Figure 7.11 b the selector is tilted in both x and y . For a tilt that is symmetric in x and y two peaks of the transmission are observed in the simulations that are slightly shifted and reduced in intensity compared to the case when no tilt is applied. The peaks are, however, still symmetric with respect to the initial focusing direction. In the experiments the tilt in y is larger than in x and the simulations predict starting the sequence with

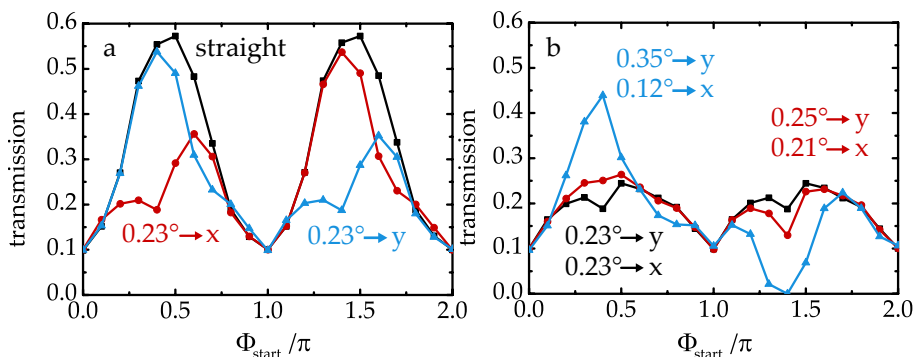


Figure 7.11: Simulated transmission of ammonia in the hfs $M_K = 1$ component of the $J_K = 1_1$ rotational state for $\nu = 4.0$ kHz as a function of Φ_{start} . The individual curves correspond to different tilts of the selector with respect to the incoming molecular beam as indicated in the figure.

focusing in x to work better for this case. This behavior qualitatively agrees with the experiment. The exact value of the optimal start phase, however, differs between experiment and simulations. While the maximum transmission is calculated for $\Phi_{\text{start}} = 0.5\pi$, in the experiment a longer time interval of x -focusing at the start of the sequence is required for maximum transmission. One possible explanation for this observation could be misalignment of the electrodes. Because, as discussed in Section 7.2.2, the misalignment of the electrodes is the largest at the ends of the selector, it will in particular influence the start and end phases of the switching sequence. A misalignment that results in a larger gradient of the electric field along the y -direction than along the x -direction could explain the longer time interval of initial x -focusing needed for optimal transmission and the observed deep minimum of transmission when starting with a too long time interval of y -focusing. The simulations shown in Figure 7.11 b also indicate that a tilt that is more asymmetric in x and y causes the transmission to drop to zero at the wrong start phase – similar to what is observed in the experiment. However, the accuracy of the determination of the tilt applied in the experiment is better than 10% and too accurate to solely explain the features observed in the experimental data.

In order to characterize the spatial profile of the molecular beam, the transmission of ammonia molecules is measured as a function of ν and of the vertical position of the focused detection laser. The measured vertical intensity profiles for ammonia in the lfs and the hfs states are depicted in Figure 7.12. The end phase is constant for all data points and the variation of the intensity with ν is caused by the changing start phase of the switching sequence. For the profiles obtained for the lfs state at $\nu = 4.9$ kHz (A) and $\nu = 5.8$ kHz (B) the full-width-at-half-maxima (FWHM) are determined from Gaussian fits to be

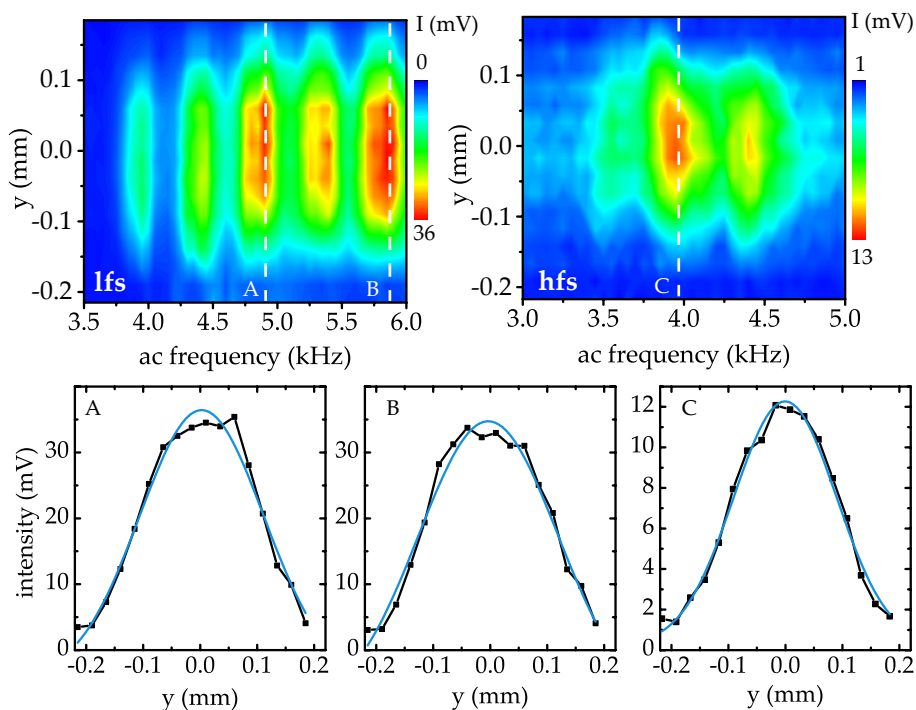


Figure 7.12: Top panel: Intensity I as a function of AC frequency and vertical position y of the detection laser for ammonia in the lfs (left) and hfs (right) quantum states. All data points are measured with fixed end phase. Bottom panel: Vertical intensity profile for the lfs state at 4.9 kHz (A) and 5.8 kHz (B). The vertical intensity profile for the hfs state and an AC frequency of 3.95 kHz is shown in Figure (C). Experimental data are shown in black, Gaussian fits of the experimental data are shown in blue.

0.26(3) mm and 0.29(2) mm, respectively. The width of the focused packet is found to be independent of the switching frequency. The FWHM of the profile of the hfs state (C) is 0.21(1) mm, somewhat smaller than the width of the profile for the lfs state. Molecules in both quantum states can be tightly focused. However, the optimal end phases that are required differ by 180° . At the phase, where molecules in the hfs state are focused along y in the detection region, molecules in the lfs state are focused along x and *vice versa*. This different shape of the molecular packet in the detection region could be exploited to spatially separate the two quantum states using, for instance, narrow slits, even though the transmission occurs at the same frequency for both states.

The measurements presented in this section provide a detailed insight in the focusing properties of the selector and the optimal choice of the phases for

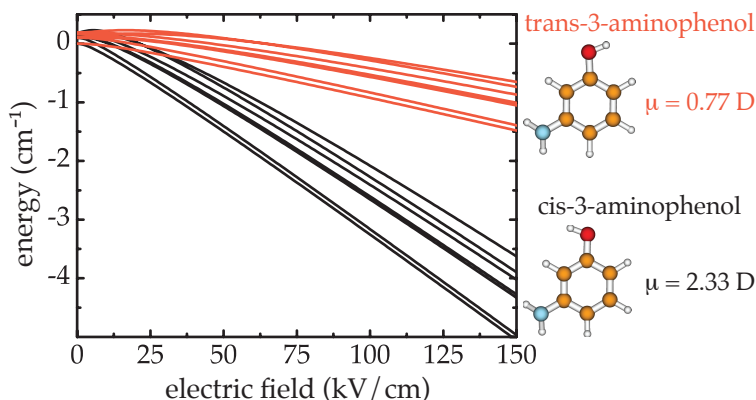


Figure 7.13: Molecular structures, dipole moments, and energies of the lowest rotational states of cis- and trans-3-aminophenol as a function of the electric field strength.

optimal transmission. Starting from the well-defined situation, where only a single quantum state is detected, we can now proceed to more complex systems.

7.4 Conformer selection of 3-aminophenol[§]

In Chapter 6 it has been shown how static electric fields can be used to spatially separate the conformers of large neutral molecules based on their distinct dipole moment to mass ratios. Here, it is demonstrated how the conformer-selective transmission through the AC quadrupole m/μ -selector can be exploited for the same purpose. Experiments are again conducted on the cis and trans conformers of 3-aminophenol, which are prototypical structural isomers of biomolecules. From the precisely known rotational constants and dipole moments [176] the energies of the rotational states of cis-3-aminophenol and trans-3-aminophenol are calculated as a function of the electric field strength. Figure 7.13 shows the resulting Stark curves for the lowest rotational states of both species. The transmission characteristics of the selector depend on μ_{eff} (the negative of the slope of the Stark curve, see Equation 2.33), the electric field gradients, and the AC frequency. Similar to the frequency dependence in quadrupole mass filters, molecules with a given value of μ_{eff} are only transmitted through the selector within a finite range of frequencies. At too low frequencies the molecules are deflected and lost in one transverse dimension before they are refocused. For high frequencies the time-averaged potential becomes flat resulting in a strongly

[§]Based on: Selector for structural isomers of neutral molecules, F. Filsinger, U. Erlekam, G. von Helden, J. Küpper, and G. Meijer, *Phys. Rev. Lett.* **100**, 133003 (2008)

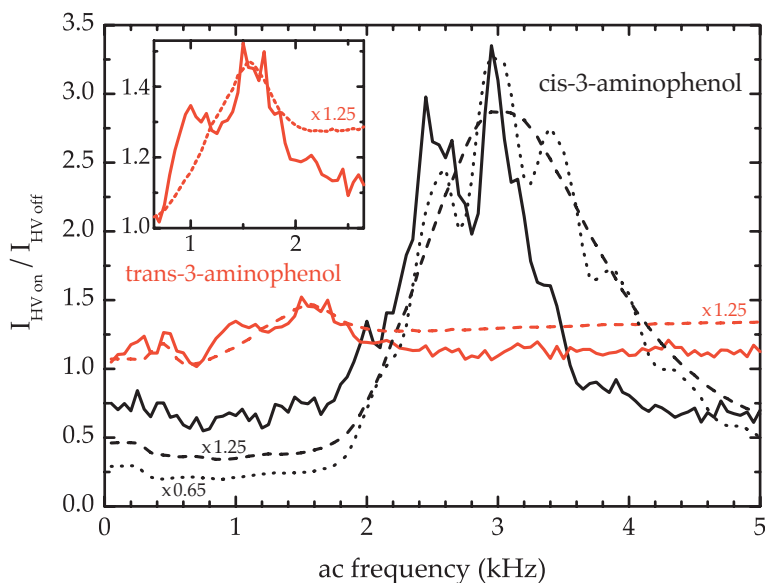


Figure 7.14: Experimental (solid lines) and simulated (dashed lines) transmission as a function of the AC frequency for cis-3-aminophenol (black) and trans-3-aminophenol (red). The inset shows an enlarged view of the transmission curve of trans-3-aminophenol. The black dotted line represents simulations for cis-3-aminophenol that include the overlap between detection laser and the molecular beam (see Figure 7.9).

reduced transmission, as discussed in the previous section for ammonia. The AC frequency for optimal transmission increases with increasing μ_{eff} . When a constant AC frequency is applied, a μ_{eff} selection – and thus a conformer selection – is performed.

AC frequency scans for cis-3-aminophenol and trans-3-aminophenol are shown in Figure 7.14. The transmission measurements are performed with the excitation laser frequency set close to the band origin of the respective conformer. The AC frequency is scanned from 0 kHz to 5 kHz in steps of 50 Hz. For a given conformer, the number of transmitted molecules is measured with and without applied high voltages, and the ratio of these two measurements is plotted in Figure 7.14. As shown in the experiments on ammonia in Section 7.3, the start phase of the switching cycle determines the overall transmission of the selector. In all measurements presented here, the switching cycle starts with a half-period of focusing along the horizontal x -axis. As a consequence, the phase of the switching cycle at the moment that the molecules exit the selector changes with the applied frequency. For cis-3-aminophenol a clear enhancement of

the transmission is observed for AC frequencies in the range from 2–3.5 kHz, whereas for trans-3-aminophenol a weaker transmission maximum is observed around 1.5 kHz. Both, the higher frequency and the higher transmission for cis-3-aminophenol reflect its considerably larger dipole moment compared to that of the trans conformer. The central dip in the transmission curve at 2.7 kHz is due to effects of the exact phase of the AC switching cycle at the exit of the selector. As discussed for ammonia, this phase determines the shape of the molecular packet in the detection region, and thereby its overlap with the laser beams. Compared to the transmission curves of ammonia (Figure 7.8), the effect of the changing end phase is less pronounced for 3-aminophenol, because unfocused laser beams are used to detect 3-aminophenol and a larger fraction of the transmitted molecular packet is probed.

Monte Carlo trajectory calculations (see Section 3.6 for details) are performed to simulate the transmission curves for fixed excitation laser frequencies. For this, the rotationally resolved electronic excitation spectrum is calculated using the known rotational constants and transition moment orientations [87, 176]. A rotational temperature of 4 K yields a rotational envelope that agrees best with the observations (*vide infra*). A rectangular spectral profile of the laser with a width of 0.15 cm^{-1} is assumed. For all rotational states that are probed within this bandwidth of the laser, Monte Carlo simulations are performed, and individual transmission curves are calculated. From the calculated line strengths and populations, a weight for every single quantum state is determined. The weighted sum over the individual transmission curves is shown together with the experimental data in Figure 7.14 (dashed lines). These simulations nicely reproduce the peak position and the low-frequency cutoff of the experimental transmission curves. On the high-frequency side the experimentally observed transmission decreases faster than predicted, which is attributed to mechanical misalignment. Taking into account the phase-dependent shape of the molecular packet and its spatial overlap with the detection laser beams, the observed modulation of the transmission peak for cis-3-aminophenol is correctly reproduced (dotted line).

The transmission of the selector depends on the effective dipole moment of the individual quantum states. Whereas in the experiments on ammonia presented in Section 7.3 individual rotational quantum states could be resolved with the pulsed dye laser, its bandwidth is too large to achieve rotational resolution for 3-aminophenol. Although individual rotational states cannot be detected, there is a well-defined relation between the excitation laser frequency and the rotational states that are probed. In Figure 7.15 the (1+1')-REMPI spectrum of 3-aminophenol is shown. In the center of each of the vibronic bands, predominantly transitions from low- J states are probed, whereas the wings of the rotational envelopes contain mostly transitions from high- J states. The inset of Figure 7.15 shows the rotational contour of the origin transition

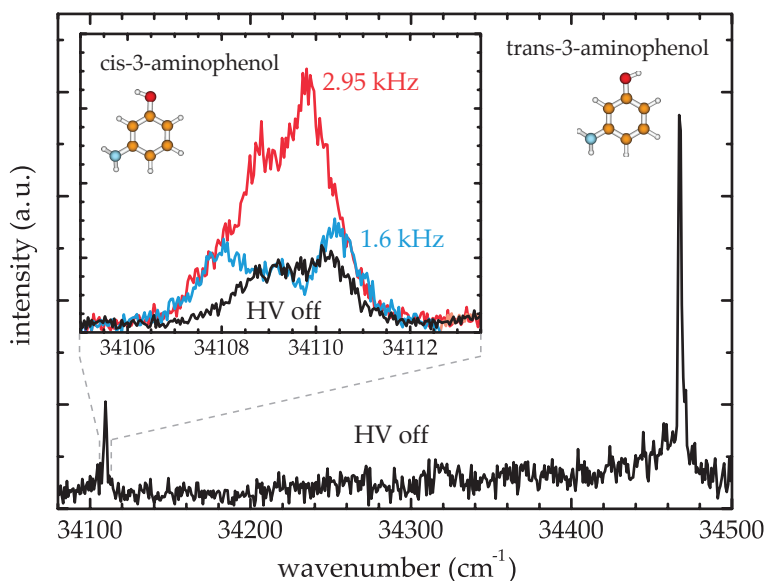


Figure 7.15: $(1+1')$ -REMPI spectrum of 3-aminophenol. The spectrum is measured without high voltage applied to the selector, and shows the two origin transitions. In the inset, the rotational envelope of the cis-3-aminophenol origin transition is shown without high voltage (black) and with high voltage for AC frequencies of 2.95 kHz (red) and 1.6 kHz (blue).

of cis-3-aminophenol on an enlarged wavenumber scale measured with and without electric fields, for different ac frequencies. For a frequency of 1.6 kHz the wings of the rotational envelope are increased, whereas the intensity of the central part of the band is actually decreased. This directly reflects that for this AC frequency high- J states are efficiently transported through the selector, whereas low- J states, that generally have a larger μ_{eff} , are over-focused and have a lower transmission. For a frequency of 2.95 kHz the whole rotational envelope is clearly increased. The largest enhancement is now observed for the central part of the rotational envelope, where mostly low- J states are probed. Figure 7.16 compares the changes of the rotational envelope upon focusing for both conformers. In order to visualize the relative changes in the intensity, both the spectral lines are scaled such that the peak intensities are identical for both conformers. Much weaker changes in the rotational envelope are observed for the trans conformer due to its smaller dipole moment, in agreement with the conclusions drawn from the transmission curves, which are shown in Figure 7.14. However, the changes in the relative abundance of the conformers would be slightly overestimated, when only considering the transmission curves. These curves are measured at the wavenumbers indicated by grey bars

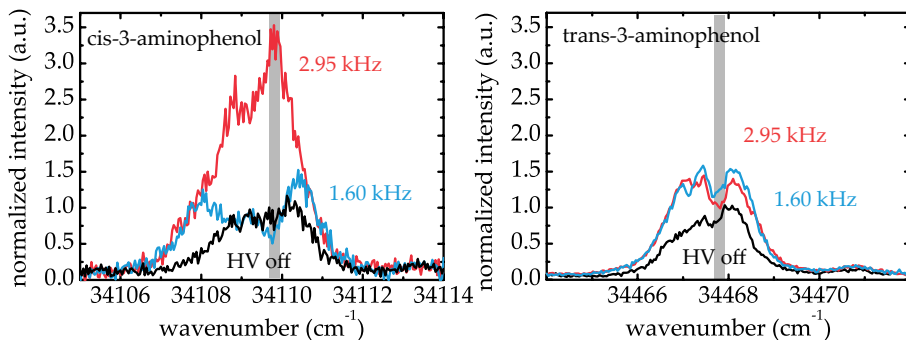


Figure 7.16: $(1+1')$ -REMPI spectrum of 3-aminophenol. The rotational envelopes of the cis-3-aminophenol origin transition (left) and trans-3-aminophenol origin transition (right) are scaled to the same peak intensities for the free jet. Experiments are performed without high voltage (black) and with high voltage for AC frequencies of 2.95 kHz (red) and 1.6 kHz (blue). The unscaled relative peak intensities are shown in Figure 7.15.

in Figure 7.16 and sample only a fraction of the populated rotational quantum states. Instead, the integrated intensities over the rotational envelopes for cis-3-aminophenol $I_{\text{int,cis}}$ and trans-3-aminophenol $I_{\text{int,trans}}$ are calculated and employed to estimate the changes of the populations. Without the selector $I_{\text{int,cis}}/I_{\text{int,trans}} = 0.28$. When the selector is operated at 1.6 kHz, $I_{\text{int,cis}}/I_{\text{int,trans}}$ decreases to 0.23, whereas $I_{\text{int,cis}}/I_{\text{int,trans}} = 0.43$ at an AC frequency of 2.95 kHz. These values indicate, that the relative abundance of the conformers can be changed by approximately a factor of 2 in the present setup.[¶] From Figure 7.16 it is evident, that intensity in the wings of the rotational envelope is rather independent from the applied frequency and that the population of high- J quantum states limits the conformer separation that can be achieved. This limitation could be reduced if a lower initial rotational temperature could be achieved. Of course, the separation would also work better for species with higher dipole moments.

In the experiments presented here, the selector is operated under conditions for optimal transmission, equivalent to the “RF-only” operation mode of quadrupole mass filters. The resolution $\mu_{\text{eff}}/\Delta\mu_{\text{eff}}$ of the selector is only about two in this case. In m/q filters, the resolution $m/\Delta m$ is increased by adding a DC offset to the RF potentials, at the cost of a reduced transmission. In the m/μ -selector a better resolution can be achieved by adding a static defocusing field to the two configurations of the electric field that is used here. As

[¶]Note that these numbers are only a crude estimate and might not reflect the actual changes in the populations, because, for instance, saturation effects and rotational quantum state specific detection efficiencies are not taken into account here.

described in Section 3.5, this can be achieved by using different high voltages for the two electric field configurations or, more easily, by changing the duty cycle, i. e., by applying the presently used field configurations for different time-intervals. The latter approach is experimentally demonstrated in the following section. For many biomolecules, e. g., amino acids and peptides, the various conformers have large and widely different dipole moments. For phenylalanine, for instance, at least six conformers have been observed [83, 84] and their dipole moments are calculated to range from 1 D to 5.5 D. Therefore, the partial selection of its conformers would be feasible even at the present resolution.

7.5 Improving selectivity – changing the duty cycle

In order to demonstrate the effect of the duty cycle, experiments on ABN are performed. ABN is chosen because it has a very favorable m/μ -ratio for AG focusing (mass 118 u, $\mu = 6.51$ D) and possesses, in contrast to small molecules like ammonia, a high density of rotational states. This high density of states is typical for large molecules and an important characteristic when the potential of the m/μ -selector is to be estimated. Due to the high density of states, many high- J states that generally have a small μ_{eff} are populated even at the low temperatures in a molecular beam. This may cause unwanted background signal, similar to what is observed for 3-aminophenol (*vide supra*), and reduce the contrast in selection experiments. As discussed in Section 3.5, for $d \neq 0.50$ (for the definition of d see Figure 3.4) the range of frequencies for which AG focusing works is expected to decrease at the cost of overall transmission. In order to experimentally demonstrate this, it is important to measure the envelope function of the transmission curve independent from strong modulations caused by a changing start or end phase. For molecules with a linear Stark effect at the relevant field strengths (for example ammonia molecules in the polar components of the $J_K = 1_1$ state) the envelope of the transmission curve can be visualized by measuring the transmission as a function of the AC frequency for different high voltages (see Figure 7.8). This approach is suboptimal for larger molecules, because, for these systems, many rotational states with a μ_{eff} that strongly varies with the electric field strength are populated. Changing the voltage will thus have a substantial non-linear effect on the effective focusing potential. As a consequence, the AC frequency cannot simply be scaled to obtain a reduced frequency, as it is possible for ammonia, and a different approach to measure the envelope of the transmission curve is taken here. The pronounced dips observed in the transmission curves for 3-aminophenol and ammonia are caused by a bad overlap between the molecular packet and the detection laser for the best start phase. Because the selector is tilted with respect to the molecular beam axis in these experiments, only one optimal start phase exists. For the experiments on ABN the selector is aligned parallel to the

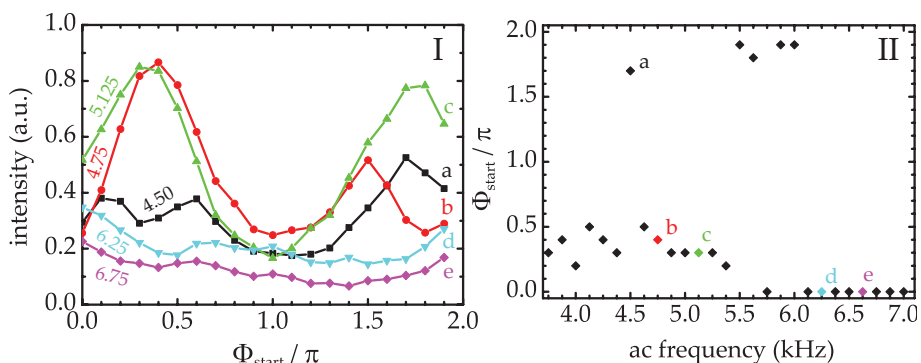


Figure 7.17: Left: Transmission of ABN as a function of the start phase of the switching sequence for different AC frequencies as indicated in the figure. Right: Optimal start phase as a function of the AC frequency for a duty cycle of 0.50.

molecular beam axis, in which case – at least in theory – two equally good start phases exist. The start phase can then be chosen such that detrimental effects due to the changing end phase are minimized.

In order to experimentally determine the optimal start phase, the transmission of ABN through the selector is measured as a function of Φ_{start} at a constant AC frequency. Figure 7.17I shows such phase scans for $d = 0.50$. For $\nu = 5.125$ kHz two peaks of the transmission are observed at $\Phi_{\text{start}} = 0.3\pi$ and $\Phi_{\text{start}} = 1.75\pi$, with a somewhat higher transmission at $\Phi_{\text{start}} = 0.3\pi$. The optimal start phase of initial x -focusing is slightly longer and the optimal start phase of initial y -focusing is slightly shorter than theoretically expected, but qualitatively this phase dependence agrees with the simulations (see simulations for ammonia, Figure 7.11). When the frequency is decreased to 4.75 kHz, a dip in the peak of the transmission at $\Phi_{\text{start}} = 1.75\pi$ is observed that is attributed to a suboptimal overlap between the detection laser and the molecular packet for the resulting end phase. Similarly, for $\nu = 4.50$ kHz a dip in the transmission peak at $\Phi_{\text{start}} = 0.3\pi$ is observed giving rise to the highest transmission when initially starting with y -focusing. In the phase scans for $\nu = 6.25$ kHz and $\nu = 6.75$ kHz only one peak of the transmission is observed at $\Phi_{\text{start}} = 0$. This start phase is found to be optimal for all frequencies above 6 kHz, as shown in Figure 7.17 II. For $\nu \lesssim 5.5$ kHz the optimal start phases are between 0.2π and 0.5π and, generally, starting with x -focusing yields a slightly higher transmission than starting with y -focusing. This might indicate that the selector is not perfectly aligned and still slightly tilted in y -direction. The effect could also be caused by misalignment of the electrodes favoring the initial focusing along x . Because the optimal start phases found in the experiment deviate

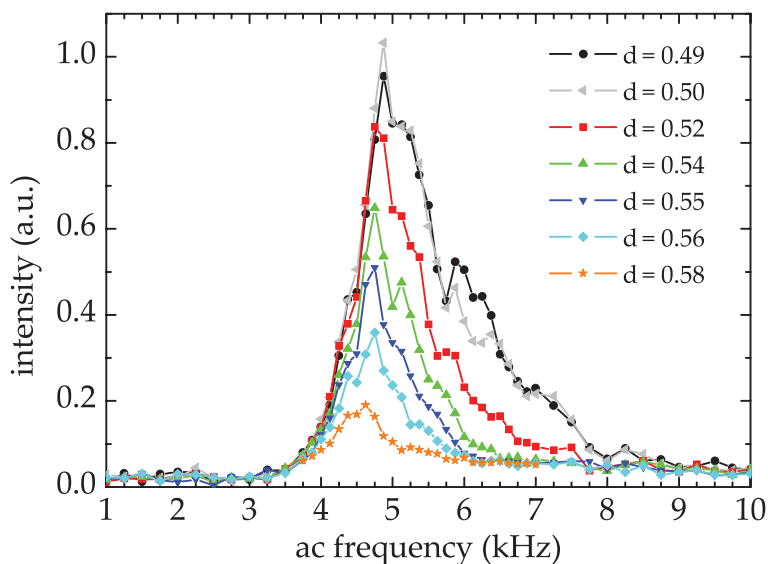


Figure 7.18: Transmission of p-aminobenzonitrile for $d \geq 0.49$ as a function of the AC frequency measured with optimized start phases; see text for details.

from the values obtained from the simulations, the optimization procedure is repeated for various frequencies and $d \neq 0.50$.

The transmission of ABN for $d \geq 0.49$ is measured as a function of the AC frequency with the optimized start phases and plotted in Figure 7.18. Compared to the transmission curves for ammonia (Figure 7.8) and 3-aminophenol (Figure 7.14) the modulations caused by the changing overlap of the molecular packet with the detection laser are much weaker and the envelope of the transmission curve is clearly visible. Furthermore, while for 3-aminophenol a background signal caused by unpolar quantum states is observed, for ABN the transmission on both, the low and the high, frequency sides of the maximum is very low. This improved contrast of the transmission curve can be explained by the larger dipole moment of ABN compared to 3-aminophenol and the corresponding larger force the molecule experiences. Furthermore, in the experiments on ABN the rotational temperature is approximately 1 K^{||} and considerably lower than in the experiments on 3-aminophenol, where it was determined to be 4 K. This lower rotational temperature significantly reduces the number of unpolar quantum states that are populated. The transmission curves for $d = 0.49$ and $d = 0.50$ are comparable both in width and peak

^{||}The rotational temperature is not directly determined. However, for 3-aminophenol, iodobenzene, and benzonitrile a rotational temperature of 1 K is observed under very similar expansion conditions, see Chapter 5.

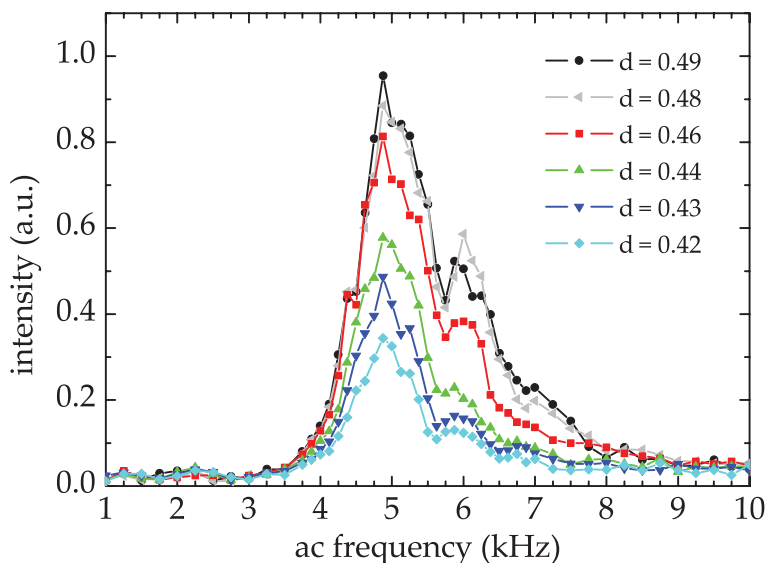


Figure 7.19: Transmission of p-aminobenzonitrile for $d \leq 0.49$ as a function of the AC frequency measured with optimized start phases; see text for details.

intensity. As the duty cycle is increased, the peak intensities and the width of the transmission curves both decrease, where the decrease in intensity is the largest at the high-frequency side of the maximum. While the high-frequency cut-off clearly shifts to smaller frequencies with increasing duty cycle, the peak position and the low-frequency cut-off occur approximately at the same position for all duty cycles. It is concluded, that the separation of ABN from a second species with different m/μ -ratio would be clearly improved when operating the selector at $d \neq 0.50$.

The measurements are repeated for $d < 0.49$ and shown in Figure 7.19. The same trend is found as for $d > 0.49$. With increasing asymmetry of the switching sequence the width and the peak intensity of the transmission curve both decrease. Figure 7.20 a directly compares the transmission curves for $d > 0.49$ (filled symbols) with the transmission curves obtained for $d < 0.49$ (open symbols). Apart from small deviations, the shape of the transmission curve for $d = 0.54$ corresponds to the curve for $d = 0.44$. Similarly, the transmission curve obtained for $d = 0.56$ resembles the one for $d = 0.42$. Figure 7.20 a indicates that the transmission characteristics of the selector are symmetric with respect to $d = 0.49$ rather than to $d = 0.50$, as it is theoretically expected (see Section 3.5). This deviation is attributed to misalignment of the electrodes.

Monte Carlo simulations are performed to simulate the experimental trans-

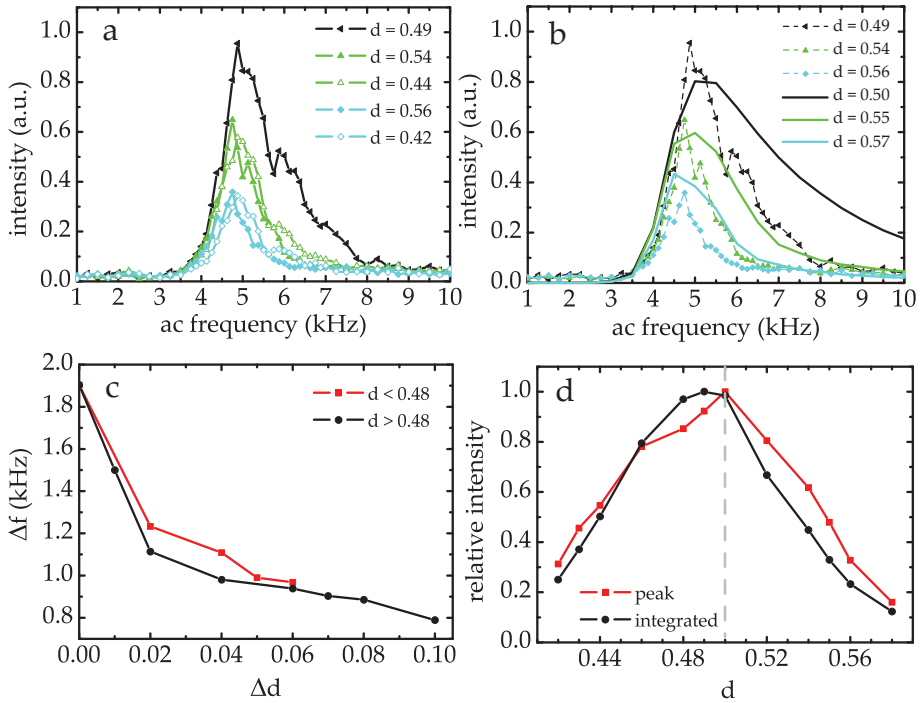


Figure 7.20: (a) Comparison of transmission curves obtained for $d < 0.49$ with the curves for $d > 0.49$. (b) Comparison of experimental transmission curves (dashed lines plus symbols) with simulated transmission curves (solid lines) for an ensemble with $T_{\text{rot}} = 0.7$ K. The duty cycle for each curve is given in the inset. The experimental transmission curves are symmetric with respect to $d = 0.49$, whereas the simulated transmission curves are symmetric with respect to $d = 0.50$. All simulations have been scaled by a factor of 0.37. (c) Width (FWHM) Δf of the transmission curve as a function of the change of duty cycle $\Delta d = |0.48 - d|$. (d) Peak intensity and integrated intensity of the transmission curve as a function of d . The grey dashed line indicates the theoretically expected maximum at $d = 0.50$

mission curves and shown as solid lines together with the experimental data in Figure 7.20 b. The simulations nicely reproduce the low frequency cut-off and the peak positions of the transmission curves. Assuming that the simulations are symmetric with respect to $d = 0.50$, whereas the experiments are symmetric with respect to $d = 0.49$, also the relative peak intensities for the different duty cycles can be reproduced. However, similar to the results for 3-aminophenol and ammonia, the simulations overestimate the intensities at the high frequency side of the maximum and, thereby, the widths of the transmission curves. While this discrepancy between experiment and simulation hinders a quantitative comparison of the widths, qualitatively a very similar behavior upon changing the duty cycle is found. For the simulations that are shown in Figure 7.20 b the lowest 400 $J_{K_a K_c} M$ -quantum states are included and a rotational temperature of 0.7 K is assumed. This temperature is somewhat lower than in the experiments under comparable conditions presented in Chapter 5, but not unrealistic given that the lowest literature value of the rotational temperature for similar expansion conditions is 0.4 K (aniline seeded in He [160]). An accurate determination of the rotational temperature by comparison of simulated and experimental transmission curve is difficult because the differences in the shapes are relatively large. However, the position of the low-frequency cut-off is quite sensitive to changes of the rotational temperature and comparing simulations and experiment suggests that $T_{\text{rot}} \lesssim 1$ K.

In order to characterize the properties of the selector in more detail, the FWHM of the transmission curves are calculated. As shown in Figure 7.20 c, the widths of the transmission curves are symmetric with respect to $d = 0.48$. However, one has to be careful in the determination of the width of the transmission curve, since remaining phase effects influence its value. Note that the transmission curves for $d = 0.50$, $d = 0.49$, and $d = 0.48$ look very similar, even though the FWHM differs between them (compare Figures 7.18 and 7.19). Despite the possibly inaccurate determination of the exact value of the FWHM, the width of the transmission curve decreases from approximately 1.9 kHz at $d = 0.48$ to 0.8 kHz at $d = 0.58$, clearly demonstrating the improved resolution of the selector that is obtained upon changing the duty cycle. Finally, the peak intensities and the integrated intensities of the transmission curves are plotted as a function of the duty cycle in Figure 7.20 b. While the highest peak intensity is observed for $d = 0.50$ and $\nu = 4.875$ kHz, the highest integrated intensity is obtained for $d = 0.49$. Taking all criteria, namely shape, width, and intensities of the transmission curves into account, it is concluded, that $d = 0.49$ represents the "optimal" duty cycle for the present setup. Table 7.1 summarizes the characteristics of the transmission curves for the different duty cycles.

d	Δv (kHz)	Δv^{rel}	$I_{\text{peak}}^{\text{rel}}$	$I_{\text{int}}^{\text{rel}}$	ν_{peak} (kHz)
0.42	0.97	0.51	0.31	0.25	4.875
0.43	0.99	0.52	0.46	0.37	4.875
0.44	1.11	0.58	0.55	0.50	4.875
0.46	1.23	0.65	0.78	0.79	4.875
0.48	1.90	1.00	0.85	0.97	4.875
0.49	1.50	0.79	0.92	1.00	4.875
0.50	1.11	0.59	1.00	0.98	4.875
0.52	0.98	0.52	0.81	0.67	4.750
0.54	0.94	0.49	0.62	0.45	4.750
0.55	0.90	0.47	0.48	0.33	4.750
0.56	0.89	0.47	0.33	0.23	4.750
0.58	0.79	0.41	0.16	0.12	4.750

Table 7.1: Widths (FWHM) Δf , relative widths Δf^{rel} , relative peak intensities $I_{\text{peak}}^{\text{rel}}$, relative integrated intensities $I_{\text{int}}^{\text{rel}}$, and AC frequencies for maximum intensity ν_{peak} , of transmission curves for different duty cycles.

7.6 Summary

In this chapter, the implementation of a novel m/μ -selector for neutral molecules is described. The device is first characterized by experiments on ammonia in its $J_K = 1_1$ state. These measurements demonstrate the versatility of the device. Clear evidence of dynamic focusing is obtained for both lfs and hfs states and differences in the frequency dependence of the transmission are observed. At high frequencies the transmission of the lfs component does practically not decrease, and the low-frequency onset of its transmission curve is shifted towards higher frequencies compared to the hfs state. This demonstrates the quantum state dependence of the focusing process and that, at least in principle, one could use the selector to separate the two quantum states. Moreover, since focusing and defocusing directions are interchanged between the lfs and hfs states, the phase effects shown in Figure 7.9 are shifted by π , which can also be used to discriminate between the two states using focused lasers or by narrow slits in the beam path. The detailed investigation of the AG focusing using a small molecule that can be detected with rotational resolution provides essential information for the experiments on more complex systems, i. e., larger molecules with multiple conformers and a high density of rotational states such as 3-aminophenol. The cis and trans conformers of 3-aminophenol have different dipole moments and, therefore, distinct frequency dependent transmission characteristics, which is exploited here to select and separate them. The dynamic focusing works best for the states with the largest effective dipole moments, which are the lowest rotational states. Here, molecular packets with an excess of cis-3-aminophenol in low rotational states are created at an

AC frequency of 2.95 kHz. Such conformer-selected molecular packets offer interesting perspectives for a variety of experiments. Since the selected states are the most polar ones, these samples are particularly useful for experiments in which aligned or oriented molecules are desired. The degree of separation between the conformers that can be achieved in the present setup is limited by the background caused by unpolar quantum states due to the relatively high rotational temperature (4 K) and by the resolution of the selector. The former can be optimized by employing an Even-Lavie valve operating at high backing pressure, while the latter can be improved by operating the device at $d \neq 0.50$ (or in practice at $d \neq 0.49$), as confirmed by the experiments on ABN. Even though the molecules spend only approximately 1 ms inside the selector and typically experience only five switching cycles at frequencies around 5 kHz, the effect of the duty cycle is clearly demonstrated and the width of the transmission curve is reduced by more than a factor of two. Monte Carlo simulations are employed to support the experimental data and, generally, a good agreement between experiment and simulation is obtained. While the peak position and the low frequency cut-off of the transmission curves are nicely reproduced, the transmission at high switching frequencies is overestimated in all simulations. This discrepancy is attributed to misalignment of the electrodes, which is not included in the simulations but known to be substantial. At high AC frequencies the confining potential becomes shallow and trajectories that are stable for a perfect geometry might more easily be destabilized than near the maximum, where the potential is deep. It should be noted that in a similar experiment it was concluded, that misalignment of the electrodes affects in particular the low frequency cut-off of the transmission curve [58], which to some degree contradicts the simulation results presented here. In order to clarify this issue, in future work misalignment of the electrodes should be included in the simulations.

Chapter 8

Outlook

In the framework of this thesis, new techniques have been developed for the quantum-state- and conformer-selective manipulation of large polar molecules with electric fields. Using an electrostatic deflector, quantum-state-selected targets of polar molecules are prepared that are expected to be beneficial for a variety of experiments. As an example of this, unprecedented degrees of laser-induced adiabatic alignment and mixed-field orientation of deflected iodobenzene molecules are demonstrated in Chapter 5. In the same setup, the quantum-state selectivity of the deflection process is exploited to spatially isolate the *cis* and *trans* conformers of 3-aminophenol, as shown in Chapter 6. Clean samples of both conformers are obtained that are also separated from the atomic seed gas. A complementary approach for conformer selection is demonstrated in Chapter 7, where the implementation of a dynamic m/μ -selector is described. Using the selector, the relative abundance of 3-aminophenol conformers is clearly changed and quantum-state-specific focusing effects are observed in the REMPI spectrum. However, it is not possible to obtain clean samples consisting of only one conformer in the present selector setup. This chapter addresses the question how the next generation dynamic conformer selector should look like. For this purpose, Monte Carlo simulations are presented in Section 8.1 that compare deflection and focusing experiments, as well as different electrode geometries. Finally, possible further applications of quantum-state- and conformer-selected molecules are outlined in Section 8.2

8.1 The next generation μ/m -selector

In the conformer selection experiments presented in Section 7.4, the limited contrast is attributed to a large extent to the relatively high rotational temperature of ~ 4 K that was present in the beam with the valve employed there (General Valve Series 9). A considerably lower temperature of 1 K can be

routinely achieved with an Even-Lavie valve (see Chapter 5). However, the onset of clustering prevented us from using heavy seed gases with this valve. Low rotational temperatures could basically only be achieved when He or Ne were used as the carrier gas. For an expansion in Ne and a valve temperature of $\sim 100^\circ\text{C}$ the typical forward velocity is about 900 m/s at a speed ratio* of 100 [177], and all simulations presented in this chapter are done for such a beam. In all simulations, identical initial beams are used with a transverse velocity spread of 15 m/s (FWHM).

Figure 8.1 shows simulations for different selector geometries for three different hypothetical molecules with a mass of 100 u and constant effective dipole moments of $0.02\text{ cm}^{-1}/(\text{kV cm}^{-1})$ (denoted hereafter as species II), $0.04\text{ cm}^{-1}/(\text{kV cm}^{-1})$ (denoted as species IV) and $0.07\text{ cm}^{-1}/(\text{kV cm}^{-1})$ (species VII)[†]. A 4 mm diameter skimmer is placed 14 cm downstream from the valve and 6 cm from the entrance of the selector. Figures A1-A4 show the transmission, i. e. , the number of molecules reaching the detection region divided by the number of molecules passing the skimmer, as a function of the AC frequency for $d = 0.50$ (dashed lines) and $d = 0.58$ (solid lines). Figures B1-B4 show the fractional intensity, which is obtained by dividing the transmission curve of a given species by the sum of the transmission curves for all species, for $d = 0.58$. In the present setup (Figures A1 and B1), only species I can be completely isolated for an expansion in neon. Due to the small number of switching cycles, many molecules still reach the detection area on metastable trajectories, in particular at the high frequency side of the transmission peak for species I, which has the smallest effective dipole moment. Doubling the number of switching cycles by increasing the length of the selector and operating the selector at $d = 0.58$ significantly reduces the long "tails" of the transmission curves. The improved contrast is clearly seen in Figure B2. For a 2 m-long selector with the same cross section, samples of each of the artificial species can be obtained with a purity $\geq 98\%$. However, as discussed in Chapter 7, significant misalignment of the electrodes is already observed for the current 1 m-long selector. For a slightly bigger focuser with electrodes of 3 mm radius similar problems have been reported [58], and these problems are expected to increase for a longer selector. However, enlarging the radius of the electrodes further should eventually result in a mechanically more stable device and reduce the misalignment. Figures A3 (A4) and B3 (B4) show simulations for a 3 m-long electrode geometry with the transverse cross section scaled up (compared to the present setup) by a factor of 2 (3). High voltages of ± 20 (30) kV are applied to the electrodes resulting in a maximum field strength of 227 kV/cm

*The speed ratio is given by $v/\Delta v$, where v denotes the velocity and Δv is the FWHM of the velocity distribution.

[†]These values correspond to 1.2 D, 2.4 D, and 4.2 D. Note that for real molecules the effective dipole moment corresponds to the permanent dipole moment only in the limit of infinitely high electric fields; see Chapter 2 for details.

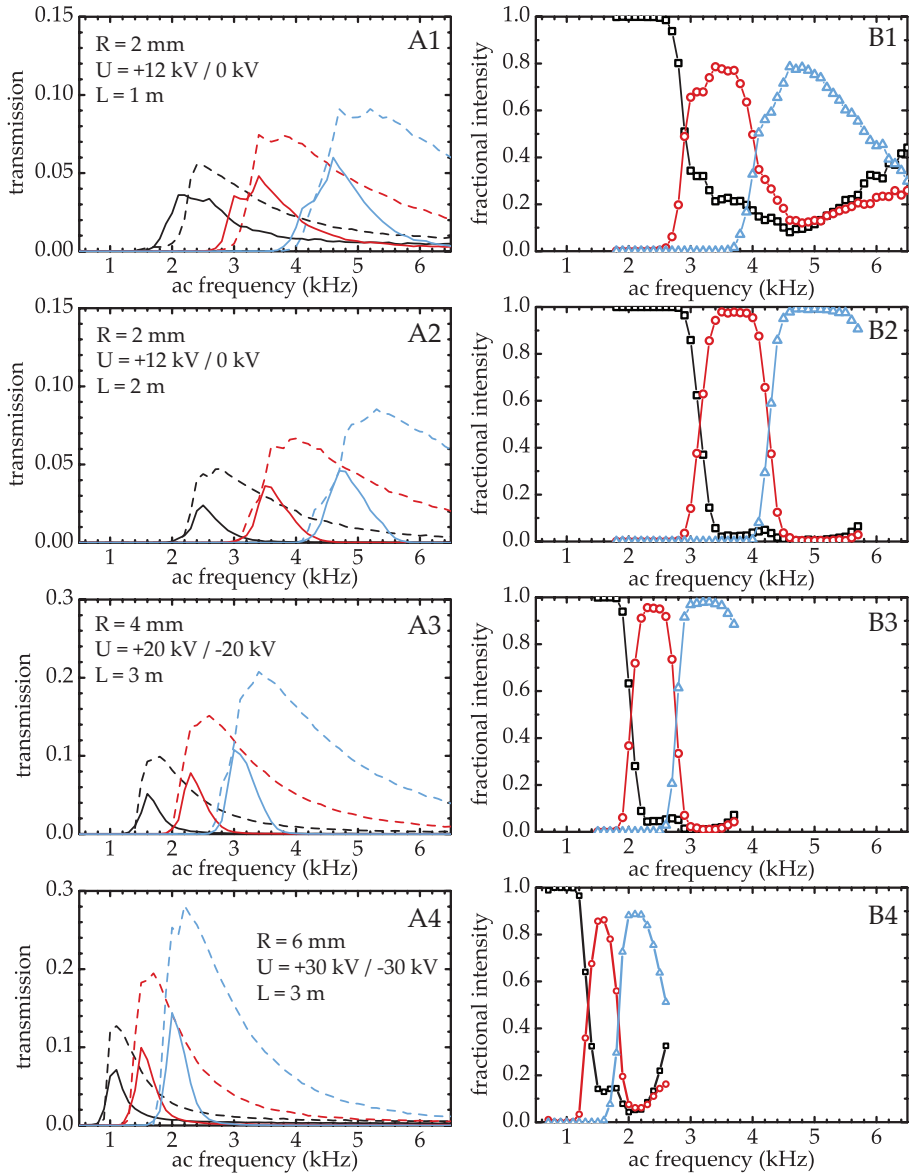


Figure 8.1: Simulations for species with $m = 100$ u and constant effective dipole moments of $0.02 \text{ cm}^{-1}/(\text{kV cm}^{-1})$ (black), $0.04 \text{ cm}^{-1}/(\text{kV cm}^{-1})$ (red), and $0.07 \text{ cm}^{-1}/(\text{kV cm}^{-1})$ (blue). Left: Transmission through the selector as a function of the AC frequency for $d = 0.50$ (dashed lines) and $d = 0.58$ (solid lines). Right: Fractional intensities of individual species for $d = 0.58$ as a function of the AC frequency. Radius R , voltages U , and length L of the selector are given in the inset; see text for details.

at the surfaces of the electrodes, which are demanding but feasible experimental conditions. If the transverse dimension of the electrode geometry is scaled up by a factor s and the voltage differences applied to the electrodes are scaled by a factor δ , then the electric field gradients scale as $\delta \cdot s^{-2}$. Since δ cannot be arbitrarily increased for technical reasons, the field gradients eventually decrease with increasing electrode cross section. This reduction manifests itself in a shift of the transmission peaks towards lower AC frequencies (compare Figures A2, A3, and A4). As a consequence, the length of the selector has to be increased for larger electrode radii, in order to achieve a selectivity that is comparable to that of the selector with the $R = 2$ mm electrodes. As shown in Figure B3, samples of species II, IV, and VII all with a purity of $\geq 95\%$ are expected for a 3 m-long selector with $R = 4$ mm. For $R = 6$ mm, however, only species I can be isolated with a fractional intensity $\geq 90\%$ (see Figure B4).[‡]

Changing the size of the electrode structure also changes the maximum transmission through the selector. When the radius of the electrodes is increased from $R = 2$ mm to $R = 4$ mm, the peak transmission increases by more than a factor of two due to the increased phase-space acceptance of the larger selector. When increasing the radius further from $R = 4$ mm to $R = 6$ mm, the transmission rises by another 40%. Note that one has to be cautious when directly comparing the transmission in the different simulations. First of all, for pulsed-laser detection schemes, not the transmission but the number density (i. e., the number of molecules per volume) in the molecular beam is the relevant quantity, and the number density decreases with increasing length of the selector. However, since the selector focuses the molecular packet in x and y , this decrease is only caused by spreading of the molecules along z once all particles on metastable trajectories are removed from the beam. Due to the large speed ratio for the Even-Lavie valve (*vide supra*) this reduction of beam density is expected to be relatively small. Secondly, for the larger devices, misalignment of the electrodes is expected to be much smaller. Since such misalignment significantly reduces the efficiency of AG focusing [58, 68, 71], the increase of the transmission upon scaling up the selector is probably underestimated in the simulations shown in Figure 8.1. Summarizing the simulation results obtained so far, a 3 m-long selector with electrodes of 4 mm radius operated at ± 20 kV appears to be a good compromise between maximum field gradients on the one hand and a mechanically stable construction with maximum transmission on the other hand.

[‡]Simulations were also performed for two slightly different electrode geometries with $R = 6$ mm electrodes, both operated at ± 30 kV. The geometry proposed by Bethlem et al. [68] and the one implemented by Wall et al. [58] both resulted in peak transmissions that are comparable to the transmission in Figure 8.1 A4. However, the field gradients and, therefore, the optimal AC frequencies are somewhat smaller compared to the selector implemented here, resulting in a slightly inferior degree of separation.

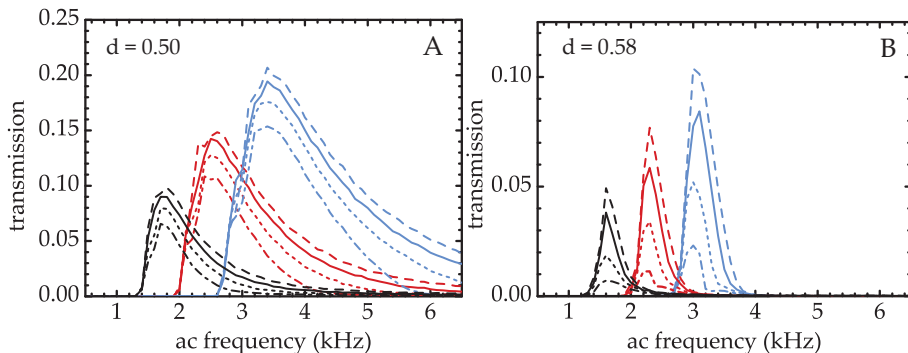


Figure 8.2: Simulations for hypothetical molecules with $m = 100$ u and constant effective dipole moments of $0.02 \text{ cm}^{-1} / (\text{kV cm}^{-1})$ (black), $0.04 \text{ cm}^{-1} / (\text{kV cm}^{-1})$ (red), and $0.07 \text{ cm}^{-1} / (\text{kV cm}^{-1})$ (blue). The transmission through a 3 m-long selector with electrodes of 4 mm radius and high voltages of ± 20 kV is plotted as a function of the AC frequency for $d = 0.50$ (left) and $d = 0.58$ (right). Simulations are performed for an expansion in Ne ($v = 900$ m/s) and a selector that is parallel to the molecular beam axis (dashed lines), tilted in both x and y by 2 mm/m (solid lines), 3 mm/m (dotted lines), and 4 mm/m (dash-dotted lines).

One big advantage of the static deflector is that it intrinsically separates the polar molecules from the unpolar atomic seed gas. A similar separation for the focused molecular packet can be achieved by tilting the axis of the selector with respect to the incoming molecular beam. Figure 8.2 shows simulations for different tilt angles for a 3 m-long selector, electrodes with $R = 4$ mm, and high voltages of ± 20 kV. In order to completely block the line-of-sight and, thereby, to eliminate any direct background from the carrier gas, a moderate tilt of 2 mm/m (or 0.1°) in both x and y is sufficient. This tilt reduces the peak transmission for a duty cycle of 0.50 by less than 10% (see Figure 8.2 A, solid line). For $d = 0.58$, shown in Figure 8.2 B, the loss in peak intensity of 20% is somewhat larger but still acceptable. Tilting the selector even further away from the molecular beam axis has a similar effect on the transmission curves as changing the duty cycle. As shown in Figure 8.2 A for $d = 0.50$, the transmission at the high-frequency side of the maximum is reduced more than the transmission at the low-frequency cut-off, which increases the resolution of the selector. The analogy between changing the duty cycle and tilting the selector is not surprising because both operations decrease the depth of the effective focusing potential. However, a symmetric tilt in x and y lowers the trap depth symmetrically in both transverse directions, whereas the alteration of the focusing potential is asymmetric in x and y for a change of the duty cycle. For

$d = 0.58$ similar effects as for $d = 0.50$ are observed upon tilting the selector that are, however, accompanied by a much stronger loss of transmission. Whereas doubling the amplitude of the tilt induces a reduction in the peak transmission by 25% for $d = 0.50$, the corresponding peak transmission is five times lower for $d = 0.58$. In conclusion, the simulations shown in Figure 8.2 demonstrate that focused packets of polar molecules that are well-separated from unpolar background species can be obtained with a tilted selector without losing much signal compared to the case when the selector is aligned parallel to the beam axis.

In order to address the question, whether a static deflector or an optimized dynamic focuser yields a better m/μ -selection, simulations are performed for seven species with a mass of 100 u and effective dipole moments ranging from $0.01 \text{ cm}^{-1}/(\text{kV cm}^{-1})$ to $0.07 \text{ cm}^{-1}/(\text{kV cm}^{-1})$ in steps of $0.01 \text{ cm}^{-1}/(\text{kV cm}^{-1})$, which are denoted as species I, species II, . . . , species VII. Figure 8.3 compares the selectivity achieved with a 3 m-long selector ($R = 4 \text{ mm}$, $d = 0.58$, operated at $\pm 20 \text{ kV}$ and tilted by 2 mm/m along x and y) with the selectivity obtained with the deflection setup that was used for the experiments described in Chapters 5 and 6. At frequencies below 1.2 kHz, a pure sample consisting only of species I is obtained for the selector, as shown in Figure B1. All other species can only be partly selected, with species VI being the most difficult one to isolate. For this species, a maximum fractional intensity of 57% is obtained at a frequency of 2.8 kHz, which corresponds to a fourfold increase compared to the fractional intensity of 14% in the free jet (indicated by the dashed line in Figure B1). This change of the species' relative abundances has to be compared with the simulated vertical intensity profiles for the deflector operated at 3 kV (A2, B2), 5 kV (A3, B3), and 8 kV (A4, B4). For 3 kV only the most polar molecules can be completely isolated from both the atomic seed gas (indicated by the dashed lines in Figures A2-A4) and the other species. The least polar molecules can be separated from species with different μ_{eff} in the lower part of the beam, but they are still overlaid with the seed gas in this region. Increasing the voltage to 5 kV completely isolates the intermediate species V and VI, the former only in a small spatial region of 0.2 mm width. The most polar molecules (species VII) are almost completely removed from the beam. These molecules are deflected so much that they either hit the electrode of the deflector or miss the skimmer behind the deflector. When 8 kV are applied to the deflector, clean samples of species I-IV are obtained. In particular, the molecules with the smallest μ_{eff} are now also isolated from the seed gas. In the deflection experiments presented in Chapters 5 and 6, the deflector was operated at 10 kV resulting in a maximum field strength of $\sim 120 \text{ kV/cm}$. An increase of the field strength by at least a factor of two should be feasible in a future version of the deflector. Since also the length of the deflector, which is only 15 cm in the present setup, can be significantly increased, thereby enhancing the deflection amplitude, deflection experiments on species with considerably smaller m/μ -ratios are realistic. In contrast, extending the selection by dynamic focusing to species with small μ_{eff}

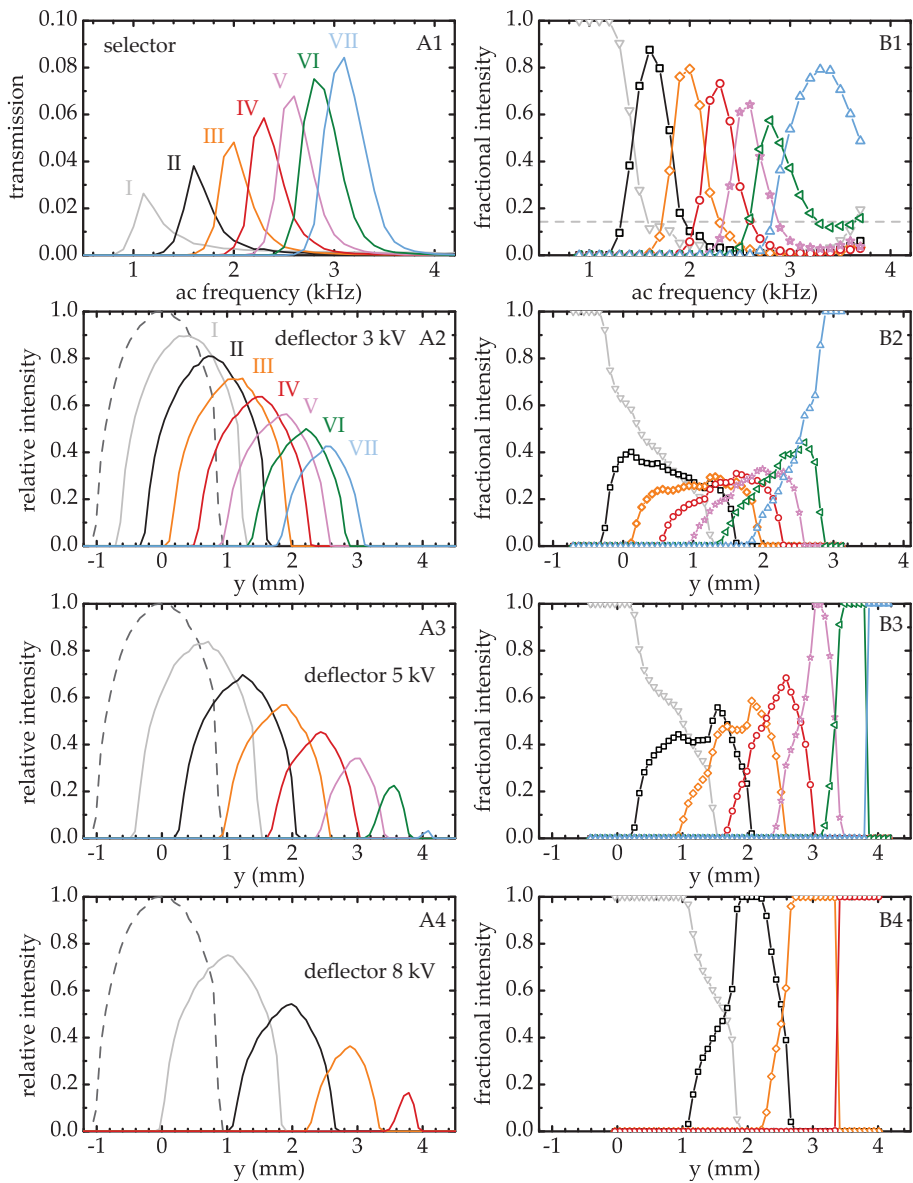


Figure 8.3: Comparison of the selectivity of a tilted selector (A1,B1) and a static deflector (A2-A4, B2-B4), the latter operated at different voltages as indicated in the figure. Simulations are performed for species with $m = 100$ u and constant effective dipole moments ranging from $0.01 \text{ cm}^{-1}/(\text{kV cm}^{-1})$ (I) to $0.07 \text{ cm}^{-1}/(\text{kV cm}^{-1})$ (VII) in steps of $0.01 \text{ cm}^{-1}/(\text{kV cm}^{-1})$. All simulations are done for a supersonic jet created by an Even-Lavie valve with Ne as the carrier gas; see text for details.

is more difficult, because the low AC frequencies that are necessary to focus these molecules would require a considerably longer selector compared to the devices discussed here.

The advantage of the selector is that it provides transverse confinement of the molecular beam, while the deflector only disperses it. In order to compare the achievable number densities for the two experiments, the number of molecules in the central part of the molecular beam (in a volume of $x \times y \times z = 1 \text{ mm} \times 1 \text{ mm} \times 10 \text{ mm}$) in the detection region is counted and compared to the free jet. For species VII, focused with a straight selector that is operated at $d = 0.50$ (see Figure 8.1 A3), an enhancement of the density compared to the free jet (at the same position at $z = 3.2 \text{ m}$) by a factor of 290 is calculated. The density in the deflected samples of species VII, when 3 kV are applied to the deflector, corresponds to $\sim 60\%$ of the density in the free jet at $z = 0.78 \text{ m}$.[§] The density in the deflected samples is calculated to be 10 times lower than the density in the focused beam at $z = 3.2 \text{ m}$ and about a factor of 30 lower than at the entrance of the selector. If a density of 10^{11} cm^{-3} is assumed at the entrance of the selector, densities of $4 \times 10^{10} \text{ cm}^{-3}$ for the 3 m-long selector and $4 \times 10^9 \text{ cm}^{-3}$ for the deflector are expected. Of course, these numbers have to be regarded as a coarse estimate since they are calculated assuming that there are no losses due to misalignment. Furthermore, the densities in deflection experiments can be improved by moving the valve closer to the deflector or using a shorter deflector. Nevertheless, the calculations presented here indicate that, at least in principle, the transverse confinement provided by the selector can provide packets of selected molecules with larger number densities than the deflector.

In a complementary approach, quantum-state and conformer selection could in principle also be achieved using an AG decelerator [50, 67, 68]. The deceleration process is quantum-state and conformer specific and could, therefore, be exploited to separate species with different m/μ -ratios in time. Although large molecules have been slightly decelerated [70], it has not been possible so far to slow them down to velocities low enough to achieve this goal. Furthermore, it is difficult to achieve quantitative agreement between the deceleration experiments and Monte Carlo simulations [71], in particular with respect to the exact effects of misalignment. In the light of this, the implementation of an improved AG focuser might help to study details of the AG focusing process and to understand these discrepancies. Whether or not it will be feasible to slow down large molecules for conformer selection remains to be seen.

[§]Note that in Figure 8.3 A2 the relative intensities are plotted. These intensities are obtained by integrating the number of molecules at a given y over the whole width of the molecular beam profile. They do not exactly reflect the relative local densities, since the width of the profile decreases with increasing deflection amplitude.

8.2 What's next ?

With both methods implemented in this work, electrostatic beam deflection and alternating gradient focusing, quantum-state- and conformer-selected samples of polar molecules are obtained. As a first application it has been demonstrated in Chapter 5 that the degree of laser induced adiabatic alignment and mixed-field orientation can be significantly improved, when deflected samples of iodobenzene molecules are provided as targets in the experiment. Similarly, other techniques for aligning and orienting molecules as, for instance, brute-force orientation [145, 146], that is, the spatial orientation of polar molecules using strong DC electric fields, are expected to benefit from the availability of state-selected molecules. In fact, as the separation of quantum states in the deflector and in the selector is based on the interaction strength of the molecules with the electric field, the states that are deflected or focused the most are also oriented the most inside the DC fields. In order to illustrate the achievable orientation with the brute-force method, the ensemble averaged orientation in a homogeneous electric field of 250 kV/cm is calculated. For a thermal ensemble of iodobenzene molecules at 1 K, $\langle \cos \theta \rangle = 0.757$ is obtained. For a deflected, quantum-state-selected sample of iodobenzene molecules at 1 % of the undeflected peak intensity (see Table 5.1), an increased ensemble averaged orientation of $\langle \cos \theta \rangle = 0.905$ is predicted.

Also for nonadiabatic alignment and orientation experiments, quantum-state selection will be beneficial. Nonadiabatic alignment is induced by laser pulses that are turned on and/or off rapidly compared to the molecular rotational periods [147, 178]. It produces transient alignment or orientation in narrow time intervals with a typical duration from a few tens of femtoseconds to a few picoseconds. A major attraction of nonadiabatic alignment and orientation is that it can occur after the laser pulse is turned off, i. e., under field-free conditions. It has been demonstrated that the dynamics and, importantly, the degree of nonadiabatic alignment and orientation depends strongly on the initial rotational state distribution [179–183]. Selection of rotational states will, therefore, be highly advantageous for nonadiabatic laser-induced schemes to control the spatial orientation of molecules. Laser-field-free impulsive alignment and orientation of quantum-state-selected NO molecules has recently been demonstrated [168]. The deflection and dynamic focusing techniques outlined in this thesis will enable similar experiments on larger, more complex molecules.

In general, complete elimination of the rotational tumbling of an asymmetric top molecule requires that all three principal axes are confined along laboratory fixed axes. This is the area of 3D alignment and orientation, which has been treated theoretically and experimentally [184–189]. A straightforward extension of the 1D alignment and orientation experiments that are presented here is to use state-selected molecules as targets for 3D alignment and orientation studies.

We have recently performed such experiments on 2,6-difluoriodobenzene molecules [189].

In general, the ability to achieve very high degrees of alignment and orientation is of great interest for a number of applications. State-selected molecules could be very beneficial for areas such as photoelectron angular distributions from fixed-in-space molecules [190], (ultrafast) diffraction with electron or X-ray sources [151, 152] and time-resolved studies of light-induced stereochemistry [191]. Furthermore, Janssen and coworkers have shown that the ability to select a single rotational state with a hexapole focuser enables new possibilities for studying directional dynamics of fragments in photodissociation of small molecules [26]. The deflection method strongly increases the number of molecules to which single rotational state selection, and subsequent orientation, can be applied. In particular, it will offer access to studies of photoinitiated processes in oriented targets of larger asymmetric tops.

Bibliography

- [1] W. E. Lamb, W. P. Schleich, M. O. Scully, and C. H. Townes, *Laser physics: Quantum controversy in action*, Rev. Mod. Phys. **71**, S263 (1999).
- [2] N. F. Ramsey, *Molecular Beams*, The International Series of Monographs on Physics (Oxford University Press, London, GB, 1956).
- [3] G. Scoles, ed., *Atomic and molecular beam methods*, vol. 1 & 2 (Oxford University Press, New York, NY, USA, 1988 & 1992).
- [4] J. B. Fenn, *Research in retrospect: Some biographical of a journeyman chemist*, Annu. Rev. Phys. Chem. **47**, 1 (1996).
- [5] O. Stern, *Ein Weg zur experimentellen Prüfung der Richtungsquantelung im Magnetfeld*, Z. Phys. **7**, 249 (1921).
- [6] W. Gerlach and O. Stern, *Der experimentelle Nachweis der Richtungsquantelung im Magnetfeld*, Z. Phys. **9**, 349 (1922).
- [7] H. Kallmann and F. Reiche, *Über den Durchgang bewegter Moleküle durch inhomogene Kraftfelder*, Z. Phys. **6**, 352 (1921).
- [8] E. Wrede, *Über die Ablenkung von Molekularstrahlen elektrischer Dipolmoleküle im inhomogenen elektrischen Feld*, Z. Phys. **44**, 261 (1927).
- [9] O. Stern, *Zur Methode der Molekularstrahlen I*, Z. Phys. **39**, 751 (1926).
- [10] I. I. Rabi, J. R. Zacharias, S. Millman, and P. Kusch, *A new method of measuring nuclear magnetic moment*, Phys. Rev. **53**, 318 (1938).
- [11] I. I. Rabi, S. Millman, P. Kusch, and J. R. Zacharias, *The molecular beam resonance method for measuring nuclear magnetic moments - the magnetic moments of ${}^6_3\text{Li}$, ${}^7_3\text{Li}$ and ${}^{19}_9\text{F}$* , Phys. Rev. **55**, 526 (1939).
- [12] R. Moro, X. Xu, S. Yin, and W. A. de Heer, *Ferroelectricity in free niobium clusters*, Science **300**, 1265 (2003).

- [13] W. A. de Heer and V. V. Kresin, *Electric and magnetic dipole moments of free nanoclusters*, arXiv p. 0901.4810 (2009), article prepared for the Handbook of Nanophysics, ed. by Klaus D. Sattler, to be published by Taylor&Francis/CRC Press.
- [14] M. Broyer, R. Antoine, I. Compagnon, D. Rayane, and P. Dugourd, *From clusters to biomolecules: Electric dipole, structure and dynamics*, Phys. Scr. **76**, C135 (2007).
- [15] H. Friedburg and W. Paul, *Optische Abbildung mit neutralen Atomen*, Die Naturwissenschaften **38**, 159 (1951).
- [16] H. G. Bennewitz and W. Paul, *Eine Methode zur Bestimmung von Kernmomenten mit fokussiertem Atomstrahl*, Z. Phys. **139**, 489 (1954).
- [17] H. G. Bennewitz, W. Paul, and C. Schlier, *Fokussierung polarer Moleküle*, Z. Phys. **141**, 6 (1955).
- [18] J. P. Gordon, H. J. Zeiger, and C. H. Townes, *Molecular microwave oscillator and new hyperfine structure in the microwave spectrum of NH₃*, Phys. Rev. **95**, 282 (1954).
- [19] J. P. Gordon, H. J. Zeiger, and C. H. Townes, *The Maser - new type of microwave amplifier, frequency standard, and spectrometer*, Phys. Rev. **99**, 1264 (1955).
- [20] H. G. Bennewitz, K. H. Kramer, J. P. Toennies, and W. Paul, *Messung der Anisotropie des van der Waals-Potentials durch Streuung von Molekülen in definiertem Quantenzustand*, Z. Phys. **177**, 84 (1964).
- [21] P. R. Brooks and E. M. Jones, *Reactive scattering of K atoms from oriented CH₃I molecules*, J. Chem. Phys. **45**, 3449 (1966).
- [22] R. J. Beuhler, R. B. Bernstein, and K. H. Kramer, *Observation of reactive asymmetry of methyl iodide. Crossed beam study of reaction of rubidium with oriented methyl iodide molecules*, J. Am. Chem. Soc. **88**, 5331 (1966).
- [23] D. H. Parker and R. B. Bernstein, *Oriented molecule beams via the electrostatic hexapole - preparation, characterization, and reactive scattering*, Annu. Rev. Phys. Chem. **40**, 561 (1989).
- [24] S. Stolte, in [3], chap. 25, pp. 631–652.
- [25] E. W. Kuipers, M. G. Tenner, A. Kleyn, and S. Stolte, *Observation of steric effects in gas-surface scattering*, Nature **334**, 420 (1988).
- [26] T. P. Rakitzis, A. J. van den Brom, and M. H. M. Janssen, *Directional dynamics in the photodissociation of oriented molecules*, Science **303**, 1852 (2004).

- [27] H. L. Bethlem, G. Berden, and G. Meijer, *Decelerating neutral dipolar molecules*, Phys. Rev. Lett. **83**, 1558 (1999).
- [28] S. Y. T. van de Meerakker, H. L. Bethlem, and G. Meijer, in [192], chap. 14.
- [29] S. Y. T. van de Meerakker, H. L. Bethlem, and G. Meijer, *Taming molecular beams*, Nature Phys. **4**, 595 (2008).
- [30] H. L. Bethlem, G. Berden, F. M. H. Crompvoets, R. T. Jongma, A. J. A. van Roij, and G. Meijer, *Electrostatic trapping of ammonia molecules*, Nature **406**, 491 (2000).
- [31] S. Y. T. van de Meerakker, P. H. M. Smeets, N. Vanhaecke, R. T. Jongma, and G. Meijer, *Deceleration and electrostatic trapping of OH radicals*, Phys. Rev. Lett. **94**, 023004 (2005).
- [32] F. M. H. Crompvoets, H. L. Bethlem, R. T. Jongma, and G. Meijer, *A prototype storage ring for neutral molecules*, Nature **411**, 174 (2001).
- [33] C. E. Heiner, D. Carty, G. Meijer, and H. L. Bethlem, *A molecular synchrotron*, Nature Phys. **3**, 115 (2007).
- [34] J. J. Gilijamse, S. Hoekstra, S. Y. T. van de Meerakker, G. C. Groenenboom, and G. Meijer, *Near-threshold inelastic collisions using molecular beams with a tunable velocity*, Science **313**, 1617 (2006).
- [35] S. Y. T. van de Meerakker, N. Vanhaecke, M. P. J. van der Loo, G. C. Groenenboom, and G. Meijer, *Direct measurement of the radiative lifetime of vibrationally excited OH radicals*, Phys. Rev. Lett. **95**, 013003 (2005).
- [36] J. J. Gilijamse, S. Hoekstra, S. A. Meek, M. Metsälä, S. Y. T. v. de Meerakker, G. Meijer, and G. C. Groenenboom, *The radiative lifetime of metastable CO ($a^3\Pi, v=0$)*, J. Chem. Phys. **127**, 221102 (2007).
- [37] S. Hoekstra, J. J. Gilijamse, B. Sartakov, N. Vanhaecke, L. Scharfenberg, S. Y. T. van de Meerakker, and G. Meijer, *Optical pumping of trapped neutral molecules by blackbody radiation*, Phys. Rev. Lett. **98**, 133001 (2007).
- [38] R. Fulton, A. I. Bishop, and P. F. Barker, *Optical Stark decelerator for molecules*, Phys. Rev. Lett. **93**, 243004 (2004).
- [39] N. Vanhaecke, U. Meier, M. Andrist, B. H. Meier, and F. Merkt, *Multistage Zeeman deceleration of hydrogen atoms*, Phys. Rev. A **75**, 031402(R) (2007).
- [40] E. Narevicius, C. G. Parthey, A. Libson, J. Narevicius, I. Chavez, U. Even, and M. G. Raizen, *An atomic coilgun: Using pulsed magnetic fields to slow a supersonic beam*, New J. Phys. **9**, 358 (2007).

- [41] M. G. Raizen, *Comprehensive control of atomic motion*, Science **324**, 1403 (2009).
- [42] S. A. Meek, H. Conrad, and G. Meijer, *Trapping molecules on a chip*, Science **324**, 1699 (2009).
- [43] W. Ketterle and D. E. Pritchard, *Trapping and focusing ground-state atoms with static fields*, Appl. Phys. B **54**, 403 (1992).
- [44] W. H. Wing, *On neutral particle trapping in quasistatic electromagnetic fields*, Prog. Quant. Electr. **8**, 181 (1984).
- [45] E. D. Courant and H. S. Snyder, *Theory of the alternating-gradient synchrotron*, Ann. Phys. **3**, 1 (1958).
- [46] E. D. Courant, M. S. Livingston, and H. S. Snyder, *The strong-focusing synchrotron- a new high energy accelerator*, Phys. Rev. **88**, 1190 (1952).
- [47] W. Paul, *Electromagnetic traps for charged and neutral particles*, Rev. Mod. Phys. **62**, 531 (1990).
- [48] W. Paul and H. Steinwedel, *Ein neues Massenspektrometer ohne Magnetfeld*, Z. Naturforsch. A **8**, 448 (1953).
- [49] W. Paul, O. Osberghaus, and E. Fischer, *Ein Ionenkäfig*, Forschungsberichte des Wirtschafts- und Verkehrsministeriums Nordrhein Westfalen (1958).
- [50] D. Auerbach, E. E. A. Bromberg, and L. Wharton, *Alternate-gradient focusing of molecular beams*, J. Chem. Phys. **45**, 2160 (1966).
- [51] D. Kakati and D. C. Lainé, *Alternate-gradient focusing of a molecular beam of ammonia*, Phys. Lett. A **24**, 676 (1967).
- [52] D. Kakati and D. C. Lainé, *Alternate-gradient focusing of neutral particles*, Phys. Lett. A **28**, 786 (1969).
- [53] D. Kakati and D. C. Lainé, *Alternate-gradient focusing of a molecular beam*, J. Phys. E **4**, 269 (1971).
- [54] A. Lübbert, F. Günther, and K. Schügerl, *Focusing of polar molecules in an alternate gradient focusing system*, Chem. Phys. Lett. **35**, 210 (1975).
- [55] F. Günther and K. Schügerl, *State selection of polar molecules by alternate gradient focussing*, Z. Phys. Chem. **NF 80**, 155 (1972).
- [56] A. Lübbert, G. Rotzoll, and F. Günther, *Molecular beam focusing of ICl in rotational states with positive induced electric dipole moments*, J. Chem. Phys. **69**, 5174 (1978).

- [57] T. Junglen, T. Rieger, S. A. Rangwala, P. W. H. Pinkse, and G. Rempe, *Two-dimensional trapping of dipolar molecules in time-varying electric fields*, Phys. Rev. Lett. **92**, 223001 (2004).
- [58] T. E. Wall, S. Armitage, J. J. Hudson, B. E. Sauer, J. M. Dyne, E. A. Hinds, and M. R. Tarbutt, *Transport of polar molecules by an alternating gradient guide*, Phys. Rev. A **80**, 043407 (2009).
- [59] D. H. H. Al-Amiedy and D. C. Lainé, *Ring-type state selector and space focuser for molecules with a positive induced dipole moment*, Phys. Lett. A **66**, 94 (1978).
- [60] D. C. Lainé and R. Sweeting, *Crossed-wire focuser for molecular beams*, Phys. Lett. A **34**, 144 (1971).
- [61] J. C. Helmer, F. B. Jacobus, and P. A. Sturrock, *Focusing molecular beams of NH_3* , J. Appl. Phys. **31**, 458 (1960).
- [62] K.-R. Chien, P. B. Foreman, K. H. Castleton, and S. G. Kukolich, *Relaxation cross section measurements on NH_3 and lower state focussing in a beam maser*, Chem. Phys. **7**, 161 (1975).
- [63] H.-J. Loesch, *A novel simple rotational state analyser/selector for polar linear molecules*, Chem. Phys. **207**, 427 (1996).
- [64] H. J. Loesch and B. Scheel, *Molecules on Kepler orbits: An experimental study*, Phys. Rev. Lett. **85**, 2709 (2000).
- [65] R. Wolfgang, *Chemical accelerators*, Sci. Am. **219**, 44 (1968).
- [66] E. E. A. Bromberg, *Acceleration and alternate-gradient focusing of neutral polar diatomic molecules*, Ph.D. thesis, University of Chicago, Chicago, IL, USA (1972).
- [67] H. L. Bethlem, A. J. A. van Roij, R. T. Jongma, and G. Meijer, *Alternate gradient focusing and deceleration of a molecular beam*, Phys. Rev. Lett. **88**, 133003 (2002).
- [68] H. L. Bethlem, M. R. Tarbutt, J. Küpper, D. Carty, K. Wohlfart, E. A. Hinds, and G. Meijer, *Alternating gradient focusing and deceleration of polar molecules*, J. Phys. B **39**, R263 (2006).
- [69] M. R. Tarbutt, H. L. Bethlem, J. J. Hudson, V. L. Ryabov, V. A. Ryzhov, B. E. Sauer, G. Meijer, and E. A. Hinds, *Slowing heavy, ground-state molecules using an alternating gradient decelerator*, Phys. Rev. Lett. **92**, 173002 (2004).
- [70] K. Wohlfart, F. Grätz, F. Filsinger, H. Haak, G. Meijer, and J. Küpper, *Alternating-gradient focusing and deceleration of large molecules*, Phys. Rev. A **77**, 031404(R) (2008).

- [71] K. Wohlfart, *Alternating-gradient focusing and deceleration of large molecules*, Dissertation, Free University, Berlin, Germany (2008).
- [72] K. Wohlfart, F. Filsinger, F. Grätz, J. Küpper, and G. Meijer, *Stark deceleration of OH radicals in low-field-seeking and high-field-seeking quantum states*, Phys. Rev. A **78**, 033421 (2008).
- [73] J. van Veldhoven, H. L. Bethlem, and G. Meijer, *AC electric trap for ground-state molecules*, Phys. Rev. Lett. **94**, 083001 (2005).
- [74] H. L. Bethlem, J. van Veldhoven, M. Schnell, and G. Meijer, *Trapping polar molecules in an ac trap*, Phys. Rev. A **74**, 063403 (2006).
- [75] Special issue "Molecular physics of building blocks of life under isolated or defined conditions", Eur. Phys. J. D **20**, 309 (2002).
- [76] Special issue "Bio-active molecules in the gas phase", Phys. Chem. Chem. Phys. **6**, 2543 (2004).
- [77] M. S. de Vries and P. Hobza, *Gas-phase spectroscopy of biomolecular building blocks*, Annu. Rev. Phys. Chem. **58**, 585 (2007).
- [78] F. Piuzzi, M. Mons, I. Dimicoli, B. Tardivel, and Q. Zhao, *Ultraviolet spectroscopy and tautomerism of the DNA base guanine and its hydrate formed in a supersonic jet*, Chem. Phys. **270**, 205 (2001).
- [79] S. K. Kim, W. Lee, and D. R. Herschbach, *Cluster beam chemistry: Hydration of nucleic acid bases; ionization potentials of hydrated adenine and thymine*, J. Phys. Chem. **100**, 7933 (1996).
- [80] T. R. Rizzo, Y. D. Park, L. Peteanu, and D. H. Levy, *Electronic spectrum of the amino acid tryptophan cooled in a supersonic molecular beam*, J. Chem. Phys. **83**, 4819 (1985).
- [81] R. D. Suenram and F. J. Lovas, *Millimeter wave spectrum of glycine - a new conformer*, J. Am. Chem. Soc. **102**, 7180 (1980).
- [82] E. Nir, K. Kleinermanns, and M. S. de Vries, *Pairing of isolated nucleic-acid bases in the absence of the DNA backbone*, Nature **408**, 949 (2000).
- [83] L. C. Snoek, E. G. Robertson, R. T. Kroemer, and J. P. Simons, *Conformational landscapes in amino acids: Infrared and ultraviolet ion-dip spectroscopy of phenylalanine in the gas phase*, Chem. Phys. Lett. **321**, 49 (2000).
- [84] J. M. Bakker, L. M. Aleese, G. Meijer, and G. von Helden, *Fingerprint IR spectroscopy to probe amino acid conformations in the gas phase*, Phys. Rev. Lett. **91**, 203003 (2003).

- [85] F. Dong and R. E. Miller, *Vibrational transition moment angles in isolated biomolecules: A structural tool*, *Science* **298**, 1227 (2002).
- [86] A. Lesarri, E. J. Cocinero, J. C. Lopez, and J. L. Alonso, *The shape of neutral valine*, *Angew. Chem. Int. Ed.* **43**, 605 (2004).
- [87] J. A. Reese, T. V. Nguyen, T. M. Korter, and D. W. Pratt, *Charge redistribution on electronic excitation. Dipole moments of cis and trans 3-aminophenol in their S_0 and S_1 electronic states*, *J. Am. Chem. Soc.* **126**, 11387 (2004).
- [88] B. C. Dian, J. R. Clarkson, and T. S. Zwier, *Direct measurement of energy thresholds to conformational isomerization in tryptamine*, *Science* **303**, 1169 (2004).
- [89] K. Hedberg, L. Hedberg, D. S. Bethune, C. A. Brown, H. C. Dorn, R. D. Johnson, and M. de Vries, *Bond lengths in free molecules of buckminsterfullerene, C_{60} , from gas-phase electron diffraction*, *Science* **254**, 410 (1991).
- [90] H. N. Chapman, A. Barty, M. J. Bogan, S. Boutet, S. Frank, S. P. Hau-Riege, S. Marchesini, B. W. Woods, S. Bajt, W. H. Benner, L. W. A., E. Plönjes, M. Kuhlmann, R. Treusch, S. Düsterer, T. Tschentscher, J. R. Schneider, E. Spiller, T. Möller, C. Bostedt, M. Hoener, D. A. Shapiro, K. O. Hodgson, D. van der Spoel, F. Burmeister, M. Bergh, C. Caleman, G. Huldt, M. M. Seibert, F. R. N. C. Maia, R. W. Lee, A. Szönke, N. Timneanu, and J. Hajdu, *Femtosecond diffractive imaging with a soft-x-ray free-electron laser*, *Nature Phys.* **2**, 839 (2006).
- [91] J. Itatani, J. Levesque, D. Zeidler, H. Niikura, H. Pépin, J. C. Kieffer, P. B. Corkum, and D. M. Villeneuve, *Tomographic imaging of molecular orbitals*, *Nature* **432**, 867 (2004).
- [92] G. von Helden, T. Wyttenbach, and M. T. Bowers, *Conformation of macromolecules in the gas-phase – use of matrix-assisted laser-desorption methods in ion chromatography*, *Science* **267**, 1483 (1995).
- [93] M. Jarrold, *Helices and sheets in vacuo*, *Phys. Chem. Chem. Phys.* **9**, 1659 (2007).
- [94] B. C. Dian, A. Longarte, and T. S. Zwier, *Conformational dynamics in a dipeptide after single-mode vibrational excitation*, *Science* **296**, 2369 (2002).
- [95] U. Erlekam, M. Frankowski, G. von Helden, and G. Meijer, *Cold collisions catalyse conformational conversion*, *Phys. Chem. Chem. Phys.* **9**, 3786 (2007).
- [96] I. Compagnon, F. C. Hagemester, R. Antoine, D. Rayane, M. Broyer, P. Dugourd, R. R. Hudgins, and M. F. Jarrold, *Permanent electric dipole and conformation of unsolvated tryptophan*, *J. Am. Chem. Soc.* **123**, 8440 (2001).

- [97] R. Antoine, I. Compagnon, D. Rayane, M. Broyer, P. Dugourd, G. Breaux, F. C. Hagemeister, D. Pippen, R. R. Hudgins, and M. F. Jarrold, *Electric susceptibility of unsolvated glycine-based peptides*, *J. Am. Chem. Soc.* **124**, 6737 (2002).
- [98] I. Compagnon, R. Antoine, D. Rayane, M. Broyer, and P. Dugourd, *Vibration induced electric dipole in a weakly bound molecular complex*, *Phys. Rev. Lett.* **89**, 253001 (2002).
- [99] M. Born and R. Oppenheimer, *Zur Quantentheorie der Molekeln*, *Ann. Physik* **84**, 457 (1927).
- [100] C. Eckart, *Some studies concerning rotating axes and polyatomic molecules*, *Phys. Rev.* **47**, 552 (1935).
- [101] W. Demtröder, *Molekülphysik* (Oldenbourg Wissenschaftsverlag, München, 2003).
- [102] B. S. Ray, *Über die Eigenwerte des asymmetrischen Kreisels*, *Z. Phys.* **78**, 74 (1932).
- [103] W. Gordy and R. L. Cook, *Microwave Molecular Spectra* (John Wiley & Sons, New York, NY, USA, 1984), 3rd ed.
- [104] J. E. Wollrab, *Rotational Spectra and Molecular Structure* (Academic Press, New York, NY, USA, 1967).
- [105] G. W. King, R. M. Hainer, and P. C. Cross, *The asymmetric rotor I. Calculation and symmetry classification of energy levels*, *J. Chem. Phys.* **11**, 27 (1943).
- [106] M. Abd El Rahim, R. Antoine, M. Broyer, D. Rayane, and P. Dugourd, *Asymmetric top rotors in electric fields: Influence of chaos and collisions in molecular beam deflection experiments*, *J. Phys. Chem. A* **109**, 8507 (2005).
- [107] J. K. G. Watson, in *Vibrational Spectra and Structure*, edited by J. R. Durig (Marcel Dekker, 1977), vol. 6, chap. 1.
- [108] S. C. Wang, *On the asymmetrical top in quantum mechanics*, *Phys. Rev.* **34**, 243 (1929).
- [109] R. Mulliken, *Species classification and rotational energy level patterns of non-linear triatomic molecules*, *Phys. Rev.* **59**, 873 (1941).
- [110] P. A. M. Dirac, *The principles of quantum mechanics* (Oxford University Press, Amen House, London E. C. 4, UK, 1947), 3rd ed.
- [111] P. R. Bunker and P. Jensen, *Molecular Symmetry and Spectroscopy* (NRC Research Press, Ottawa, Ontario, Canada, 1998), 2nd ed.

- [112] C. H. Townes and A. L. Schawlow, *Microwave Spectroscopy* (Dover Publications, New York, 1975).
- [113] B. Kleibömer and D. H. Sutter, *The vibrational-state dependence of the ^{14}N quadrupole coupling tensor in aniline - a microwave Fourier-transform study combined with semirigid bender calculations.*, *Z. Naturforsch. A* **43**, 561 (1988).
- [114] D. R. Borst, T. M. Korter, and D. W. Pratt, *On the additivity of bond dipole moments. Stark effect studies of the rotationally resolved electronic spectra of aniline, benzonitrile, and aminobenzonitrile*, *Chem. Phys. Lett.* **350**, 485 (2001).
- [115] J. Küpper and F. Filsinger, *libcoldmol: A particle trajectory calculation framework* (2003-2008), URL: <http://libcoldmol.cold-molecules.info>.
- [116] M. R. Tarbutt and E. A. Hinds, *Nonlinear dynamics in an alternating gradient guide for neutral particles*, *New J. Phys.* **10**, 073011 (2008).
- [117] S. Y. T. van de Meerakker, N. Vanhaecke, H. L. Bethlem, and G. Meijer, *Transverse stability in a Stark decelerator*, *Phys. Rev. A* **73**, 023401 (2006).
- [118] F. Filsinger, U. Erlekam, G. von Helden, J. Küpper, and G. Meijer, *Selector for structural isomers of neutral molecules*, *Phys. Rev. Lett.* **100**, 133003 (2008).
- [119] J. A. Richards, R. M. Huey, and J. Hiller, in *Proceedings of the Institution of Radio and Electronics Engineers, Australia* (1971), vol. 32, pp. 321-322.
- [120] J. A. Richards, R. M. Huey, and J. Hiller, *A new operating mode for the quadrupole mass filter*, *Int. J. Mass Spectrom. Ion Proc.* **12**, 317 (1973).
- [121] N. Kononkov, M. Sudakov, and D. Douglas, *Matrix methods for the calculation of stability diagrams in quadrupole mass spectrometry*, *J. Am. Soc. Mass. Spectrom.* **13**, 597 (2002).
- [122] L. A. Pipes, *Matrix solution of equations of the Mathieu-Hill type*, *J. Appl. Phys.* **24**, 902 (1953).
- [123] P. Lützwow, M. Schnell, and G. Meijer, *Instabilities of molecule motion in a linear ac trap*, *Phys. Rev. A* **77**, 063402 (2008).
- [124] W. Paul and M. Raether, *Das elektrische Massenfilter*, *Z. Phys.* **140**, 262 (1955).
- [125] Y. R. Wu and D. H. Levy, *Determination of the geometry of deuterated tryptamine by rotationally resolved electronic spectroscopy*, *J. Chem. Phys.* **91**, 5278 (1989).

- [126] C. M. Western, *PGOPHER, a program for simulating rotational structure* (2003-2007), University of Bristol, Bristol, UK, URL: <http://pgopher.chm.bris.ac.uk>.
- [127] R. Weinkauff, J. Schermann, M. S. de Vries, and K. Kleinermanns, *Molecular physics of building blocks of life under isolated or defined conditions*, *Eur. Phys. J. D* **20**, 309 (2002).
- [128] J. P. Simons, *Bio-active molecules in the gas phase*, *Phys. Chem. Chem. Phys.* **6**, E7 (2004).
- [129] C. Unterberg, A. Gerlach, A. Jansen, and M. Gerhards, *Structures and vibrations of neutral and cationic 3-and 4-aminophenol*, *Chem. Phys.* **304**, 237 (2004).
- [130] M. Shinozaki, M. Sakai, S. Yamaguchi, T. Fujioka, and M. Fujii, *$S_1 \leftarrow S_0$ electronic spectrum of jet-cooled *m*-aminophenol*, *Phys. Chem. Chem. Phys.* **5**, 5044 (2003).
- [131] D. G. Lister, J. K. Tyler, J. H. Høg, and N. W. Larsen, *The microwave spectrum, structure and dipole moment of aniline*, *J. Mol. Struct.* **23**, 253 (1974).
- [132] N. W. Larsen, *Microwave spectra of the six mono- ^{13}C -substituted phenols and of some monodeuterated species of phenol. Complete substitution structure and absolute dipole moment*, *J. Mol. Struct.* **51**, 175 (1979).
- [133] J.-U. Grabow, W. Stahl, and H. Dreizler, *A multioctave coaxially oriented beam-resonator arrangement Fourier-transform microwave spectrometer*, *Rev. Sci. Instrum.* **67**, 4072 (1996).
- [134] M. Schnell, D. Banser, and J.-U. Grabow, *Coaxially aligned electrodes for Stark-effect applied in resonators using a supersonic jet Fourier transform microwave spectrometer*, *Rev. Sci. Instrum.* **75**, 2111 (2004).
- [135] J. M. L. J. Reinartz and A. Dymanus, *Molecular constants of OCS isotopes in the (01^10) vibrational state measured by molecular-beam electric-resonance spectroscopy*, *Chem. Phys. Lett.* **24**, 346 (1974).
- [136] M. J. Frisch, G. W. Trucks, H. B. Schlegel, G. E. Scuseria, M. A. Robb, J. R. Cheeseman, J. J. A. Montgomery, T. Vreven, K. N. Kudin, J. C. Burant, J. M. Millam, S. S. Iyengar, J. Tomasi, V. Barone, B. Mennucci, M. Cossi, G. Scalmani, N. Rega, G. A. Petersson, H. Nakatsuji, M. Hada, M. Ehara, K. Toyota, R. Fukuda, J. Hasegawa, M. Ishida, T. Nakajima, Y. Honda, O. Kitao, H. Nakai, M. Klene, X. Li, J. E. Knox, H. P. Hratchian, J. B. Cross, V. Bakken, C. Adamo, J. Jaramillo, R. Gomperts, R. E. Stratmann, O. Yazyev, A. J. Austin, R. Cammi, C. Pomelli, J. W. Ochterski, P. Y. Ayala,

- K. Morokuma, G. A. Voth, P. Salvador, J. J. Dannenberg, V. G. Zakrzewski, S. Dapprich, A. D. Daniels, M. C. Strain, O. Farkas, D. K. Malick, A. D. Rabuck, K. Raghavachari, J. B. Foresman, J. V. Ortiz, Q. Cui, A. G. Baboul, S. Clifford, J. Cioslowski, B. B. Stefanov, G. Liu, A. Liashenko, P. Piskorz, I. Komaromi, R. L. Martin, D. J. Fox, T. Keith, M. A. Al-Laham, C. Y. Peng, A. Nanayakkara, M. Challacombe, P. M. W. Gill, B. Johnson, W. Chen, M. W. Wong, C. Gonzalez, and J. A. Pople, *Gaussian 03, Gaussian, Inc., Wallingford CT* (2004).
- [137] Z. Kisiel, J. Kosarzewski, B. A. Pietrewicz, and L. Pszczółkowski, *Electric dipole moments of the cyclic trimers (H₂O)₂HCl and (H₂O)₂HBr from Stark effects in their rotational spectra*, Chem. Phys. Lett. **325**, 523 (2000).
- [138] Z. Kisiel, B. A. Pietrewicz, P. W. Fowler, A. C. Legon, and E. Steiner, *Rotational spectra of the less common isotopomers, electric dipole moment and the double minimum inversion potential of H₂O ... HCl*, J. Phys. Chem. A **104**, 6970 (2000).
- [139] S. G. Kukolich, *Measurement of ammonia hyperfine structure with a two-cavity maser*, Phys. Rev. **156**, 83 (1967).
- [140] S. G. Kukolich, *Measurement of hyperfine structure of the J=3, K=2 inversion line of ¹⁴NH₃*, Phys. Rev. **138**, A1322 (1965).
- [141] J. van Veldhoven, J. Küpper, H. L. Bethlem, B. Sartakov, A. J. A. van Roij, and G. Meijer, *Decelerated molecular beams for high-resolution spectroscopy: The hyperfine structure of ¹⁵ND₃*, Eur. Phys. J. D **31**, 337 (2004).
- [142] N. W. Larsen, E. L. Hansen, and F. M. Nicolaisen, *Far infrared investigation of aniline and 4-fluoroaniline in vapor-phase - inversion and torsion of amino group*, Chem. Phys. Lett. **43**, 584 (1976).
- [143] R. A. Kydd and P. J. Krueger, *Far-infrared vapor-phase spectra of aniline-ND₂ and aniline-NHD*, Chem. Phys. Lett. **49**, 539 (1977).
- [144] M. Gerhards, A. Jansen, C. Unterberg, and A. Gerlach, *Structures and rearrangement reactions of 4-aminophenol(H₂O)₁⁺ and 3-aminophenol(H₂O)₁⁺ clusters*, J. Chem. Phys. **123**, 074320 (2005).
- [145] H. J. Loesch and A. Remscheid, *Brute force in molecular reaction dynamics: A novel technique for measuring steric effects*, J. Chem. Phys. **93**, 4779 (1990).
- [146] B. Friedrich and D. R. Herschbach, *Spatial orientation of molecules in strong electric fields and evidence for pendular states*, Nature **353**, 412 (1991).
- [147] H. Stapelfeldt and T. Seideman, *Colloquium: Aligning molecules with strong laser pulses*, Rev. Mod. Phys. **75**, 543 (2003).

- [148] B. Friedrich and D. Herschbach, *Alignment and trapping of molecules in intense laser fields*, Phys. Rev. Lett. **74**, 4623 (1995).
- [149] B. Friedrich and D. Herschbach, *Enhanced orientation of polar molecules by combined electrostatic and nonresonant induced dipole forces*, J. Chem. Phys. **111**, 6157 (1999).
- [150] B. Friedrich and D. Herschbach, *Manipulating molecules via combined static and laser fields*, J. Phys. Chem. A **103**, 10280 (1999).
- [151] J. C. H. Spence and R. B. Doak, *Single molecule diffraction*, Phys. Rev. Lett. **92**, 198102 (2004).
- [152] E. R. Peterson, C. Buth, D. A. Arms, R. W. Dunford, E. P. Kanter, B. Krassig, E. C. Landahl, S. T. Pratt, R. Santra, S. H. Southworth, and L. Young, *An X-ray probe of laser-aligned molecules*, Astrophys. Lett. & Comm. **92**, 094106 (2008).
- [153] J. Levesque, Y. Mairesse, N. Dudovich, H. Pépin, J.-C. Kieffer, P. B. Corkum, and D. M. Villeneuve, *Polarization state of high-order harmonic emission from aligned molecules*, Phys. Rev. Lett. **99**, 243001 (2007).
- [154] M. Hillenkamp, S. Keinan, and U. Even, *Condensation limited cooling in supersonic expansions*, J. Chem. Phys. **118**, 8699 (2003).
- [155] B. Friedrich and D. Herschbach, *Polarization of molecules induced by intense nonresonant laser fields*, J. Phys. Chem. **99**, 15686 (1995).
- [156] U. Buck and M. Fárnik, *Oriented xenon hydride molecules in the gas phase*, Int. Rev. Phys. Chem. **25**, 583 (2006).
- [157] S. Minemoto, H. Nanjo, H. Tanji, T. Suzuki, and H. Sakai, *Observation of molecular orientation by the combination of electrostatic and nonresonant, pulsed laser fields*, J. Chem. Phys. **118**, 4052 (2003).
- [158] L. Holmegaard, J. H. Nielsen, I. Nevo, H. Stapelfeldt, F. Filsinger, J. Küpper, and G. Meijer, *Laser-induced alignment and orientation of quantum-state-selected large molecules*, Phys. Rev. Lett. **102**, 023001 (2009).
- [159] H. Sakai, C. P. Safvan, J. J. Larsen, K. M. Hilligsøe, K. Hald, and H. Stapelfeldt, *Controlling the alignment of neutral molecules by a strong laser field*, J. Chem. Phys. **110**, 10235 (1999).
- [160] U. Even, J. Jortner, D. Noy, N. Lavie, and N. Cossart-Magos, *Cooling of large molecules below 1 K and He clusters formation*, J. Chem. Phys. **112**, 8068 (2000).

- [161] K. Wohlfart, M. Schnell, J.-U. Grabow, and J. Küpper, *Precise dipole moment and quadrupole coupling constants of benzonitrile*, *J. Mol. Spec.* **247**, 119 (2008).
- [162] G. Berden, W. L. Meerts, and E. Jalviste, *Rotationally resolved ultraviolet spectroscopy of indole, indazole, and benzimidazole: Inertial axis reorientation in the $S_1(^1L_b) \leftarrow S_0$ transitions*, *J. Chem. Phys.* **103**, 9596 (1995).
- [163] O. Dorosh, E. Białkowska-Jaworska, Z. Kisiel, and L. Pszczółkowski, *New measurements and global analysis of rotational spectra of Cl-, Br-, and I-benzene: Spectroscopic constants and electric dipole moments*, *J. Mol. Spec.* **246**, 228 (2007).
- [164] M. Kirste, B. G. Sartakov, M. Schnell, and G. Meijer, *Nonadiabatic transitions in electrostatically trapped ammonia molecules*, *Phys. Rev. A* **79**, 051401(R) (2009).
- [165] J. J. Larsen, H. Sakai, C. P. Safvan, I. Wendt-Larsen, and H. Stapelfeldt, *Aligning molecules with intense nonresonant laser fields*, *J. Chem. Phys.* **111**, 7774 (1999).
- [166] V. Kumarappan, C. Z. Bisgaard, S. S. Viftrup, L. Holmegaard, and H. Stapelfeldt, *Role of rotational temperature in adiabatic molecular alignment*, *J. Chem. Phys.* **125**, 194309 (2006).
- [167] A. Gijsbertsen, W. Siu, M. F. Kling, P. Johnsson, P. Jansen, S. Stolte, and M. J. J. Vrakking, *Direct determination of the sign of the NO dipole moment*, *Phys. Rev. Lett.* **99**, 213003 (2007).
- [168] O. Ghafur, A. Rouzee, A. Gijsbertsen, W. K. Siu, S. Stolte, and M. J. J. Vrakking, *Impulsive orientation and alignment of quantum-state-selected NO molecules*, *Nature Phys.* **5**, 289 (2009).
- [169] C. Ng, *Vacuum ultraviolet spectroscopy and chemistry by photoionization and photoelectron methods*, *Annu. Rev. Phys. Chem.* **53**, 101 (2002).
- [170] W. Li, X. Zhou, R. Lock, S. Patchkovskii, A. Stolow, H. C. Kapteyn, and M. M. Murnane, *Time-resolved dynamics in N_2O_4 probed using high harmonic generation*, *Science* **322**, 1207 (2008).
- [171] M. E. Sanz, S. Blanco, J. C. Lopez, and J. L. Alonso, *Rotational probes of six conformers of neutral cysteine*, *Angew. Chem. Int. Ed.* **47**, 6216 (2008).
- [172] R. Neutze, R. Wouts, D. van der Spoel, E. Weckert, and J. Hajdu, *Potential for biomolecular imaging with femtosecond X-ray pulses*, *Nature* **406**, 752 (2000).

- [173] J. Küpper, H. Junkes, and U. Hoppe, *KouDA: A general purpose data acquisition system* (2003-2008), <http://kouda.cold-molecules.info>.
- [174] R. V. Latham, *High voltage vacuum insulation: basic concepts and technological practice* (Academic Press, London, 1995).
- [175] G. Berden, J. van Rooy, W. L. Meerts, and K. A. Zachariasse, *Rotationally resolved electronic spectroscopy of 4-aminobenzonitrile*, *Chem. Phys. Lett.* **278**, 373 (1997).
- [176] F. Filsinger, K. Wohlfart, M. Schnell, J.-U. Grabow, and J. Küpper, *Precise dipole moments and quadrupole coupling constants of the cis and trans conformers of 3-aminophenol: Determination of the absolute conformation*, *Phys. Chem. Chem. Phys.* **10**, 666 (2008).
- [177] U. Even, *private communication* (2009).
- [178] F. Rosca-Pruna and M. J. J. Vrakking, *Experimental observation of revival structures in picosecond laser-induced alignment of I₂*, *Phys. Rev. Lett.* **87**, 153902 (2001).
- [179] T. Seideman, *On the dynamics of rotationally broad, spatially aligned wave packets*, *J. Chem. Phys.* **115**, 5965 (2001).
- [180] M. Machholm, *Postpulse alignment robust to thermal averaging*, *J. Chem. Phys.* **115**, 10724 (2001).
- [181] F. Rosca-Pruna and M. J. J. Vrakking, *Revival structures in picosecond laser-induced alignment of I₂ molecules. II. Numerical modeling*, *J. Chem. Phys.* **116**, 6579 (2002).
- [182] E. Péronne, M. D. Poulsen, H. Stapelfeldt, C. Z. Bisgaard, E. Hamilton, and T. Seideman, *Nonadiabatic laser-induced alignment of iodobenzene molecules*, *Phys. Rev. A* **70**, 063410 (2004).
- [183] M. Muramatsu, M. Hita, S. Minemoto, and H. Sakai, *Field-free molecular orientation by an intense nonresonant two-color laser field with a slow turn on and rapid turn off*, *Phys. Rev. A* **79**, 011403(R) (2009).
- [184] J. J. Larsen, K. Hald, N. Bjerre, H. Stapelfeldt, and T. Seideman, *Three dimensional alignment of molecules using elliptically polarized laser fields*, *Phys. Rev. Lett.* **85**, 2470 (2000).
- [185] H. Tanji, S. Minemoto, and H. Sakai, *Three-dimensional molecular orientation with combined electrostatic and elliptically polarized laser fields*, *Phys. Rev. A* **72**, 063401 (2005).

- [186] K. F. Lee, D. M. Villeneuve, P. B. Corkum, A. Stolow, and J. G. Underwood, *Field-free three-dimensional alignment of polyatomic molecules*, Phys. Rev. Lett. **97**, 173001 (2006).
- [187] S. S. Viftrup, V. Kumarappan, S. Trippel, H. Stapelfeldt, E. Hamilton, and T. Seideman, *Holding and spinning molecules in space*, Phys. Rev. Lett. **99**, 143602 (2007).
- [188] A. Rouzee, S. Guerin, O. Faucher, and B. Lavorel, *Field-free molecular alignment of asymmetric top molecules using elliptically polarized laser pulses*, Phys. Rev. A **77**, 043412 (2008).
- [189] I. Nevo, L. Holmegaard, J. H. Nielsen, J. L. Hansen, H. Stapelfeldt, F. Filsinger, G. Meijer, and J. Küpper, *Laser-induced 3D alignment and orientation of quantum state-selected molecules*, Phys. Chem. Chem. Phys. **11**, 9912 (2009).
- [190] C. Z. Bisgaard, O. J. Clarkin, G. Wu., A. M. D. Lee, O. Geßner, C. C. Hayden, and A. Stolow, *Time-resolved molecular frame dynamics of fixed-in-space CS₂ molecules*, Science **323**, 1464 (2009).
- [191] C. B. Madsen, L. B. Madsen, S. S. Viftrup, M. P. Johansson, T. B. Poulsen, L. Holmegaard, V. Kumarappan, K. Jørgensen, and H. Stapelfeldt, *Manipulating the torsion of molecules by strong laser pulses*, Phys. Rev. Lett. **102**, 073007 (2009).
- [192] R. Krems, W. C. Stwalley, and B. Friedrich, *Cold Molecules: Theory, Experiment, Applications* (CRC Press, Taylor&Francis Group, 2009).

Samenvatting

Dit proefschrift beschrijft hoe grote neutrale molekulen in de gas fase kunnen worden gemanipuleerd en gecontroleerd met elektrische velden. Voordat ik de inhoud van dit werk beschrijf, wil ik eerst kort op twee vragen ingaan. Wat betekent "manipuleren en controleren van molekulen" in deze context, en waarom is dit belangrijk? "Manipuleren" en "controleren" betekent het preciese beïnvloeden van de baan van molekulen om ze te scheiden op basis van hun intrinsieke eigenschappen, zoals hun structuur of hun kwantumtoestand. In een typisch molekuulbundel experiment komen grote molekulen in verschillende vormen voor, de zogenaamde konformeren. Verder is voor een gegeven konformeer de bezetting verdeeld over vele verschillende (rotationele) kwantumtoestanden. Omdat het resultaat van een experiment in de regel afhangt van zowel de vorm als de kwantumtoestand van het molekuul, zijn methoden om molekulen van elkaar te scheiden voor vele toepassingen wenselijk.

Onze methode gebruikt sterke elektrische velden (typisch $E \sim 100$ kV/cm) om molekulen te scheiden. Alhoewel de onderzochte molekulen als geheel elektrisch neutraal zijn, hebben ze een asymmetrische ladingsverdeling. Zulke molekulen worden polair genoemd, en de asymmetrie van hun ladingsverdeling wordt gekarakteriseerd door het dipoolmoment μ . De interactie van een polair molekuul met een elektrisch veld wordt beschreven door het Stark effect (zie hoofdstuk 2), die leidt tot een verschuiving van de molekulaire energie niveaus in een elektrisch veld. De kracht die het molekuul ondervindt hangt af van deze zogenaamde Stark verschuiving en de gradiënt van het veld. Omdat het Stark effect afhankelijk is van de vorm en de kwantumtoestand van het molekuul, kan deze kracht gebruikt worden om molekulen te scheiden. Door de juiste velden aan te leggen kunnen molekulen met ongewenste eigenschappen verwijderd worden, terwijl molekulen met gewenste eigenschappen van de bron tot het detectiegebied doorgelaten worden. Zulke gefilterde molekuulbundels zijn ideaal voor een scala aan toekomstige experimenten, waarvan sommige worden besproken in de rest van deze samenvatting.

Voor de experimenten die in dit proefschrift zijn beschreven zijn twee experimenten opgebouwd om een kwantumtoestand en konformeer van grote neutrale molekulen te selekteren. In de eerste opbouw is een statisch inhomogeen elektrisch veld gebruikt om bundels benzonitriël of joodbenzeen af te buigen (zie hoofdstuk 5). Door molekulen door een 15 cm lange deflector te laten vliegen werden de molekulen gespreid op basis van hun rotationele kwantumtoestand. Molekulen in de laagste rotationele niveaus hebben het grootste Stark effect en worden het meest afgebogen. Molekulen in hoog gelegen niveaus voelen een zwakkere kracht omdat de Stark verschuiving in de regel afneemt met toenemend rotationeel kwantumgetal. De relatieve bezetting van de individuele kwantumtoestanden hangt af van de rotationele temperatuur. De ruimtelijke verdeling van de afgebogen molekuulbundel is daarom erg gevoelig voor veranderingen in deze temperatuur. Door de experimentele en gesimuleerde bundelverdelingen met elkaar te vergelijken kon de rotationele temperatuur van de bundels benzonitriël en joodbenzeen bepaald worden. Omdat de afgebogen molekulen in verschillende kwantumtoestanden op verschillende posities in het detectiegebied aankomen, kan een selectie van de kwantumtoestand in het experiment bereikt worden door het fokus van de detectielaser door de moleculaire verdeling te bewegen.

Als eerste toepassing werd gedemonstreerd dat door kwantumtoestand geselecteerde molekulen te gebruiken, de kwaliteit van laser-geïnduceerde alignment en orientatie van joodbenzeen molekulen aanzienlijk verbeterd kan worden. In deze experimenten worden sterke lineair gepolariseerde laserpulsen gebruikt om de ruimtelijke orientatie van molekulen in het laboratorium te controleren. Deze methode kan belangrijk zijn, bij voorbeeld, voor toekomstige experimenten die als doel hebben de ruimtelijke structuur van molekulen te onderzoeken met röntgenstraling of elektron diffractie. In typische molekuulbundel experimenten bestaat de bundel voor meer dan 90 % uit een atomaire edelgas, en maar voor een kleine fractie uit de te onderzoeken molekulen. De deflektiemethode kan ook belangrijke toepassingen hebben in experimenten waar dit (niet polaire) edelgas bijdraagt aan het gemeten signaal, zoals experimenten waarin gebruikt gemaakt wordt van VUV of Röntgen vrije elektronen lasers. Doordat het edelgas niet wordt beïnvloed door het elektrisch veld worden de afgebogen molekulen automatisch gescheiden van de atomen, en ontstaat er een zeer zuivere en goed gedefinieerde molekuulbundel.

In dezelfde experimentele opbouw werd de afbuiging van 3-aminophenol bestudeerd (zie hoofdstuk 6). 3-Aminophenol bezit twee konformeren, cis-3-aminophenol en trans-3-aminophenol, met respectievelijk een dipoolmoment van 2.3 D en 0.8 D. De twee konformeren kunnen ruimtelijk gescheiden worden met de deflector doordat het meer polaire cis konformeer aanzienlijk meer afgebogen wordt dan het trans konformeer. Deze afgebogen en konformeer-geselecteerde molekulen kunnen in toekomstige experimenten ge-

bruikt worden om, bij voorbeeld, de dynamica in grote molekulen te bestuderen; m.a.w. het direct aanschouwen hoe konformereren in elkaar overgaan. Omdat de konformeer-geselecteerde molekulen ook kwantumtoestand geselecteerd zijn, zou de ruimtelijke orientatie zoals al gedemonstreerd is voor joodbenzeen eenvoudig moeten zijn. Dit kan mogelijkheden bieden voor stereo-specifieke experimenten aan geïsoleerde konformereren, m.a.w. het onderzoeken hoe de ruimtelijke orientatie het reactievermogen van molekulen beïnvloedt.

In hoofdstuk 7 wordt de implementatie van de tweede experimentele opbouw beschreven. In deze opbouw worden geschakelde elektrische velden gebruikt om bundels neutrale molekulen te focuseren. Het focuseren van grote molekulen met elektrische velden is moeilijk omdat zij altijd in zogenaamde hoogveldzoekende toestanden zijn, m.a.w., ze voelen een kracht die richting hoge elektrische velden wijst. Omdat het elektisch veld altijd het hoogst is aan het elektrode oppervlak, hebben de molekulen de neiging tegen de elektroden te botsen. Statische elektrische velden kunnen dus niet gebruikt worden om grote molekulen te focuseren. Het is echter mogelijk om hoogveldzoekers te focuseren met geschakelde velden; een concept dat alternating gradient (AG) focussatie genoemd wordt (zie hoofdstuk 3). AG focussatie wordt sinds tientallen jaren gebruikt om geladen deeltjes in lineaire versnellers, in quadropool massa filters, of in ionen vallen te focuseren. Alhoewel de krachten die op een neutraal molekuul in een elektrisch veld werken vele grootte-orde kleiner zijn dan de krachten die op een ion werken, kan deze techniek toch worden toegepast op neutrale molekulen. Voor de experimenten die in hoofdstuk 7 gepresenteerd zijn is een één meter lange AG focuser geconstrueerd die uit vier cilindrisch symmetrische hoogspanningselektroden bestaat. Het elektrisch veld in de focuser werd snel geschakeld tussen twee zadelpunt configuraties. De optimale schakelfrequentie die de hoogste transmissie door de focuser levert hangt af van de m/μ -verhouding, waarbij m de massa van het deeltje is. Voor een gegeven schakelfrequentie wordt een bepaalde m/μ -verhouding geselecteerd. In de experimenten met 3-aminophenol kon worden gedemonstreerd dat deze frequentie afhankelijke transmissie door de focuser inderdaad gebruikt kan worden om deeltjes met een bepaalde verhouding tussen dipool moment en massa te selecteren. Bij lage schakelfrequenties worden voornamelijk het minder polaire trans konformeer gefocuseerd en doorgelaten, terwijl bij hoge schakelfrequenties de transmissie van het meer polaire cis konformeer toenam. Tenslotte werd in experimenten met aminobenzonitriël gedemonstreerd dat de selectie resolutie verbeterd kan worden door de golfvorm die voor focussatie gebruikt wordt te veranderen. De resultaten die met de focuser werden verkregen zijn complementair aan de deflektie experimenten om konformereren te scheiden. Deflektie heeft als voordeel dat het eenvoudiger te implementeren is, terwijl met de focuser - op zijn minst in principe - potentieel hogere dichtheden mogelijk zijn doordat de molekulen actief bij elkaar worden gehouden.

Summary

This thesis describes how large neutral molecules in the gas phase can be manipulated and controlled using electric fields. Before I summarize the contents of this work, I would like to briefly address two questions. What does “manipulating and controlling molecules” mean in this context, and why is it interesting? Here, “manipulation” and “control” mean influencing the motion of the molecules in a precise way in order to sort them according to their intrinsic properties, such as their structure or their quantum state. In a typical molecular beam experiment, large molecules occur as different conformers or, in other words, they can adopt different shapes. Moreover, for any given conformer the population is distributed over many different (rotational) quantum states. Since the outcome of an experiment generally depends on both the shape and the quantum state, sorting tools for molecules are highly desired and will be beneficial for many applications.

Our approach uses strong electric fields (typically $E \sim 100$ kV/cm) for sorting. Although the molecules investigated here are neutral as a whole, they possess an asymmetric internal charge distribution. Such molecules are called polar molecules and the asymmetry of their charge distribution is characterized by the dipole moment μ . The interaction between a polar molecule and an electric field is described by the Stark effect (see Chapter 2), which leads to a shift of the molecular energy levels in an electric field. This so-called Stark shift and the electric field gradient determine the strength of the force that the molecule experiences in a given field. As the Stark shift is shape and quantum-state dependent, the force induced by electric fields can be exploited to sort the molecules. By applying the appropriate fields, molecules with undesired properties are removed from the sample, while molecules with desired properties are transmitted from the source to the detection region. Such filtered samples are ideal targets for a variety of experiments – some of which will be discussed in the course of this summary.

In the framework of this thesis, two experiments were set up for the quantum-state and conformer selection of large neutral molecules. In the

first setup, a static inhomogeneous electric field is used to deflect beams of benzonitrile or iodobenzene molecules (see Chapter 5). Upon passing through a 15 cm long deflector, the molecules are dispersed according to their rotational quantum state. Molecules in the lowest rotational states have the largest Stark shift and are deflected the most. On the other hand, molecules in high-lying states feel a weaker force since the Stark shift generally decreases with increasing rotational quantum number. The relative populations of the individual quantum states depend on the rotational temperature, therefore the spatial profile of the deflected molecular beam is very sensitive to changes in this temperature. By comparing the experimental data with simulated beam profiles, the rotational temperatures of both beams of benzonitrile and iodobenzene have been determined. Since deflected molecules in different states arrive at different spatial positions in the detection region, quantum-state selection in the experiment can be achieved by focusing the detection laser at different positions within the molecular beam profile.

As a first application, it was shown that the degree of laser-induced alignment and orientation of iodobenzene molecules is considerably improved when quantum-state-selected molecules are used as targets. In these experiments, strong linearly polarized laser pulses are used to control the spatial orientation of the molecules in the laboratory frame. This method might be important, for instance, for future X-ray or electron diffraction experiments on gas-phase molecules aimed at direct imaging of the molecular structure. In a typical molecular beam experiment the sample consists of more than 90% of an inert atomic carrier gas; only a small fraction of the beam contains the molecules under investigation. The deflection method might, therefore, also be important for applications where this (unpolar) carrier gas contributes to the measured signal, such as experiments using novel VUV or X-ray free-electron lasers. The deflected polar molecules are intrinsically separated from the carrier gas, which is not affected by the electric field, and thus represent an extremely clean and well-defined sample.

In the same experimental setup the deflection of 3-aminophenol was studied (see Chapter 6). 3-aminophenol has two conformers, *cis*-3-aminophenol and *trans*-3-aminophenol, with dipole moments of 2.3 D and 0.8 D, respectively. Since the more polar *cis* conformer is deflected considerably more than the *trans* conformer, spatial separation of the two conformers was achieved using the deflector. These deflected and conformer-selected samples could be used in future experiments to study, for instance, dynamics in large molecules, i. e., investigating how the conformers interconvert in real time. Because the conformer-selected molecules are also rotational-quantum-state selected, controlling the spatial orientation in the same way as demonstrated for iodobenzene should be straightforward. This might open the way for stereospecific experiments on isolated conformers, i. e., studying how the spatial orientation

of molecules influences the reactivity.

Chapter 7 goes on to describe the implementation of a second experimental setup. Here, switched electric fields are used to focus beams of polar molecules. Focusing large molecules with electric fields is difficult because they are always in so-called high-field-seeking quantum states, i. e., they feel a force towards regions of strong electric fields. Because the electric field is always highest near the surface of the electrodes, the molecules have a tendency to crash into the electrodes. As a consequence, static electric fields cannot be applied to focus large molecules. It is, however, possible to focus high-field seekers using switched electric fields, a concept that is called alternating gradient (AG) focusing (see Chapter 3). AG focusing has been applied for many decades for the focusing of charged particles in linear accelerators, quadrupole mass filters or ion traps. Even though the forces experienced by a polar molecule in an electric field are many orders of magnitude smaller compared to the respective forces exerted on an ion, this technique can be applied for neutral molecules. For the experiments presented in Chapter 7, a one meter long AG focuser consisting of four cylindrical high-voltage electrodes was constructed. The electric field of the focuser was rapidly switched between two saddle-point configurations. The optimal switching frequency yielding the highest transmission through the focuser depends on the m/μ -ratio, where m is the mass of the particle. For a fixed switching frequency, a m/μ -selection is performed. In experiments on 3-aminophenol it was demonstrated that this frequency-dependent transmission through the focuser can indeed be exploited to select species with distinct dipole moment to mass ratios. At low switching frequencies, predominantly the less polar trans conformer was focused and transmitted, conversely at high switching frequencies the transmission of the more polar cis conformer was enhanced. Finally, in experiments on aminobenzonitrile it was demonstrated that the resolution of the selector can be improved by modifying the waveform used for focusing. The results obtained with the focuser are complementary to the conformer selection experiments with the electrostatic deflector. While the deflector has the advantage of being easier to implement, the selector has – at least in principle – the potential to yield higher densities by actively confining the molecules.

Acknowledgements

*“If I have seen a little further it is by standing on the shoulders of Giants”
(Isaac Newton in a letter to Robert Hooke, 1676)*

Four years ago I came to Berlin after having completed my diploma thesis in a different field of physics. Back then I didn't know much about cold molecules, high-voltage electrodes, or lasers. Fortunately, I could stand on the shoulders of giants and learn from many people. During the last four years I've had the pleasure to work in an extraordinary team, without whom this thesis would not have been possible. At this point I would like to thank all the people who supported me during my PhD project.

Zuerst möchte ich mich bei Gerard Meijer dafür bedanken, dass ich in seiner Gruppe meine Doktorarbeit schreiben konnte. Gerard, vielen Dank für Deine Unterstützung, Deinen ansteckenden Enthusiasmus für die Wissenschaft und die Art wie Du die Gruppe führst. Es macht Spaß hier zu arbeiten, die Erfolge und Geburtstage in Form von Kaffee und Kuchen mit der Gruppe zu teilen, und im jährlichen Fußballturnier anzutreten. Vielen Dank für eine wundervolle Zeit am Fritz. Als nächstes möchte ich mich bei Jochen Küpper für die Betreuung meiner Arbeit bedanken. Jochen, vielen Dank dass Du im Labor mit Rat und Tat zur Seite standst, mir viel über Moleküle beigebracht hast und Dir immer für mich Zeit genommen hast. Danke auch für viele hilfreiche Diskussionen, Deine Ideen und für das sorgfältige Korrekturlesen meiner Arbeit. Mein Dank geht auch an die ehemaligen und aktuellen Mitstreiter in unserer Arbeitsgruppe: Kirstin Wohlfart, Fabian Grätz und Stephan Putzke.

Pertaining to this thesis I'd like to thank Bas van de Meerakker for translating the summary and to Adela Marian and Cynthia Heiner for proof-reading parts of this thesis. I would also like to thank the members of the manuscript committee, Leo Meerts, Henrik Stapelfeldt, and Mike Tarbutt, for carefully reading the manuscript and their helpful comments and suggestions.

Die Experimente, die ich im Rahmen dieser Arbeit aufgebaut habe, wären ohne die technische Unterstützung vieler Kollegen nicht möglich gewesen. An

dieser Stelle möchte ich mich ganz besonders bei Henrik Haak für die Hilfe bei Design und Justage unserer Apparaturen bedanken. Vielen Dank auch Herrn Schwäricke und dem Team der Feinwerktechnik, Georg Heyne und dem Elektroniklabor, sowie Sandy Gewinner für die Unterstützung bei Laserproblemen aller Art. Uwe Hoppe danke ich für die Programmierung von Kouda, Heinz Junkes für die Hilfe bei der Implementierung der Frequenzstabilisierung für unseren Laser, sowie Manfred Erdmann, Georg Hammer, Petrik Bischoff, Wolfgang Erlebach und Rolf Meilicke für technischen Support. Einen Teil meiner Apparatur konnte ich von Undine Erlebam, Marcin Frankowski, und Gert von Helden übernehmen. Vielen Dank dafür. Die Mikrowellenmessungen wurden am Institut für Physikalische Chemie und Elektrochemie der Universität Hannover durchgeführt. In diesem Zusammenhang möchte ich mich bei Jens-Uwe Grabow, Melanie Schnell, Kirstin Wohlfart und Jochen Küpper bedanken.

During the last two years I have had the pleasure to work in an excellent and very fruitful collaboration with Henrik Stapelfeldt and his group in Aarhus. Henrik, Lotte, Jens, Iftach, Jonas, Jochen, and Jan, thanks a lot for your hospitality, fun times in the lab and our good collaboration. Jonas, thank you once more for phase matching – you're way better than my autotracker here in Berlin.

For distraction from work through squash and beer I want to thank Steven, Jochen, Cyndi (I know I still owe you a case of beer), and all the occasional members of the squash group. Adela, I'd like to stress that you do have a sense of humour. Stolli, thanks for introducing the nice Oktoberfest tradition and, Peter, thanks for continuing to organize it. Andreas, I'll never forget the Ski conference in Diavolezza. Thanks for organizing it. I'd also like to thank my former office mates Joost, Stolli, and Philipp as well as my current office mates for fun times in the office. Finally, a big thank you to all diploma students, PhD students, post-docs and colleagues, for a great working atmosphere, the beers on the terrasse, the Wandertage, Sommerfeste, and X-mas parties. Schließlich noch ein riesiges Dankeschön an die gute Seele der Abteilung, Inga von Dölln, die unsere Abteilung hinter den Kulissen am Laufen hält.

And last but certainly not least: Danke meinen Freunden in Berlin (ich weiß jetzt was ein Schiebchen ist) und anderswo, meiner Familie und Dagmar. Ihr macht das Leben lebenswert.

Berlin, im November 2009

Frank Filsinger

Curriculum Vitae

Frank Filsinger

Born on October 9, 1978 in Heidelberg, Germany

- 1998 Abitur at the Gymnasium Wiesloch, Germany
- 1998 - 2004 Physics studies at the Ruprecht-Karls-Universität Heidelberg,
Germany
- 2002 ERASMUS scholar at Uppsala University, Sweden
- 2003 - 2004 Research for the diploma thesis under the supervision of
Prof. Dr. U. Platt at the Institute for Environmental Physics
at the Ruprecht-Karls-Universität Heidelberg.
Subject of the diploma thesis: "MAX-DOAS Measurements of
Tropospheric BrO at the Hudson Bay"
- 2004 Field measurements aboard the research vessel
"Ronald H. Brown" and in New England, USA, in the
framework of the NASA/NOAA ICARTT 2004 campaign.
- 2005 - 2009 PhD student in the group of Prof. dr. G.J.M. Meijer
at the Fritz-Haber-Institut der Max-Planck-Gesellschaft
in Berlin, Germany.
- 2009 - present Post-doc in the group of Prof. dr. G.J.M. Meijer
at the Fritz-Haber-Institut der Max-Planck-Gesellschaft
in Berlin, Germany.

List of Publications

1. MAX-DOAS detection of glyoxal during ICARTT 2004
R. Sinreich, R. Volkamer, F. Filsinger, U. Frieß, C. Kern, U. Platt, O. Sebastián, and T. Wagner
Atmos. Chem. Phys. **7**, 1293 (2007)
2. Precise dipole moments and quadrupole coupling constants of the cis and trans conformers of 3-aminophenol: determination of the absolute conformation
F. Filsinger, K. Wohlfart, M. Schnell, J.-U. Grabow, and J. Küpper
Phys. Chem. Chem. Phys. **10**, 666 (2008)
3. Alternating-gradient focusing and deceleration of large molecules
K. Wohlfart, F. Grätz, F. Filsinger, H. Haak, G. Meijer, and J. Küpper
Phys. Rev. A **77**, 031404(R) (2008)
4. Selector for structural isomers of neutral molecules
F. Filsinger, U. Erlekam, G. von Helden, J. Küpper, and G. Meijer
Phys. Rev. Lett. **100**, 133003 (2008)
5. Stark deceleration of OH radicals in low-field-seeking and high-field-seeking quantum states
K. Wohlfart, F. Filsinger, F. Grätz, J. Küpper, and G. Meijer
Phys. Rev. A **78**, 033421 (2008)
6. Laser-induced alignment and orientation of quantum-state-selected large molecules
L. Holmegaard, J. H. Nielsen, I. Nevo, H. Stapelfeldt, F. Filsinger, J. Küpper, and G. Meijer
Phys. Rev. Lett. **102**, 023001 (2009)
7. Manipulating the motion of large molecules
J. Küpper, F. Filsinger and G. Meijer
Faraday Discuss. **142**, 155 (2009)

8. Pure samples of individual conformers: The separation of stereo-isomers of complex molecules using electric fields
F. Filsinger, J. Küpper, G. Meijer, J. L. Hansen, J. Maurer, J. H. Nielsen, L. Holmegaard, and H. Stapelfeldt
Angew. Chem. Int. Ed. **48**, 6900 (2009)
9. Laser-induced 3D alignment and orientation of quantum-state-selected molecules
I. Nevo, L. Holmegaard, J. H. Nielsen, J. L. Hansen, H. Stapelfeldt, F. Filsinger, G. Meijer, and J. Küpper
Phys. Chem. Chem. Phys. **11**, 9912 (2009)
10. Quantum-state selection, alignment, and orientation of large molecules using static electric and laser fields
F. Filsinger, J. Küpper, G. Meijer, L. Holmegaard, J. H. Nielsen, I. Nevo, J. L. Hansen, and H. Stapelfeldt
J. Chem. Phys. **131**, 064309 (2009)